A Matrix Converter Drive System for an Aircraft Rudder Electro-Mechanical Actuator

Dott.Ing. Liliana de Lillo

Submitted to the University of Nottingham for the degree of Doctor of Philosophy, March 2006.

Abstract

The matrix converter is an attractive topology of power converter for the Aerospace Industry where factors such as the absence of electrolytic capacitors, the potentiality of increasing power density, reducing size and weight and good input power quality are fundamental. The matrix converter potential advantages offers the possibility to achieve the aim of the More Electric Aircraft research which intends to gradually replace, from the aircraft architecture, the hydraulic power source and its infrastructure with electric power generation and a more flexible power distribution system.

The purpose of this work is to investigate the design and implementation of a 40kVA matrix converter for an Electro Mechanical Actuator (EMA) drive system. A SABER simulation analysis of the candidate matrix converter drive systems, for this application, is provided. The design and implementation of the matrix converter is described, with particular attention to the strict requirements of the given aerospace application. Finally, the matrix converter PMSM drive system and the EMA drive system are respectively assembled, tested and commissioned.

Acknowledgements

I would like to express my most sincere gratitude to my supervisors Dr. P.W. Wheeler and Prof. J.C. Clare for their guidance and support over the course of this project and for believing in me.

I would like to thank the staff of the PEMC group at the University of Nottingham and all of the technicians of the ground floor workshop, for providing the necessary help, both theoretical and practical, to carry out this research.

Thanks to all my of friends and colleagues of the PEMC group, especially Lee Empringham, Cesar Silva, Joe Vassallo, Si Dang, Maurizio Catucci, James Campbell, Michael Bland, Maurice Apap, Cedric Caruana, David Gerry and Pericle Zanchetta, for their friendship, their precious advise and technical support, without their help I could have never dreamt to reach the end of this project.

Finally I would like to thank my dear husband and my family for their infinite patience, support and love. They helped me to regain enthusiasm, strength and determination during the difficult times. Thanks for being there for me and believing in me, always.

Claims

The research work which is presented in this thesis has generated the following novel achievements:

A comparative study has been performed to ascertain the suitability of different matrix converter drive systems for aircraft applications. A matrix converter drive system was devised for each of the main motor types to which the aerospace industry has shown interest. These include the switched reluctance, brushless DC, induction and permanent magnet synchronous motors. A uni-directional matrix converter structure was introduced in simulation to drive the switched reluctance machine. These systems were simulated and the physical effects on the matrix converter drive such as power pulsations were presented. Each of the drive systems was then compared on the basis of the results of their analysis and their potential merits for an aerospace application in terms of power quality, torque production and power density.

A 40kVA matrix converter has been designed and built to aerospace requirements for an Electro Mechanical Actuator drive system. Issues which have previously prevented successful implementation such as device packaging, converter layout and protection have been addressed and solutions have been presented.

A robust overvoltage clamp circuit has been introduced and shown to protect the matrix converter under fault conditions. This clamp also improves the reliability of the matrix converter circuit by giving it the ability to withstand a circuit failure such as current direction feedback failure. No electrolytic capacitors were employed in the protection circuit or the power circuit. High quality polypropylene film capacitors were used to minimise the converter volume and respond to important issues such the reliability requirements.

The matrix converter was integrated into the application of the aircraft electro mechanical rudder actuator both thermally and mechanically. This is the first time a matrix converter has been integrated with an application and moreover for an aerospace application involving EMA topology.

The EMA drive system was delivered and commissioned at Smiths Aerospace Actuation Systems in Wolverhampton.

Contents

List of Figures

List of Tables

Chapter 1

Introduction

Voltage Source Inverter (VSI) has been the traditional power converter which is used to provide the variable voltage and frequency from the fixed voltage and fixed frequency supply, for variable speed drive applications. In the VSI, as shown in Figure 1.1, the input supply is first rectified then it is applied to the load by the inverter stage. The control of the output of this two stage converter is achieved by modulating the duty cycles of the devices in the inverter stage so as to produce near sinusoidal output currents in the inductive load machine, of the desired amplitude and frequency.

Figure 1.1 shows a large capacitor placed across the DC link to provide a stiff DC voltage source and energy storage. This means that a large capacitance is needed but within a reasonable volume, therefore electrolytic capacitors are normally used for the DC link components. Electrolytic capacitors typically occupy $30-50\%$ of the total volume of the converter for power levels greater than a few kW and in addition to this they are temperature sensitive.

Due to the diode bridge front end, the inverter circuit shown in Figure 1.1 will draw input currents that are rich in 5th and 7th harmonics, which can become a significant problem at increased power levels. This problem can be solved by employing an active

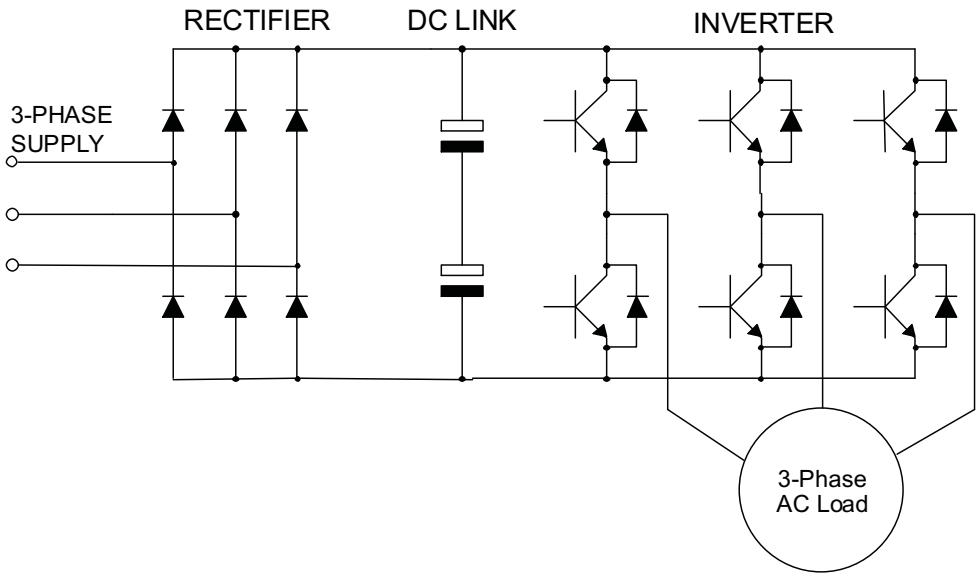

Figure 1.1: Voltage source inverter schematic

PWM rectifier front end as shown in Figure 1.2, which can be modulated to draw near sinusoidal input currents. The active, or sinusoidal front end inverter, which is also known as a back-to-back inverter has the added advantage that the power flow can be bi-directional. However the DC link capacitors are still large and so are the input inductors.

An alternative AC-AC power converter, the matrix converter, is discussed in this thesis. The matrix converter, shown in Figure 1.3, consists of an array of bi-directional switches where any input phase can be connected to any output phase. The duty cycle of the switches can be modulated to produce the desired output amplitude and frequency. The matrix converter is also described as a direct AC-AC converter because it requires no intermediate energy storage.

Much of the work on matrix converter over the past twenty years has been concentrated on modulation algorithms and, more recently, on the practical implementation issues, which have largely been solved. One of the key benefits of the matrix converter technology is the possibility of greater power density due to the absence of a

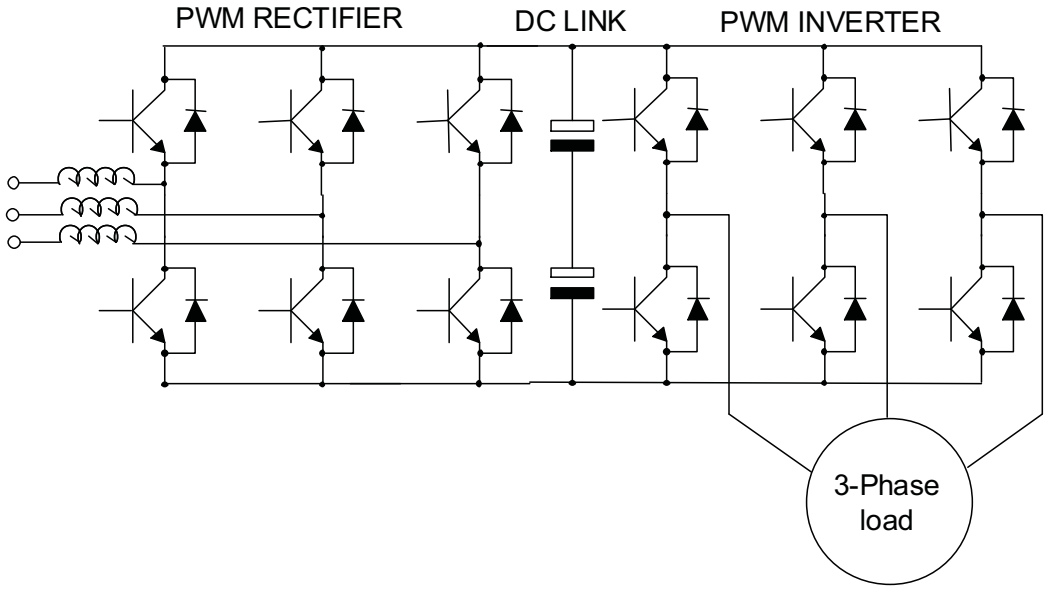

Figure 1.2: Back-to-back inverter schematic

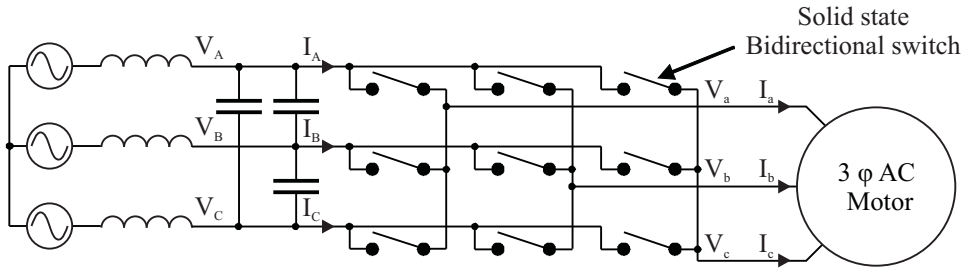

Figure 1.3: Simplified representation of a matrix converter motor drive

DC link. This is translated into a realistic advantage if the filter size is also optimised, by having a sufficiently high switching frequency. This means, though, a compromise between filter size and semiconductor losses must be found.

Factors such as the absence of electrolytic capacitors, the potential for increasing power density, reducing size, reducing weight and obtaining good input power quality are fundamental to aerospace applications. The matrix converter is therefore an attractive topology for the Aerospace Industry who are progressively showing more interest in it. The reason for this interest is the aim of the More Electric Aircraft research which intends to gradually replace, from the aircraft architecture, the hydraulic power source and its infrastructure with electric power generation and a more flexible power distribution system.

The purpose of this work is to investigate the design and implementation of a 40kVA matrix converter for an Electro Mechanical Actuator (EMA) drive system. A SABER simulation analysis of the candidate matrix converter drive systems, for this application, is provided. The design and implementation of the matrix converter is described, with particular attention to the strict requirements of the given aerospace application. Finally, the matrix converter PMSM drive system and the EMA drive system are respectively assembled, tested and commissioned.

1.1 Thesis Structure

The remainder of this thesis is divided into the following Chapters.

In Chapter 2, the More Electric Aircraft research concept is introduced and discussed. Particular attention is given to the flight surface actuator technology and how it is influenced by the MEA idea. Details are given of the Electrically Driven Advanced Actuation Systems (EDAAS) project, which includes this work as one of its components.

In Chapter 3, the matrix converter concept is discussed and the mathematical model from which the modulation problem can be derived is introduced. A brief description of the Venturini and Space Vector Modulation methods is given. The practical implementation issues are introduced and the proposed solutions are discussed. A comparison between the conventional topology of power converters for AC-AC conversion and the matrix converter is provided in terms of a predicted reliability study.

The SABER simulation analysis of the matrix converter drive systems, implementing sinusoidal and non-sinusoidal machines, is described in Chapter 4. The main differences between the drive systems are highlighted and the reason for the choice of the selected matrix converter PMSM drive for the given application, is discussed.

The design and construction of the 40kVA matrix converter is described in Chapter 5. The control of the converter is also described and a more robust approach of circuit protection implementation is proposed.

In Chapter 6, a full description is given of the different assembly and testing stages of the power converter first, the matrix converter PMSM drive system and, finally, the EMA drive system. The correspondent series of results is presented. The Chapter concludes with the description of the testing and commissioning of the EMA drive system at SMITHS AEROSPACE.

In Chapter 7, conclusions are drawn from the work presented and the goals achieved. Also, areas of further research are highlighted.

Chapter 2

The More Electric Aircraft Research

In order to optimise civil aircraft technology by reducing its mechanical complexity and replacing it with electronics, the concepts of the All Electric Aircraft(AEA) and More Electric Aircraft(MEA) have been debated and developed over the past thirty years [1][2]. It was, in fact, in the late 1970s that the idea of an All Electric Aircraft without any hydraulics or pneumatics could introduce many advantages was seriously considered. The idea of AEA was supported by development in building new magnetic materials and progress in power electronic devices. Many studies were carried out by NASA on both the AEA concept, combining it with digital control technology, and the 'All Electric Engine'(AEE), which would have provided electric power for the whole airframe and its accessories.

In the late 1980s the interest of the aerospace industry was directed to a more conservative approach of the MEA concept in which electric power could be used in specific applications such as primary or secondary actuation systems. Although several projects and studies have been conducted and interest has been shown in the MEA concept, no concrete steps forward had been made to replace the consolidated, reliable, conventional aircraft architecture with an unknown and therefore potentially

risky approach. MEA research in Europe has been supported over the past ten years by several initiatives which have seen many companies from the aerospace industry and also other industry sectors involved in collaborative projects. Recently, in the summer of 2005, the first 'More Electric' flight control commercial transport, the Airbus A380, has been successfully completed and almost fully tested. It is the very first realisation of what has been, for a long time, an investigated idea. Further details of the originality introduced in the A380 actuation systems will be discussed in the following section.

2.1 EHA and EMA

In a commercial transport aircraft the flight control surfaces are distinguished as 'primary flight controls' used to control the roll, yaw and pitch of the aircraft and its trajectory and 'secondary flight controls' which control the lift of the wing [3]. Figure 2.1 shows all of the flight control surfaces. Ailerons and spoilers are used to control the roll, single or double panel rudders are employed to control the yaw while the pitch is controlled by elevators and horizontal stabilisers. The secondary flight controls are achieved by using flaps and slats which modify the shape of the wing and produce a different lift effect on the aircraft at a given angle of attack. In a conventional architecture these flight control surfaces are hydraulically powered from a main hydraulic pump supplied with mechanical power generated by the engines [4]. These engines use the fuel to generate mainly propulsive power to move the aircraft, mechanical power using a gearbox which drives the main hydraulic pump, other local pumps for engine equipment and the main electrical generator. The main hydraulic pump therefore provides, through a heavy piping system, hydraulic power for many systems on board including not only the flight control surfaces but also for example the thrust reversal systems, the engine actuation and the landing gear systems. Finally the main generator provides electrical power to the avionics, cabin and aircraft lighting and for other loads.

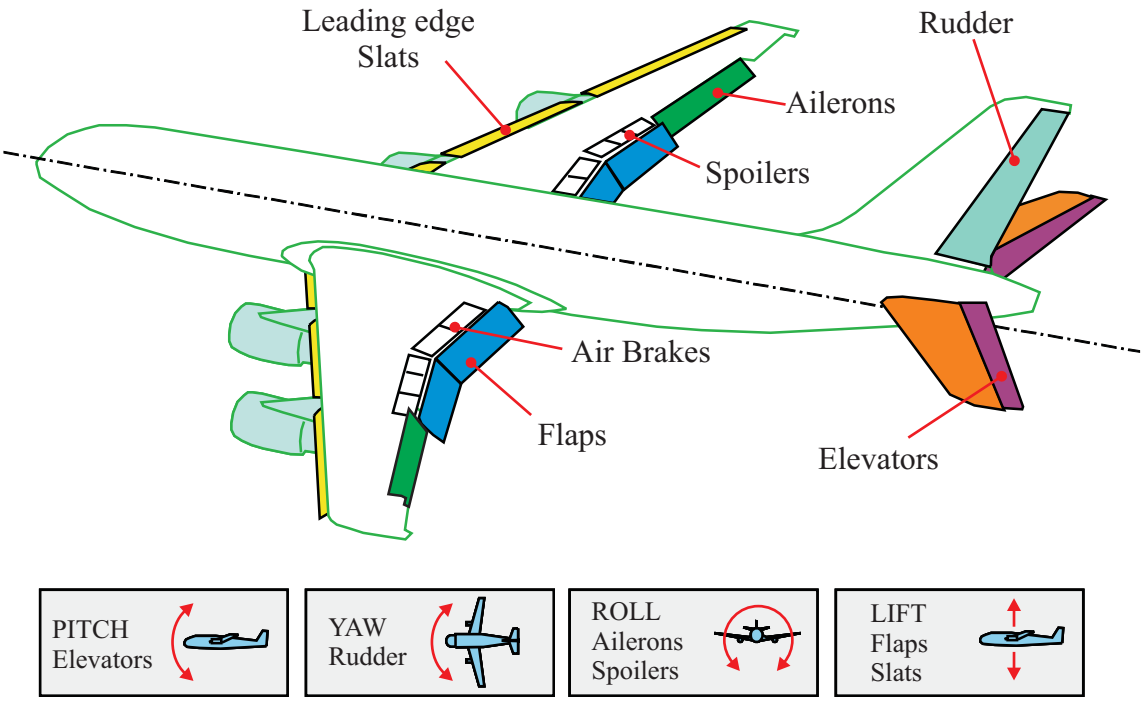

Figure 2.1: Diagram of an aircraft with flight control surfaces

The debating point is the complex system of hydraulic piping which has been fully tested over the years and is capable of high power density responding to the high demand for on-board power. Nevertheless it could be potentially dangerous because of leakage of corrosive hydraulic fluid and it adds considerable weight to the aircraft architecture. On the other hand, the MEA concept pushes towards the direction of replacing the heavy, and not fully secure, hydraulic system with a lighter and more flexible electrical cabling system. Safety and reliability are again the main drivers of the aerospace industry and if problems connected to ageing of the electrical wires and potential fire hazards due to short-circuiting or arcing are not overcome, the goal of creating an all electric aircraft will not occur soon [5].

A very positive example of the MEA concept becoming reality is represented by the introduction of Electro Hydrostatic Actuators (EHA) in parallel with conventional hydraulic ones in the new Airbus A380. Figure 2.2 shows a schematic diagram of an EHA. The conventional flight control system technology is regulated by the 'Fly

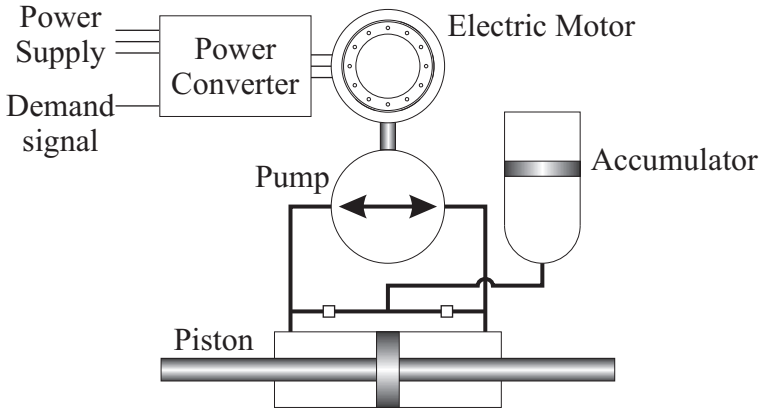

Figure 2.2: Schematic diagram of an electro hydrostatic actuator

By Wire' concept where hydraulic actuators are supplied by centralized hydraulic systems and controlled by electrical signals. The number of actuators per control surface can vary between one and three for redundancy due to safety reasons [3]. During normal flight conditions one or two actuators are active and the remaining ones are in a stand-by configuration.

Differently to a hydraulic actuator which is powered by localised hydraulic pumps, an EHA has an integrated pump driven by a variable speed electric motor. The pump and the electric motor achieve the control of the flight surface by controlling the transfer of hydraulic fluid shared by the individual actuator.

In the new A380, one hydraulic actuator has been replaced with two Electro Hydrostatic ones, plus for some control surfaces such as the two rudder actuators, Electrical Back-up Hydraulic Actuators (EBHA) have been implemented in parallel with the hydraulic ones. The EBHA offers the possibility to choose how to power a given actuator either from a hydraulic system or from an electric system as for an EHA. The two hydraulic and two electric (2H/2E) power source arrangement of the A380 offers advantages in terms of safety because the increase in the number of power systems from three to four introduces a higher degree of redundancy and flexibility. The elimination of one hydraulic supply not only eliminates potential leakage sources but also reduces weight and costs. Figure 2.3 shows a schematic diagram of the layout

of the actuator power system of the 2H/2E used on the A380. The two hydraulic systems, 'green' and 'yellow' are denoted using 'G' and 'Y' and the two electrical systems, 'electrical 1' and 'electrical 2' are denoted using 'E_1' and 'E_2'. Each flight surface uses multiple actuators supplied from different power systems. It can be seen that even if different power systems fail, control of the aircraft will be maintained.

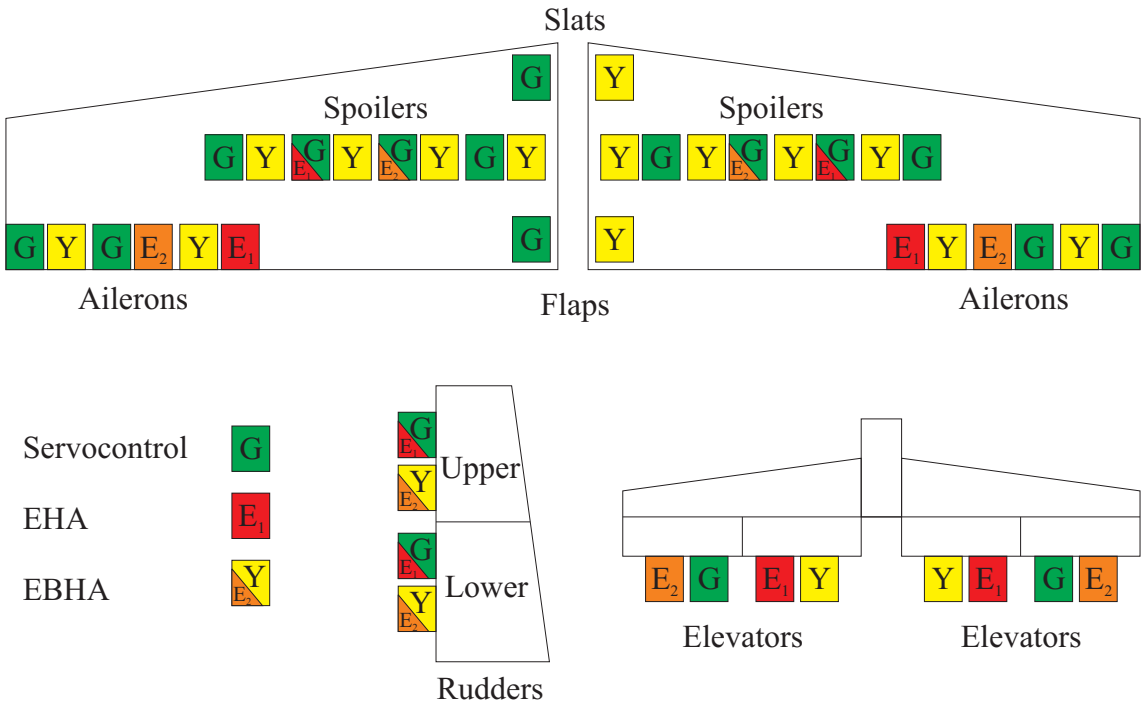

Figure 2.3: Actuator power system layout of the A380

An alternative electrical actuator is the Electro-Mechanical Actuator (EMA) as shown in Figure 2.4. It is characterised by an electric motor which directly drives a gear set which then drives a ball screw which moves the flight surface removing the need for any hydraulic system. This is the major novelty of EMA which introduces a series of benefits such as reduced complexity, weight and maintenance while increasing reliability. Even though EMAs are potentially more attractive then EHAs, they have few a areas which need further investigation and research such as the jamming probability of an EMA or their wear life. An example of an EMA application is shown in the following section.

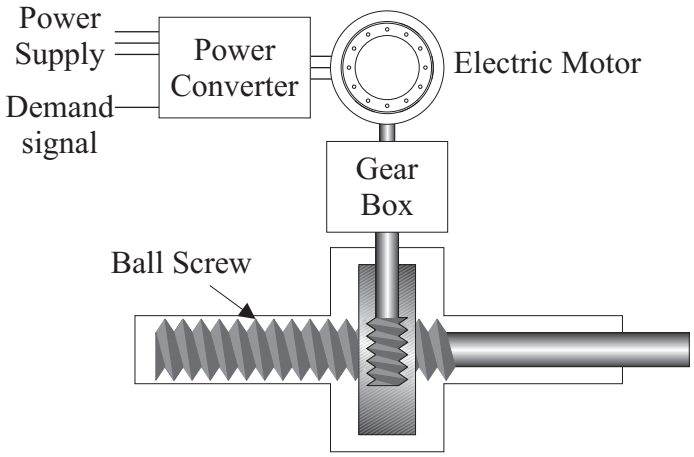

Figure 2.4: Schematic diagram of an electro-mechanical actuator

2.2 The Electrically Driven Advanced Actuation System (EDAAS) Study

An example of the development of MEA is the EDAAS project. The EDAAS project, completed in the Spring of 2005, has been a DTI funded programme as part of the Civil Aircraft Research and Technology Demonstration (CARAD) initiative which was launched in the late 1990s to support and stimulate research into electric systems which can replace hydraulic and pneumatic ones in the next generation of civil aircraft. The EDAAS project aimed to demonstrate an EMA to control a large aircraft rudder surface by employing an innovative topology of power converter, the matrix converter, which is able to be driven from frequency wild power systems, thus avoiding the DC conversion stage. Considering that the aircraft's varying engine speeds generate a variable frequency AC supply with a range of frequencies from 400Hz to 800Hz, if a load requires a fixed frequency supply or DC voltage, bulky rectification units are inevitable [5][6]. An alternative solution to a heavy and complex way of achieving fixed frequency power sources on-board could be a direct AC to AC converter such as the matrix converter. The EDAAS demonstrator was considered to be a 'Not For Flight' experimental unit operated at ground laboratory conditions with the purpose

of model validation and analysis of its performance in order to develop flight standard equipment. Although the demonstrator has not been built to withstand the target application environmental conditions, a review of these requirements has been taken into consideration to investigate their effects on the matrix converter. On the other hand the matrix converter topology itself has appealing features when considered for an aerospace application such as the absence of electrolytic capacitors which are temperature sensitive and therefore unreliable when the typical temperature range for this applications varies between $-55°C$ and $+70°C$. Moreover they can be bulky and heavy. Besides, the matrix converter is characterised by inherent bidirectional power flow and control of input power factor.

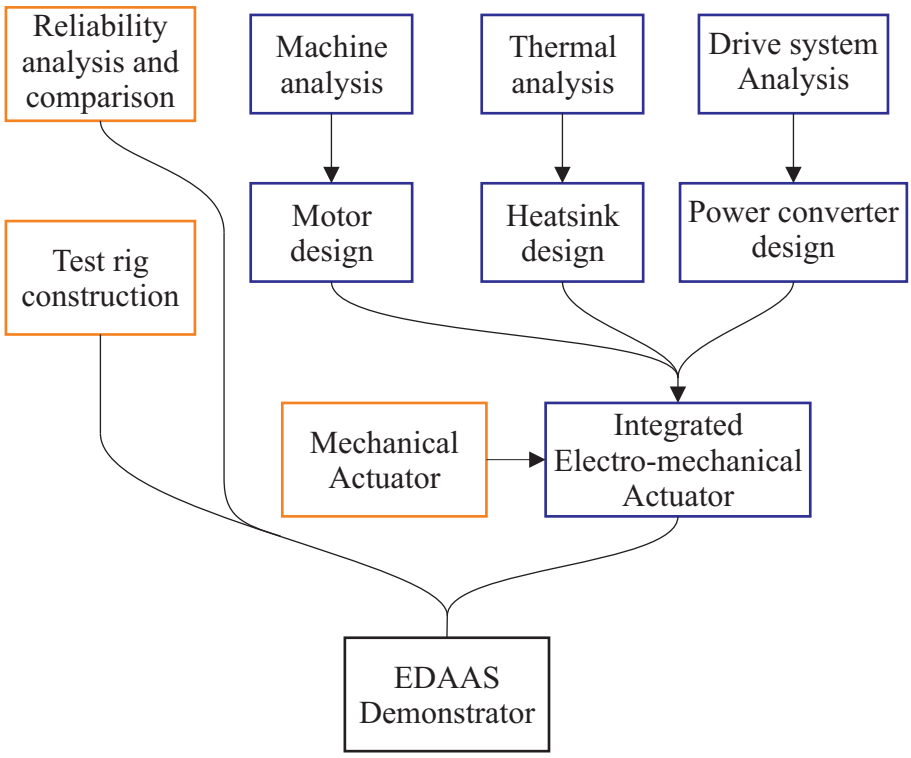

Figure 2.5: Diagram to show the concept of the EDAAS project

The EDAAS project is the result of multiple studies all acting to optimise the final demonstrator to aircraft requirements. It is the joined collaboration of different parts involved in the design and practical realisation of an electrical machine, a matrix

converter and the heat sink for the electronics as a result of the analysis on the thermal aspect of the application. This work has been complemented by a comparative study on the reliability of matrix converters against rectifier-inverter topologies [7](more details will be given in Section 3.7). The areas highlighted in orange in Figure 2.5 were the responsibility of the engineers at Smiths Aerospace in Wolverhampton. Those areas indicated in blue were the responsibility of Nottingham University. The thermal modelling and heat sink design was done by the School of Mechanical Engineering and the remaining work was carried out by the School of Electrical and Electronic Engineering.

The drive system analysis, and the design, construction and testing of the matrix converter implemented in this project, together with the final assembly and testing of the demonstrator, will be described in this thesis.

2.3 Prospects for the future of More Electric Aircraft

To ensure successful technological improvements in the future of the aerospace industry more needs to be done in order to respond to very demanding environments. Thermal management is a fundamental issue for developing new technologies in the spirit of the MEA concept. Both power electronics and electric machinery are affected by this issue. Providing cooling systems for the electronics mounted in restricted environments such as the ones encountered in aerospace applications can be difficult and involve complex mechanisms which can add weight and cost to the entire system. Further developments are required in the field of the Silicon Carbide (SiC) power devices which by replacing the silicon devices, can offer improvements to power conditioning size, weight, efficiency and above all temperature capability as will be discussed in Section 3.3.

Passive components such as capacitors are devices affected by temperature change

and emerging technologies which employ Fluorene Polyester(FPE) and Diamond-Like Carbon (DLC) instead of polycarbonate offer higher temperature and energy density capabilities [8]. On the electric machines side more research is required on magnetic materials and insulation because existing materials cannot meet the high operating temperature requirements which can be in the range of $300°C$ to $500°C$. Overall, it is the contribution from different industry sectors and research programmes which involve not only industry but also the academic world which will lead to a constructive progress in aerospace applications. Without forgetting the complex process of new certification and safety standards which are required for new technologies as a consequence of high demand in safety and reliability [9].

2.4 Summary

This chapter gives an overview of the history and research in More Electric Aircraft applications. One aspect investigated with the MEA approach is the replacement of hydraulic actuators with electrically powered ones and they can be distinguished in EHA and EMA. One example of a real MEA implementation and the use of an EHA, used in the 2H/2E configuration is the new aircraft from Airbus, the A380. An example of how an EMA could be implemented involving new power converter technologies has been introduced with the EDAAS project description which forms the basis of this thesis. The future of MEA applications is in collaborative research in new technologies which can meet the high requirements of the aerospace industry.

Chapter 3

The Matrix Converter Concept

The matrix converter concept was first introduced in the early 1970s with the pioneering work of L.Gyugyi and B.Pelly on 'Static Power frequency Changers' followed by their publication in 1976 [10]. The matrix converter circuit was at that time known as the Forced Commutated Cycloconverter that was a cycloconverter in which the devices were bidirectional static power switches which when provided with the appropriate control allowed the converter to be used as an unrestricted frequency changer capable of power regeneration. Since then years of research have been spent to optimise the control of the devices in the matrix converter in order to operate a safe and efficient implementation of this topology of converters in the real world.

In the following sections the fundamentals of matrix converter operation are discussed and its advantages and disadvantages are highlighted with reference to conventional Voltage Source Inverters (VSI). A review of the solutions to the practical implementation problems proposed over the years is given including a description of the mathematical models which are used to solve the modulation problem.

3.1 The Matrix Converter Circuit

A simplified block diagram of a 3-phase to 3-phase Matrix Converter drive system is shown in Figure 3.1. The matrix converter circuit consists of an array of bi-directional switches constructed from unidirectional power devices, arranged in such a way as to enable any input line to be connected to any output line. The switch duty cycles are modulated to generate the desired output waveform on the basis of the input supply voltages and the demanded output voltages. The demanded voltages are generally the output of a cascaded speed and current control loop. A matrix converter can be viewed as an all silicon solution to the general AC-AC power conversion problem. Compared to the conventional AC/DC/AC converter, matrix converters have many advantages. Above all no DC-link is required for this topology of converter, removing the necessity for bulky electrolytic capacitors which are intolerant to high temperatures and have a relatively short life time. As a result a large capacity and compact converter system can be designed. Bi-directional power flow is straightforward with a matrix converter and by controlling the switching devices appropriately both output voltage and input current are sinusoidal with only harmonics around or above the switching frequency. Depending on the modulation technique it can be arranged that unity displacement factor is seen at the supply side irrespective of the type of load.

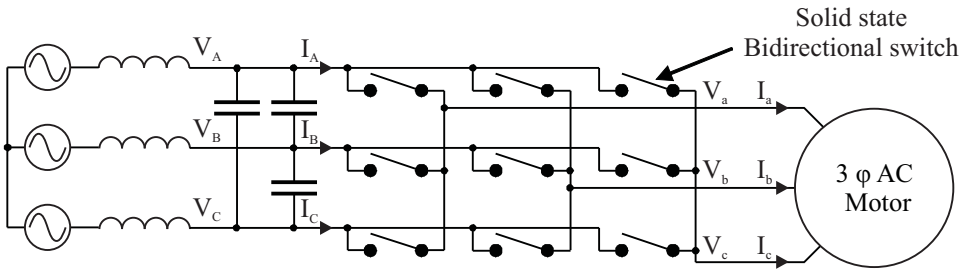

Figure 3.1: Simplified representation of a matrix converter motor drive

As many problems involving the technical implementation of matrix converters are resolved, the interest from industry for this topology of converters increases. With the price of semiconductors falling, matrix converters could become a more attractive

future alternative to the back-to-back inverter in applications where sinusoidal input currents or true bi-directional power flow are required. The voltage transfer ratio limitation as it will be shown in Section 3.2.2, is a real problem if standard machine and standard supply are to be used. If the application allows the specification of the machine voltage, the voltage ratio limitation is not the main issue in the design of the drive. More important innovative and efficient strategies of implementing circuit protection for the matrix converter will ease the way to the commercialisation of this converter in applications such as integrated motor drives, aerospace and marine propulsion applications where power density, space and weight play a fundamental role. This view is reinforced by the possibility that the matrix converter could be the ideal converter topology to employ future technologies such as high temperature silicon carbide devices. Adding to this, the absence of large electrolytic capacitors helps to overcome the problem of electronic equipment operating in difficult environmental conditions.

The Power Electronics, Machine and Control group (PEMC) from Nottingham University has been involved in research on matrix converters for over a decade. Recently it has been specializing in the design and construction of compact and efficient medium/high power matrix converters for the Aerospace Industry. No commercial matrix converters are available on the market to date, although Yaskawa Electric has been publicly promoting their matrix converter drives to be launched in the near future.

3.2 Mathematical Model and Modulation Strategies

In this section the mathematical model of matrix converter operation is established and the modulation problem is introduced. Matrix converter modulation has received a significant amount of attention in the literature and several different modulation methods have been proposed. In this section two of the most common modulation

methods are described. Most of the other methods are similar and are not discussed.

A 3-phase input 3-phase output converter will form the basis of the discussion in this study but the basic idea can be extended to a converter with any number of input and output phases by simply adding more bi-directional switches. The designation of input and output ports at this stage is arbitrary since the converter is symmetrical. However, for any sensible mode of operation, one port should have a voltage stiff characteristic and the other a current stiff characteristic. For the following discussion and throughout this thesis it is assumed that the input port is voltage stiff and the output port is current stiff which is the case for variable speed drive applications. An input line filter is included to circulate the high frequency switching harmonics and provides the voltage stiff characteristic through line to line capacitors. The output inductance is usually part of the load. In this thesis upper case suffixes denote the input phases and lower case suffixes denote the output phases as shown in Figure 3.1.

Assuming ideal switching, a mathematical model for the topology in Figure 3.1 can be derived using the concept of switching functions [11]. The switching function, S_{Kj} for the switch connecting input line K to output line j, is defined to be 1 when the switch is ON and 0 when the switch is OFF. The instantaneous current and voltage relationships can then be written as given in (3.1).

$$\begin{bmatrix} v_a(t) \\ v_b(t) \\ v_c(t) \end{bmatrix} = \begin{bmatrix} S_{Aa}(t) & S_{Ba}(t) & S_{Ca}(t) \\ S_{Ab}(t) & S_{Bb}(t) & S_{Cb}(t) \\ S_{Ac}(t) & S_{Bc}(t) & S_{Cc}(t) \end{bmatrix} \begin{bmatrix} v_A(t) \\ v_B(t) \\ v_C(t) \end{bmatrix}$$

$$\begin{bmatrix} i_A(t) \\ i_B(t) \\ i_C(t) \end{bmatrix} = \begin{bmatrix} S_{Aa}(t) & S_{Ab}(t) & S_{Ac}(t) \\ S_{Ba}(t) & S_{Ba}(t) & S_{Bc}(t) \\ S_{Ca}(t) & S_{Cb}(t) & S_{Cc}(t) \end{bmatrix} \begin{bmatrix} i_a(t) \\ i_b(t) \\ i_c(t) \end{bmatrix} \tag{3.1}$$

Due to the lack of freewheeling diodes in the matrix converter configuration there is a fundamental restriction on the permissible switching combinations in that short circuits of the capacitive input and open circuits of the inductive output must be avoided. This means that at any instant one and only one switch on each output

phase must be closed. This is stated in terms of switching functions in (3.2).

$$\sum_{K=A,B,C} S_{Ka}(t) \;=\; \sum_{K=A,B,C} S_{Kb}(t) \;=\; \sum_{K=A,B,C} S_{Kc}(t) = 1 \tag{3.2}$$

Meeting these constraints is one of the practical implementation issues that has received a significant amount of attention in the past. For the following analysis, it is assumed that (3.2) is obeyed and the commutation between switches is instantaneous.

The output waveforms of the matrix converter are formed by selecting each of the input phases in sequence for defined periods of time. Typical waveforms for a relatively low switching frequency are shown in Figure 3.2. The output voltage consists of segments made up from the three input voltages. The input current consists of segments of the three output currents plus blank periods during which the output current freewheels through the switch matrix. There is normally a fixed repeat period for the switch sequence, T_{seq} which is analogous to the carrier period in conventional PWM. The switching pattern normally follows something similar to that shown in Figure 3.3. To determine the average behaviour of the converter at output frequencies well below the switching frequency a modulation duty cycle can be defined for each switch (eg. $m_{Aa}(t) = \frac{t_{Aa}}{T_{seq}}$ where t_{Aa} refers to the time for which S_{Aa} is ON and T_{seq} is the sequence time of the PWM pattern). These continuous time functions can then be used to define and compare the modulation strategies, as set out in equation (3.3).

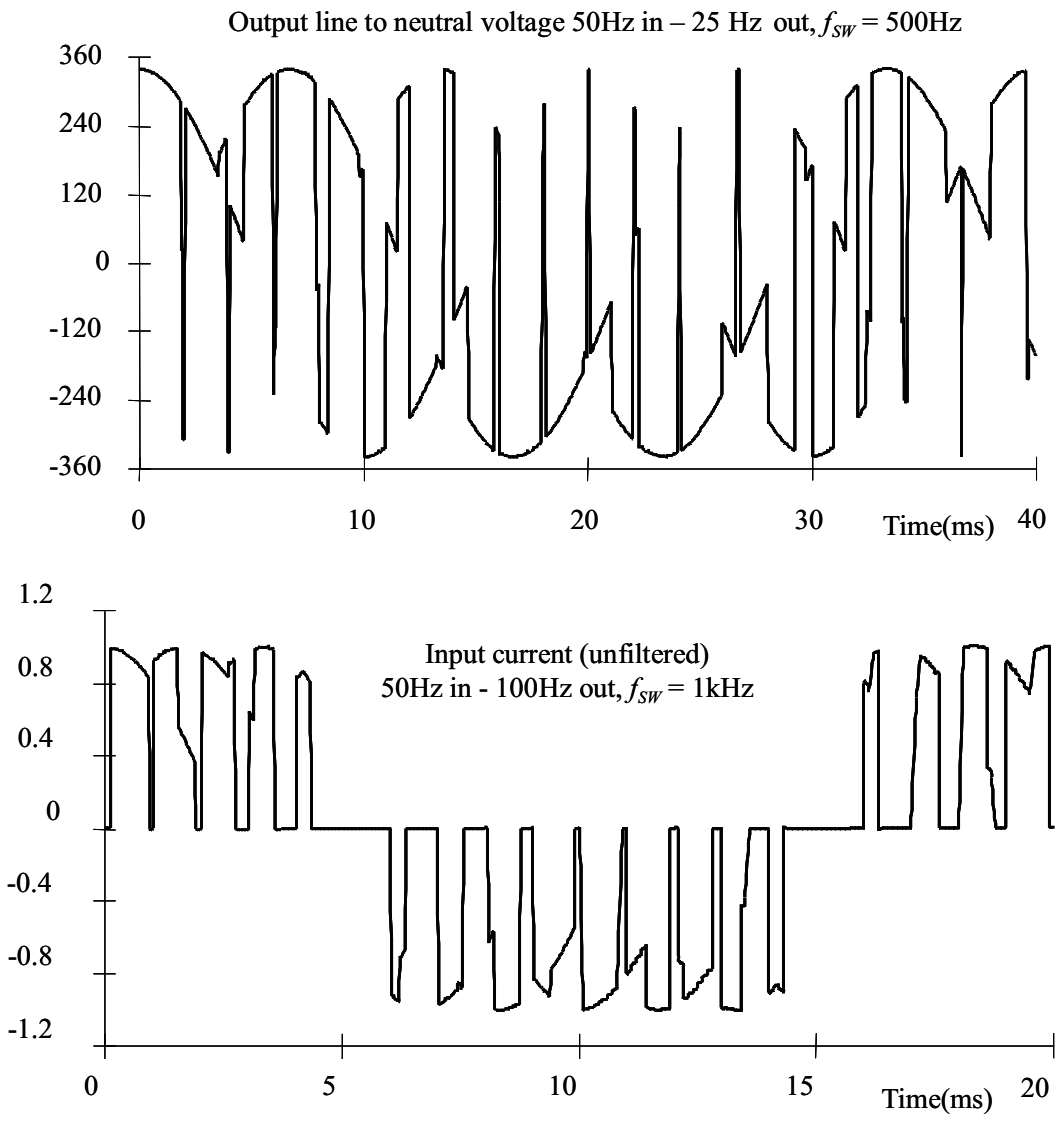

Figure 3.2: Example of typical Matrix Converter waveforms

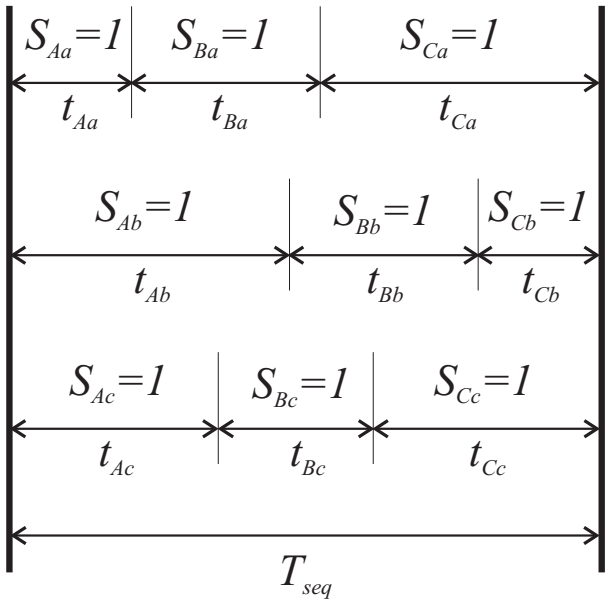

Figure 3.3: General form of switching pattern

$$\begin{bmatrix} v_a(t) \\ v_b(t) \\ v_c(t) \end{bmatrix} = \begin{bmatrix} m_{Aa}(t) & m_{Ba}(t) & m_{Ca}(t) \\ m_{Ab}(t) & m_{Bb}(t) & m_{Cb}(t) \\ m_{Ac}(t) & m_{Bc}(t) & m_{Cc}(t) \end{bmatrix} \begin{bmatrix} v_A(t) \\ v_B(t) \\ v_C(t) \end{bmatrix}$$

$$\begin{bmatrix} i_a(t) \\ i_b(t) \\ i_c(t) \end{bmatrix} = \begin{bmatrix} m_{Aa}(t) & m_{Ab}(t) & m_{Ac}(t) \\ m_{Ba}(t) & m_{Ba}(t) & m_{Bc}(t) \\ m_{Ca}(t) & m_{Cb}(t) & m_{Cc}(t) \end{bmatrix} \begin{bmatrix} i_A(t) \\ i_B(t) \\ i_C(t) \end{bmatrix} \tag{3.3}$$

Note that in (3.3) v_x & i_x $(x = a, b, c)$ are now values averaged over the sequence time.

Equation (3.3) can be presented in a more compact notation where M(t) is known as the modulation matrix:

$$\begin{aligned} [v_o(t)] &= [M(t)][v_i(t)] \\ [i_i(t)] &= [M(t)]^T[i_o(t)] \end{aligned} \tag{3.4}$$

The constraint equation is now given by:

$$\sum_{K=A,B,C} m_{Ka}(t) \;=\; \sum_{K=A,B,C} m_{Kb}(t) \;=\; \sum_{K=A,B,C} m_{Kc}(t) = 1 \tag{3.5}$$

3.2.1 The Modulation Problem and Basic Solution

The modulation problem is usually posed assuming that a set of sinusoidal output voltages, $v_o(t)$ and input currents, $i_i(t)$ are required. Given a set of input voltages, $v_i(t)$ and an assumed set of output currents, $i_o(t)$:

$$[v_i(t)] = V_{im} \begin{bmatrix} \cos(\omega_i t) \\ \cos(\omega_i t + \frac{2\pi}{3}) \\ \cos(\omega_i t + \frac{4\pi}{3}) \end{bmatrix} \qquad [i_o(t)] = I_{om} \begin{bmatrix} \cos(\omega_o t + \phi_o) \\ \cos(\omega_o t + \phi_o + \frac{2\pi}{3}) \\ \cos(\omega_o t + \phi_o + \frac{4\pi}{3}) \end{bmatrix} \tag{3.6}$$

find a modulation matrix M(t) such that:

$$[v_o(t)] = qV_{im} \begin{bmatrix} \cos(\omega_o t) \\ \cos(\omega_o t + \frac{2\pi}{3}) \\ \cos(\omega_o t + \frac{4\pi}{3}) \end{bmatrix} \qquad [i_i(t)] = q\frac{\cos\phi_o}{\cos\phi_i} I_{om} \begin{bmatrix} \cos(\omega_i t + \phi_i) \\ \cos(\omega_i t + \phi_i + \frac{2\pi}{3}) \\ \cos(\omega_i t + \phi_i + \frac{4\pi}{3}) \end{bmatrix} \tag{3.7}$$

and the constraint equation (3.5) is satisfied. In equation (3.7) q is the voltage transfer ratio, ω_i and ω_o are the input and output frequencies and ϕ_i and ϕ_o are the input and output phase displacement angles respectively. There are two basic solutions to this problem which were derived by Venturini [12]:

$$[M1(t)] = \frac{1}{3} \begin{bmatrix} 1+2q\cos(\omega_m t) & 1+2q\cos(\omega_m t - \frac{2\pi}{3}) & 1+2q\cos(\omega_m t - \frac{4\pi}{3}) \\ 1+2q\cos(\omega_m t - \frac{4\pi}{3}) & 1+2q\cos(\omega_m t) & 1+2q\cos(\omega_m t - \frac{2\pi}{3}) \\ 1+2q\cos(\omega_m t - \frac{2\pi}{3}) & 1+2q\cos(\omega_m t - \frac{4\pi}{3}) & 1+2q\cos(\omega_m t) \end{bmatrix} \tag{3.8}$$

with $\omega_m = (\omega_o - \omega_i)$

$$[M2(t)] = \frac{1}{3} \begin{bmatrix} 1+2q\cos(\omega_m t) & 1+2q\cos(\omega_m t - \frac{2\pi}{3}) & 1+2q\cos(\omega_m t - \frac{4\pi}{3}) \\ 1+2q\cos(\omega_m t - \frac{2\pi}{3}) & 1+2q\cos(\omega_m t - \frac{4\pi}{3}) & 1+2q\cos(\omega_m t) \\ 1+2q\cos(\omega_m t - \frac{4\pi}{3}) & 1+2q\cos(\omega_m t) & 1+2q\cos(\omega_m t - \frac{2\pi}{3}) \end{bmatrix} \tag{3.9}$$

with $\omega_m = (\omega_o + \omega_i)$.

The solution in (3.8) yields $\phi_i = \phi_o$ giving the same phase displacement at the input and output of the converter whereas the solution in (3.9) yields $\phi_i = -\phi_o$ giving reversed phase displacement at the input. Combining the two solutions provides the means for input displacement factor control.

$$[M(t)] = \alpha_1[M1(t)] + \alpha_2[M2(t)] \qquad \text{where } \alpha_1 + \alpha_2 = 1 \tag{3.10}$$

Setting $\alpha_1 = \alpha_2$ gives unity input displacement factor regardless of the load displacement factor. Other possibilities exist, through the choice of α_1 and α_2, to have a leading displacement factor (capacitive) at the input with a lagging (inductive) load at the output and vice versa.

For $\alpha_1 = \alpha_2$ the modulation functions can be expressed in the compact formula:

$$m_{Kj} = \frac{t_{Kj}}{T_{seq}} = \frac{1}{3}\left(1 + \frac{2v_K V_j}{V_{im}^2}\right) \quad \text{for } K = A, B, C \text{ and } j = a, b, c \tag{3.11}$$

The modulation algorithm defined by (3.11) operates such that, during each switching sequence, the average output voltages (taken over the switching sequence) equal the target output voltages $[v_o(t)]$. For this to be possible the target output voltages must fit within the input voltage envelope for all operating conditions. Using this solution the maximum value of input to output voltage ratio (q) that the converter can achieve is 50%, as shown in Figure 3.4. The algorithm (3.11) is ideally suited for real time implementation of this basic method but is of little practical use because of the 50% voltage transfer ratio limitation.

3.2.2 Optimum Amplitude Algorithm

The maximum theoretical output voltage can be improved to 87% of the input voltage by modifying the target output voltage matrix to include third harmonics of the input and output frequencies [13]. To achieve this Venturini's optimum method employs the common-mode addition technique defined in [14]. The output voltage target

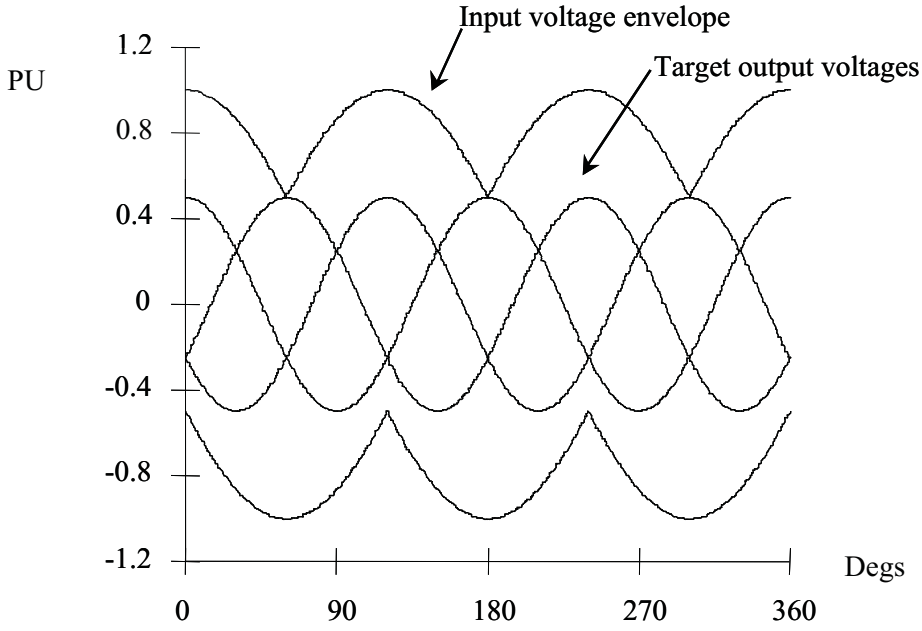

Figure 3.4: Theoretical waveforms illustrating the 50% voltage ratio limit

waveforms now make full use of the input voltage envelope, as shown in Figure 3.5. These third harmonics will cancel in a three-phase load in the same way as they do with third harmonic addition in a conventional inverter. To achieve this the target output voltages in (3.7) are modified to those given in (3.12)

$$[v_o(t)] = qV_{im} \begin{bmatrix} \cos(\omega_o t) - \frac{1}{6}\cos(3\omega_o t) + \frac{1}{2\sqrt{3}}\cos(3\omega_i t) \\ \cos(\omega_o t + \frac{2\pi}{3}) - \frac{1}{6}\cos(3\omega_o t) + \frac{1}{2\sqrt{3}}\cos(3\omega_i t) \\ \cos(\omega_o t + \frac{4\pi}{3}) - \frac{1}{6}\cos(3\omega_o t) + \frac{1}{2\sqrt{3}}\cos(3\omega_i t) \end{bmatrix} \tag{3.12}$$

Note that for a matrix converter, triple harmonics of both the input and output frequencies are added to achieve the optimum output. If unity displacement factor is required, it has been shown [13] that the equation given in (3.11) becomes:

$$\begin{aligned} m_{Kj} &= \frac{1}{3}\left(1 + \frac{2v_K V_j}{V_{im}^2} + \frac{4q}{3\sqrt{3}}\sin(\omega_i t + \beta_K)\sin(3\omega_i t)\right) \quad \text{for } K = A, B, C \text{ and } j = a, b, c \\ \beta_K &= 0, \frac{2\pi}{3}, \frac{4\pi}{3} \quad \text{for } K = A, B, C \text{ respectively} \end{aligned} \tag{3.13}$$

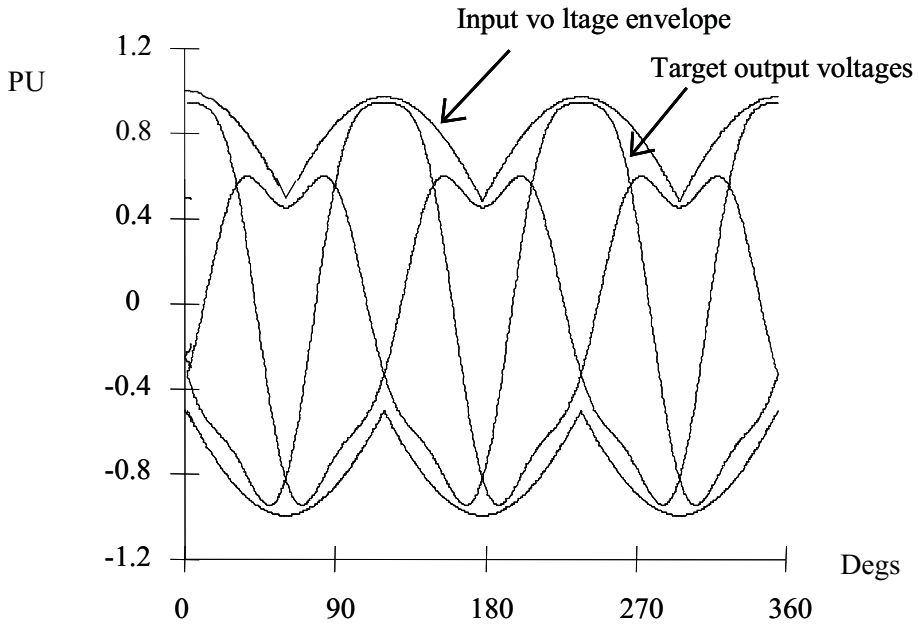

Figure 3.5: Theoretical waveforms illustrating the third harmonic addition to obtain the 87% optimum voltage ratio limit

Note that in (3.13), the target output voltages, V_j, include the triple harmonic addition as defined in (3.12). Equation (3.12) provides the basis for real-time implementation of the optimum amplitude Venturini method which is readily handled by modern microprocessors up to sequence (switching) frequencies of tens of kHz. Input displacement factor control can be introduced into the formulation in (3.12) by inserting a phase shift between the actual input voltages and the input voltages, v_K, inserted into (3.12). However, it should be noted that the output voltage limit reduces from $0.87V_{im}$ for input displacement factors other than unity.

3.2.3 Scalar Modulation Methods

The scalar modulation method presented in [15] and [16] is based on the idea of calculating the switch actuation signals directly from measurements of the instantaneous input voltages and comparing their relative magnitudes following the algorithm below:

1 Assign subscript M to the input which has a different polarity to the other two inputs

2 Assign subscript L to the smallest (absolute) of the other two inputs. The third input is assigned subscript K.

The modulation duty cycles are then given by:

$$\begin{aligned} m_{Lj} &= \frac{(v_j - v_M)v_L}{1.5V_i m^2} \\ m_{Kj} &= \frac{(v_j - v_M)v_K}{1.5V_i m^2} \\ m_{Mj} &= 1 - (m_{Lj} + m_{Kj}) \text{ for } j = a, b, c \text{ respectively} \end{aligned} \tag{3.14}$$

Again, common-mode addition is used with the target output voltages v_j to achieve 87% voltage ratio capability. Despite the apparent differences, this method yields virtually identical switch timings to the optimum Venturini method. Expressed in

the form of 3.13, the modulation duty cycles for the scalar method are given in 3.15.

$$m_{Kj} = \frac{1}{3}\left(1 + \frac{2v_K V_j}{V_{im}^2} + \frac{2}{3}\sin(\omega_i t + \beta_K)\sin(3\omega_i t)\right) \quad \text{for } K = A, B, C \text{ and } j = a, b, c$$
$$\beta_K = 0, \frac{2\pi}{3}, \frac{4\pi}{3} \quad \text{for } K = A, B, C \text{ respectively} \tag{3.15}$$

At maximum output voltage ($q = \frac{\sqrt{3}}{2}$),3.13 and 3.15 are identical. The only difference between the methods is that the right most term is used in conjunction with q in the Venturini method and is fixed at its maximum value in the scalar method. The effect on output voltage is negligible except at low switching frequencies where the Venturini method is superior.

3.2.4 Space Vector Modulation Methods

The space vector modulation method (SVM) is well known in conventional PWM inverters and has its roots in the "Space Phasor" method of representing and analysing 3-phase machines. This method of analysis is particularly popular with workers in the area of field orientated (or vector) control since it allows visualisation of the spatial and time relationships between the resultant current and flux vectors (or space phasors) in various reference frames. The SVM was first used with matrix converters in [17] where a new PWM control technique of Forced Commutated Cycloconverters was introduced based on the space vector representation of the voltages in the complex plane.

3.2.4.1 Space Phasors

The voltage space phasor of the target output voltages is defined, in terms of the line to line voltages, by (3.16).

$$\overrightarrow{\mathbf{V}}_o(t) = \frac{2}{3}(v_{ab} + a v_{bc} + a^2 v_{ca}) \quad \text{where } a = e^{j2\pi/3} \tag{3.16}$$

On an Argand diagram, multiplication by a corresponds to a rotation of 120° and a^2 by 240°. On the same diagram, $\overrightarrow{\mathbf{V}}_o(t)$ is a vector of constant length ($qV_{im}\sqrt{3}$) rotating at frequency ω_o. The basis of the space vector modulation technique is that the possible output voltages for the converter (for each permissible switching state) are expressed in the same form as (3.16). At each sampling instant, the position of $\overrightarrow{\mathbf{V}}_o(t)$ is compared with the possible vectors and the desired output voltage is synthesised by time averaging (within the switching interval) between adjacent vectors to give the correct mean voltage. This is a relatively simple process for a conventional DC link inverter since there are only eight possible switching states. Two of these give zero volts (termed zero vectors) and the others are at the vertices of a regular hexagon. The locations and length of the possible output space vectors are fixed in the case of a DC link inverter. The situation with a Matrix Converter is more complex since there are twenty seven possible switching states and the input voltages are time varying.

3.2.4.2 Matrix Converter Output Space Phasors

The 27 possible switching states for a 3-phase to 3-phase Matrix Converter together with the resulting output voltages are tabulated in Table 3.1.

From this table, the output voltage states may be split into three groups:

Group I Each output line is connected to a different input line
– constant amplitude, rotating (in either direction) at the supply angular frequency

Group II Two output lines are connected to a common input line, the remaining output line is connected to one of the other two input lines
– varying amplitude, fixed position occupying one of 6 positions regularly spaced 60° apart.

Group III All output lines are connected to the same input line
– zero amplitude at the origin

Group	Output phase voltages			Output line to line voltages		
	v_a	v_b	v_c	v_{ab}	v_{bc}	v_{ca}
I	v_A	v_B	v_C	v_{AB}	v_{BC}	v_{CA}
	v_A	v_C	v_B	$-v_{CA}$	$-v_{BC}$	$-v_{AB}$
	v_B	v_A	v_C	$-v_{AB}$	$-v_{CA}$	$-v_{BC}$
	v_B	v_C	v_A	v_{BC}	$-v_{CA}$	v_{AB}
	v_C	v_B	v_A	v_{CA}	v_{AB}	v_{BC}
	v_C	v_B	v_A	$-v_{BC}$	$-v_{AB}$	$-v_{CA}$
IIa	v_A	v_A	v_B	0	v_{AB}	$-v_{AB}$
	v_A	v_A	v_C	0	$-v_{CA}$	v_{CA}
	v_B	v_B	v_A	0	$-v_{AB}$	v_{AB}
	v_B	v_B	v_C	0	v_{BC}	$-v_{BC}$
	v_C	v_C	v_A	0	v_{CA}	$-v_{CA}$
	v_C	v_C	v_B	0	$-v_{BC}$	v_{BC}
IIb	v_B	v_A	v_A	$-v_{AB}$	0	v_{AB}
	v_C	v_A	v_A	v_{CA}	0	$-v_{CA}$
	v_A	v_B	v_B	v_{AB}	0	$-v_{AB}$
	v_C	v_B	v_B	$-v_{BC}$	0	v_{BC}
	v_A	v_C	v_C	$-v_{CA}$	0	v_{CA}
	v_B	v_C	v_C	v_{BC}	0	$-v_{BC}$
IIc	v_A	v_B	v_A	v_{AB}	$-v_{AB}$	0
	v_A	v_C	v_A	$-v_{CA}$	v_{CA}	0
	v_B	v_A	v_B	$-v_{AB}$	v_{AB}	0
	v_B	v_C	v_B	v_{BC}	$-v_{BC}$	0
	v_C	v_A	v_C	v_{CA}	$-v_{CA}$	0
	v_C	v_B	v_C	$-v_{BC}$	v_{BC}	0
III	v_A	v_A	v_A	0	0	0
	v_B	v_B	v_B	0	0	0
	v_C	v_C	v_C	0	0	0

Table 3.1: Switching states for a 3-phase to 3-phase matrix converter

3.2.4.3 Selection of Switching States

The method used to select the vectors to produce the desired output voltage at each sampling instant is not unique. A simple method is described here. Other more complex methods, giving better performance are possible [18] but the underlying concept is the same.

The rotating vectors of Group I are not used. Group II vectors are split into three sub-groups as shown in Table 3.1. The six states in each sub-group produce a space phasor along a defined direction. For the three sub-groups the directions are mutually displaced by 120°. The amplitude and polarity of the space phasor along the defined direction depends on which of the line to line voltages is used. This yields the hexagon of possible vectors shown in Figure 3.6 For example, subgroup IIa can produce vector 1 or 4. A number of switching states will produce each of these vectors but at any instant in time only one choice of switching state (for each vector) will maximise the length of the vector. This occurs when the input line to line voltage that is selected is the one with the maximum amplitude and the output therefore follows the rectified envelope of the input voltages (Figure 3.5).

For example, consider a time when v_{ab} is the most positive line to line voltage. Selecting the first state in subgroup IIa will produce a maximum length vector in direction 1 – selecting the third state in subgroup IIa will produce a vector in direction 4. Similarly, selecting the first state in subgroup IIb will produce a maximum length vector in direction 3 and so on. Only the maximum length vectors in each of the directions 1 to 6 are used in this simple example. The length of these vectors is $\frac{2}{\sqrt{3}}V_{env}$ where V_{env} is the instantaneous value of the rectified envelope.

To determine the modulation times, the position and length of the desired output voltage vector, $\overrightarrow{\mathbf{V}}_o(t)$, is determined at the start of the sampling interval (T_{seq}). The correct output voltage is then synthesised by switching between the two adjacent maximum length vectors from group II and one or more of the zero vectors from group III. For example, consider a time when $\overrightarrow{\mathbf{V}}_o(t)$ lies in the sextant between vector

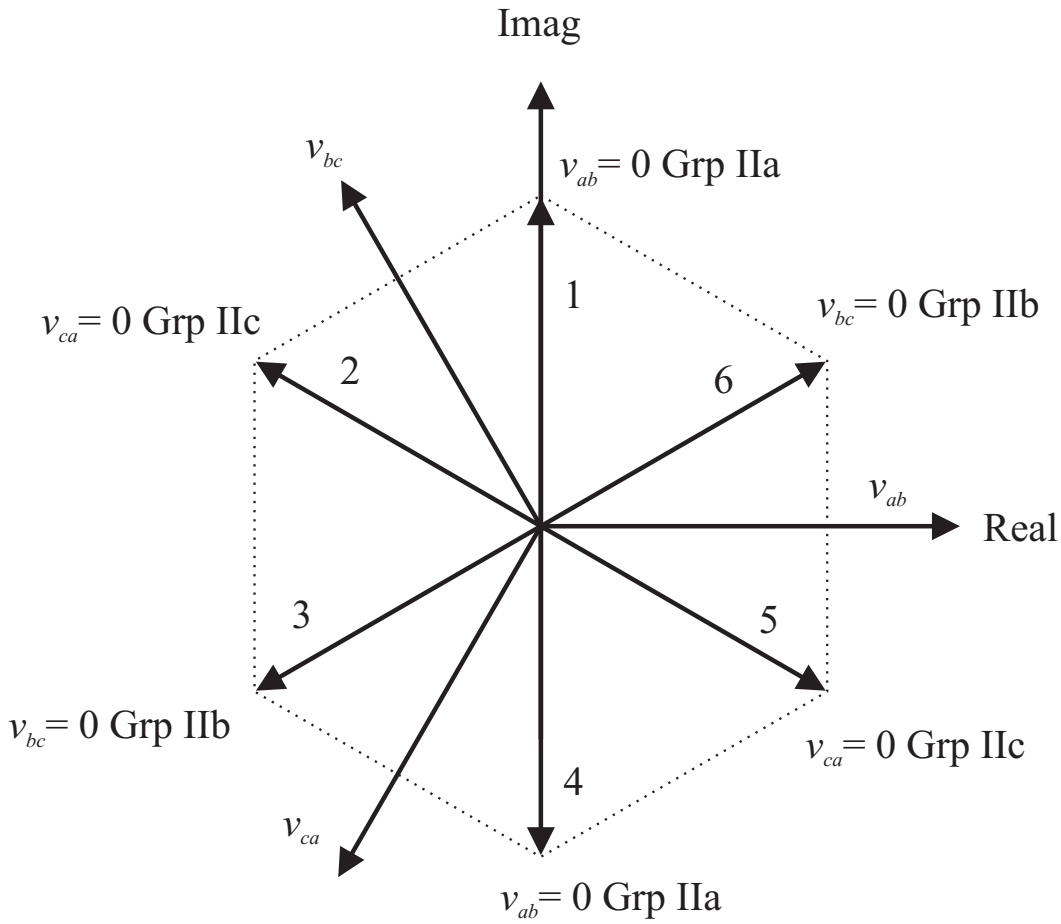

Figure 3.6: Output voltage space vectors

1 and vector 6 as depicted in Figure 3.7. $\overrightarrow{\mathbf{V}}_o(t)$ is generated from a weighted sum of

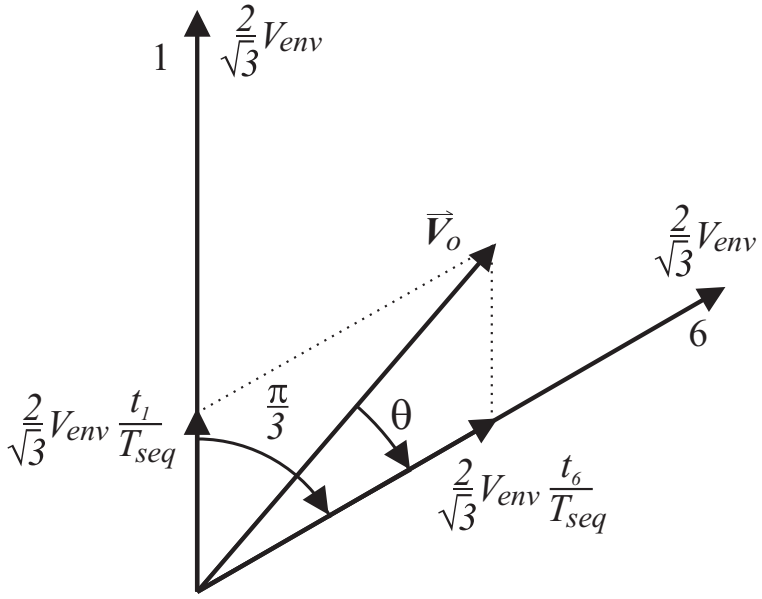

Figure 3.7: Synthesis of output voltage space phasor

the 1 and 6 vectors. The weighting is achieved through time averaging by choosing the time spent in vector 1 (t_1) and vector 6 (t_6) during the switching sequence. from Figure 3.7 (applying the sine rule) the relationship in (3.17) is found.

$$\frac{2}{\sqrt{3}}\frac{t_1}{T_{seq}}\frac{V_{env}}{\sin(\theta)} = \frac{2}{\sqrt{3}}\frac{t_6}{T_{seq}}\frac{V_{env}}{\sin(\frac{\pi}{3}-\theta)} = \frac{\overrightarrow{\mathbf{V}}_o}{\sin(\frac{2\pi}{3}-\theta)} \tag{3.17}$$

which yields:

$$t_1 = \frac{\overrightarrow{\mathbf{V}}_o}{V_{env}}T_{seq}\sin(\theta) \qquad \text{and} \qquad t_6 = \frac{\overrightarrow{\mathbf{V}}_o}{V_{env}}T_{seq}\sin(\frac{\pi}{3}-\theta)) \tag{3.18}$$

then:

$$t_0 = T_{seq} - (t_1 + t_6) \tag{3.19}$$

where t_0 is the time spent in the zero vector.

There is no unique way in which the times (t_1, t_6, t_0) have to be distributed within the switching sequence. A method suggested by some authors is to arrange them symmetrically with the zero state in the middle as shown in Figure 3.8. However, several

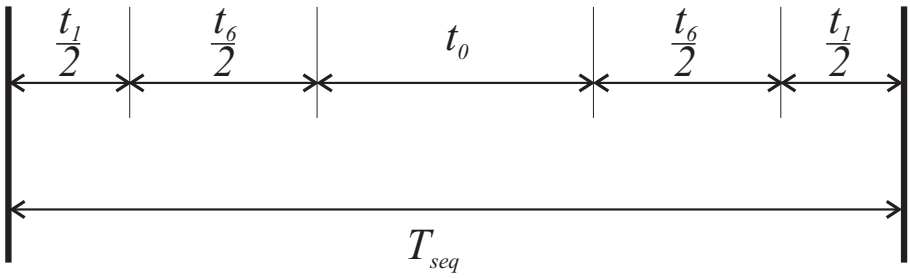

Figure 3.8: Possible way of allocating states within the switching sequence

variations of the space vector modulation method have been proposed [19, 18]. These more sophisticated methods take into account the desired input current direction making it possible to draw sinusoidal input currents with controllable displacement factor.

3.2.5 Indirect Modulation Methods

These methods aim to increase the maximum voltage ratio above the 86.6% limit of other methods [20] and [21]. To do this the modulation process expressed in terms of output phase voltage defined in (3.3) is split into two steps as indicated in (3.20)

$$[v_o(t)] = ([A(t)][v_i(t)])[B(t)] \tag{3.20}$$

In (3.20), premultiplication of the input voltages by $[A(t)]$ generates a "fictitious dc link" and postmultiplication by $[B(t)]$ generates the desired output by modulating the "fictitious dc link". $[A(t)]$ is generally referred to as the "rectifier transformation" and $[B(t)]$ as the "inverter transformation" due to the similarity in concept with a traditional rectifier/dc link/inverter system. $[A(t)]$ is given by (3.21)

$$[A(t)] = K_A \begin{bmatrix} \cos(\omega_i t) \\ \cos(\omega_i t + \frac{2\pi}{3}) \\ \cos(\omega_i t + \frac{4\pi}{3}) \end{bmatrix}^T \tag{3.21}$$

Hence,

$$[A(t)][v_i(t)] = K_A V_{im} \begin{bmatrix} \cos(\omega_i t) \\ \cos(\omega_i t + \frac{2\pi}{3}) \\ \cos(\omega_i t + \frac{4\pi}{3}) \end{bmatrix}^T \begin{bmatrix} \cos(\omega_i t) \\ \cos(\omega_i t + \frac{2\pi}{3}) \\ \cos(\omega_i t + \frac{4\pi}{3}) \end{bmatrix} = \frac{3K_A V_{im}}{2} \tag{3.22}$$

$[B(t)]$ is given by (3.23)

$$[B(t)] = K_B \begin{bmatrix} \cos(\omega_o t) \\ \cos(\omega_o t + \frac{2\pi}{3}) \\ \cos(\omega_o t + \frac{4\pi}{3}) \end{bmatrix} \tag{3.23}$$

Hence,

$$[v_o(t)] = ([A(t)][v_i(t)])[B(t)] = \frac{3K_A K_B V_{im}}{2} \begin{bmatrix} \cos(\omega_o t) \\ \cos(\omega_o t + \frac{2\pi}{3}) \\ \cos(\omega_o t + \frac{4\pi}{3}) \end{bmatrix} \tag{3.24}$$

From (3.24) the voltage ratio is $q = \frac{3K_A K_B V_{im}}{2}$. The $[A(t)]$ and $[B(t)]$ must be implemented by a suitable choice of the switching states. There are many ways of doing this, which are discussed in detail in [20] and [21]. To maximise the voltage ratio, the step in $[A(t)]$ is implemented so that the most positive and most negative input voltages are selected continuously. This yields $K_A = \frac{2\sqrt{3}}{\pi}$ with a "fictitious dc link" of $\frac{3\sqrt{3}V_{im}}{\pi}$. K_B represents the modulation index of a PWM process and has the maximum value of $\frac{2}{\pi}$ [20]. The overall voltage ratio q therefore has the maximum value of $\frac{6\sqrt{3}}{\pi^2} = 105.3\%$.

The maximum voltage ratio obtainable is obviously greater than that of other methods but the improvement is obtained at the expense of the quality of either the input currents, the output voltages or both. For values of $q > 0.866$, the mean output voltage no longer equals the target output voltage in each switching interval. This inevitably leads to low frequency distortion in the output voltage and/or the input current compared to other methods with $q < 0.866$. For $q < 0.866$, the indirect method yields very similar results to the direct methods.

3.3 Device characteristics and properties overview

In this section an overview of the power devices currently in use is given with particular attention to their maximum ratings and main features. A diagram showing the present approximate maximum device ratings for the different types of power device topology under review can be seen in Figure 3.9.

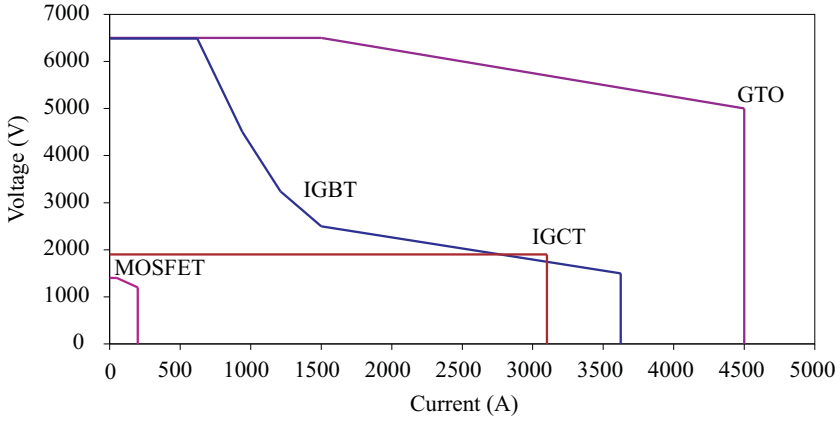

Figure 3.9: Ratings of currently available power semiconductor devices

The MOSFET (Metal-Oxide-Semiconductor Field Effect Transistor) is a voltage controlled device which is turned on when the voltage between gate and source is large enough (max +/- 20V) and off when the gate-source voltage is below the threshold value. The switching times of a MOSFET can be very short in the range of a few

nanoseconds to a few hundreds nanoseconds according to the charge. Therefore MOSFET is capable of high switching frequencies. Although the fast switching speed lead to low switching losses, MOSFETs are characterised by high conduction losses due to an on-state resistance between the drain and the source which increases rapidly with the device blocking voltage rating. This is the main reason why MOSFET application in power electronics is limited to low voltage power converters.

The GTO (Gate-Turn-Off Thyristors) has become the standard power device for high power applications due to its thyristor like carrying capability. The GTO is manufactured as an array of cathode elements to permit good gate access to the conducting regions. This enables the device to be depleted evenly during the turn-off process. Unbalanced current sharing during turn off can cause high local dissipation and possible device failure. It is for this reason that the GTO must utilise snubber circuits to limit the rate of rise of anode voltage and hence prevent localised device stress. This snubber arrangement causes high switching losses and hence the GTO can only be used at low switching frequencies. Many manufacturers also specify minimum on and off times for these devices which may distort the converter output waveforms.

The IGBT (Insulated Gate Bipolar Transistor) is a power device which combines some of the advantages of MOSFET, BJT and GTO. Like the MOSFET, the IGBT has a high impedance gate which requires only a small amount of energy to switch the device while it is characterised by a small on-state voltage as its main conduction path is that of the BJTs. Besides this the IGBT can be designed to block negative voltages similar to the GTO (known as reverse blocking IGBTs). Current IGBT's ratings show their improved power capability and given the appealing characteristics it is not surprising if it results the most popular power semiconductor switching device for AC variable speed drive applications. The last generation of IGBT chip, the Field Stop (Trench) IGBT combines the advantages of Non Punch Through (NPT) IGBTs by further minimising both static and dynamic losses together with a higher current density capability.

The IGCT (Integrated Gate Commutated Thyristor) is used in medium voltage, high power converters developed by ABB for motor drive applications. The IGCT consists of a separate gate driver and gate commutated thyristor. The structure of the gate commutated tyristor is very similar to the GTO except that an anti-parallel diode is integrated into the same silicon wafer. Improvements in the structure of the multitude of cathode elements in the device have led to improved current sharing at turn off and, according to the manufacturer, this removes the need for snubber circuits unlike the standard GTO. The silicon substrate from which the IGCT is constructed is also thinner than the standard GTO. This enables the integration of the diode and reduces the amount of stored charge present in the device at turn off and hence switching times and losses are reduced. The supplied gate drivers also simplify the design of power systems since these require only logic level signals. These gate drivers however are large and the construction of a compact power circuit would be difficult.

The Silicon is today the leading base material for power semiconductor devices but new material such as Silicon Carbide (SiC) and Gallium Nitride (GaN) have the potential to produce a new generation of semiconductor devices which would influence many sectors of the industry. The key point is in the properties of these new materials. Particular attention has been given in the last decade to SiC a wide bandgap material that promises to offer devices with lower conduction losses, higher junction temperatures, higher power densities and higher voltage operation. It is indeed a reality for diodes which can be purchased from different manufacturers offering a new degree of freedom in the design of power circuits [22]. It is for automotive and aerospace applications that SiC power devices will offer the major advantages. At a device level silicon will always be very competitive with respect to other materials, looking especially at its cost performance ratio and technological improvements. At a system level with a growing demand for increased power density, crucial when space and weight are important issues, the larger range of operating temperatures SiC devices could be the better alternative in the near future. The current work on SiC power switches is focused on MOSFET type devices and Junction Field Effect Transistors (JFET). The successful development of these devices will be applied to other devices such as IGBTs.

3.4 Bidirectional Switch Structures

The matrix converter requires a bi-directional switch capable of blocking voltage and conducting current in both directions. Unfortunately there are no such devices currently available that fulfil these needs; so discrete devices need to be used to construct suitable bi-directional switch cells. The choice of bi-directional switches also dictates which current commutation methods can be used. This section describes some possible bi-directional switch configurations and the advantages and disadvantages of each arrangement. In the discussion below it has been assumed that the switching device would be an IGBT, but other devices such as MOSFETs, MCTs and IGCTs can be used in the same way.

3.4.1 Diode Bridge Bi-directional Switch

The most simple bi-directional switch structure is the diode bridge bi-directional switch cell. This arrangement consists of an IGBT at the centre of a single phase diode bridge arrangement and is shown in Figure 3.10. The main advantage of this

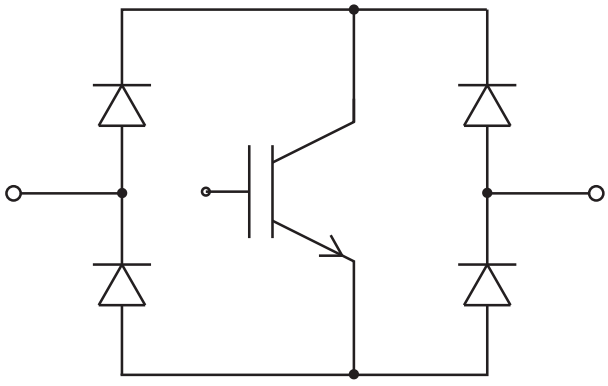

Figure 3.10: Diode bridge bi-directional switch

arrangement is that only one active device is needed, reducing the cost of the power circuit and the complexity of the control/gate drive circuits. Conduction losses are

relatively high since there are three devices in each conduction path. The direction of the current through the switch cannot be controlled. This is a disadvantage, as many of the advanced commutation techniques described later in Section 3.6.1 rely on independent control of the current in each direction.

3.4.2 IGBT with Anti-parallel Diode Configurations

3.4.2.1 Common Emitter Bi-directional Switch

This switch arrangement consists of two diodes and two IGBTs connected in anti-parallel as shown in Figure 3.11. The diodes are included to provide the reverse

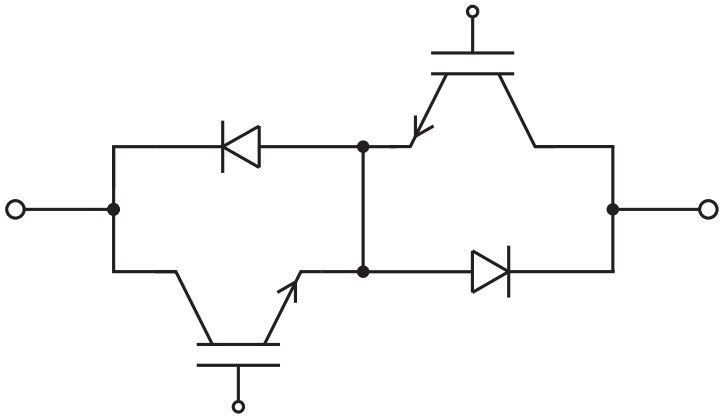

Figure 3.11: Common Emitter bi-directional switch

blocking capability. There are several advantages in using this arrangement when compared with the diode bridge switch. The first is that it is possible to independently control the direction of the current. Conduction losses are also reduced since only two devices carry the current at any one time. As with the diode bridge switch each bi-directional switch cell requires an isolated power supply.

3.4.2.2 Common Collector Bi-directional Switch

This arrangement is similar to the previous one but the IGBTs are arranged in a common collector configuration as shown in Figure 3.12. The conduction losses are

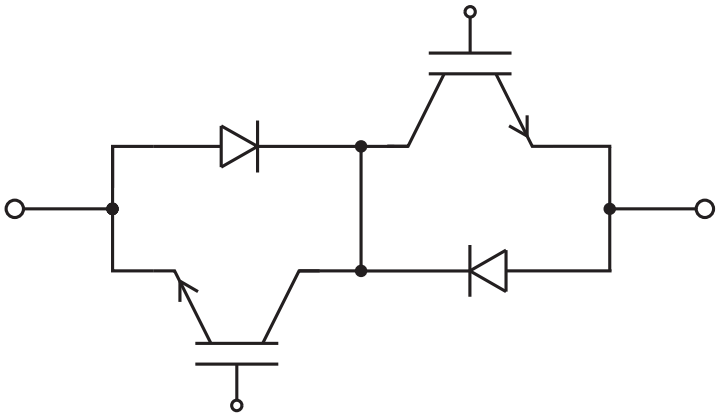

Figure 3.12: Common Collector bi-directional switch

the same as the common emitter configuration. A possible advantage of the common collector configuration is that only six isolated power supplies are needed to supply the gate drive signals. This is possible if the inductance between the devices sharing the same isolated power supply is low which is the case for matrix converter modules where all the bi-directional switches are integrated in one package [23]. However, as the power levels increase, the stray inductance of the individual bi-directional switches becomes more important. Therefore at higher power converters it is desirable to package the IGBTs into individual bi-directional switches or complete output legs. Hence the common emitter configuration is usually preferred for higher power levels [24].

3.4.2.3 Series IGBT Diode Configurations

Both the common emitter and common collector configurations can be used without the central connection, as shown in Figure 3.13. In the case of the common emitter configuration, this will remove the advantage of being able to drive the two IGBTs from the same isolated supply.

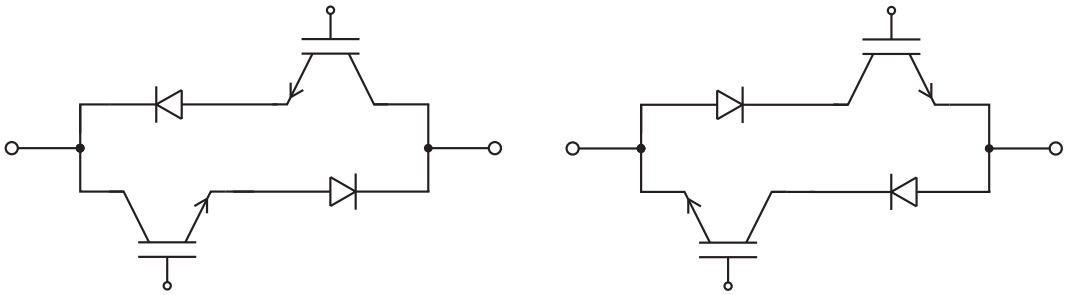

(a) Common Emitter (b) Common Collector

Figure 3.13: Back to back devices without central connection

3.4.2.4 Anti-parallel Reverse Blocking IGBTs

If the switching devices used for the bi-directional switch have a reverse voltage blocking capability then it is possible to build the bi-directional switches by simply placing two devices in anti-parallel as shown in Figure 3.14. This arrangement leads to a very compact converter with the potential for substantial improvements in efficiency. However, to date reverse blocking IGBTs have shown poor reverse recovery characteristics which decreases the efficiency by increasing the switching losses and has prevented widespread use of this configuration.

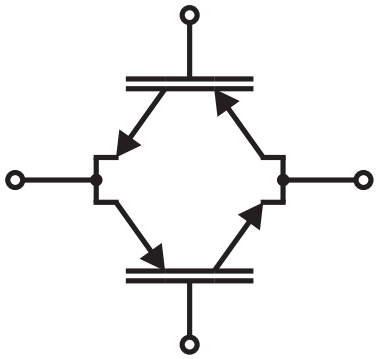

Figure 3.14: Reverse blocking IGBT bi-directional switch

3.5 Commutation Techniques

Reliable current commutation between switches in matrix converters is more difficult to achieve than in conventional voltage source inverters (VSI) since there are no natural freewheeling paths. The commutation has to be actively controlled at all times with respect to two basic rules. This can be visualised by considering just two switches on one output line of a Matrix Converter. It is important that no two bi-directional switches are switched on at any one time, as shown in Figure 3.15(a). This would result in line-to-line short circuits and the destruction of the converter due to overcurrent. Also, the bi-directional switches for each output phase should not all be turned off at any point in time, as shown in Figure 3.15(b). This would result in the absence of a path for the inductive load current, causing large over-voltages. These two considerations cause a conflict since semiconductor devices cannot be switched instantaneously due to propagation delays and finite switching times.

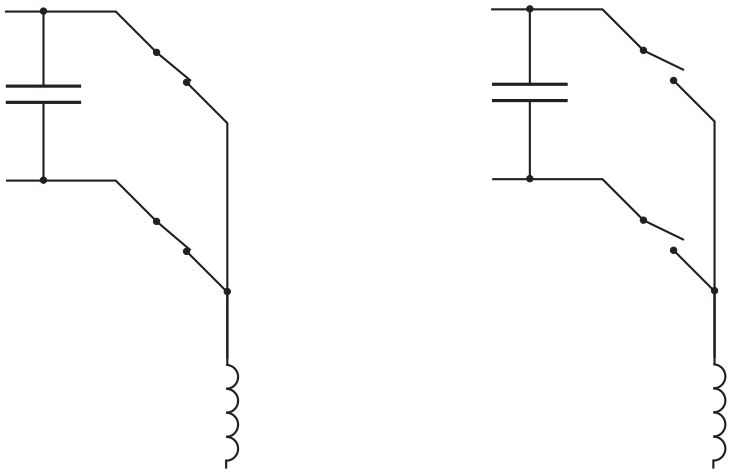

(a) Short circuit of capacitive input (b) Open circuit of inductive load

Figure 3.15: These conditions must be avoided for safe operation

3.5.1 Simple Commutation

3.5.1.1 Deadtime Commutation

The deadtime method is commonly used in inverter circuits. The load current freewheels through the anti-parallel diodes during the deadtime period. In the case of a Matrix Converter using deadtime commutation will cause an open circuit of the load (Figure 3.15(b)). This will result in large voltage spikes across the switches which would destroy the converter unless snubbers or clamping devices are used to provide a path for the load current during the deadtime period [25, 26]. This method is undesirable since the energy in the snubber circuit is lost during every commutation. In addition to this the bi-directional nature of the Matrix Converter circuit further complicates the snubber design.

3.5.1.2 Overlap Commutation

This method also breaks the rules of Matrix Converter current commutation and needs extra circuitry to avoid destruction of the converter. In overlap current commutation, the incoming switch is turned on before the outgoing one is turned off. This will cause a line to line short circuit during the overlap period unless extra line inductance is added to slow the rise of the current [27]. This is not a desirable method since the inductors are in the main conduction path so the conduction losses would be increased. In addition to this there will be significant distortion of the output voltage waveform during the overlap period. The switching time for each commutation is increased and will vary with commutation voltage which may cause control problems.

One possible advantage of these simple commutation methods is that the diode bridge bi-directional switch arrangement, as described in Section 3.4.1, may be used. However, this advantage is outweighed by the problems discussed above. For these reasons the advanced commutation methods described below are now preferred in all Matrix Converters.

3.6 Advanced Commutation Methods

A reliable method of current commutation, which obeys the rules, uses a four-step commutation strategy in which the direction of current flow through the commutation cells can be controlled. To implement this strategy the bi-directional switch must be designed in such a way as to allow the direction of the current flow in each switch to be controlled.

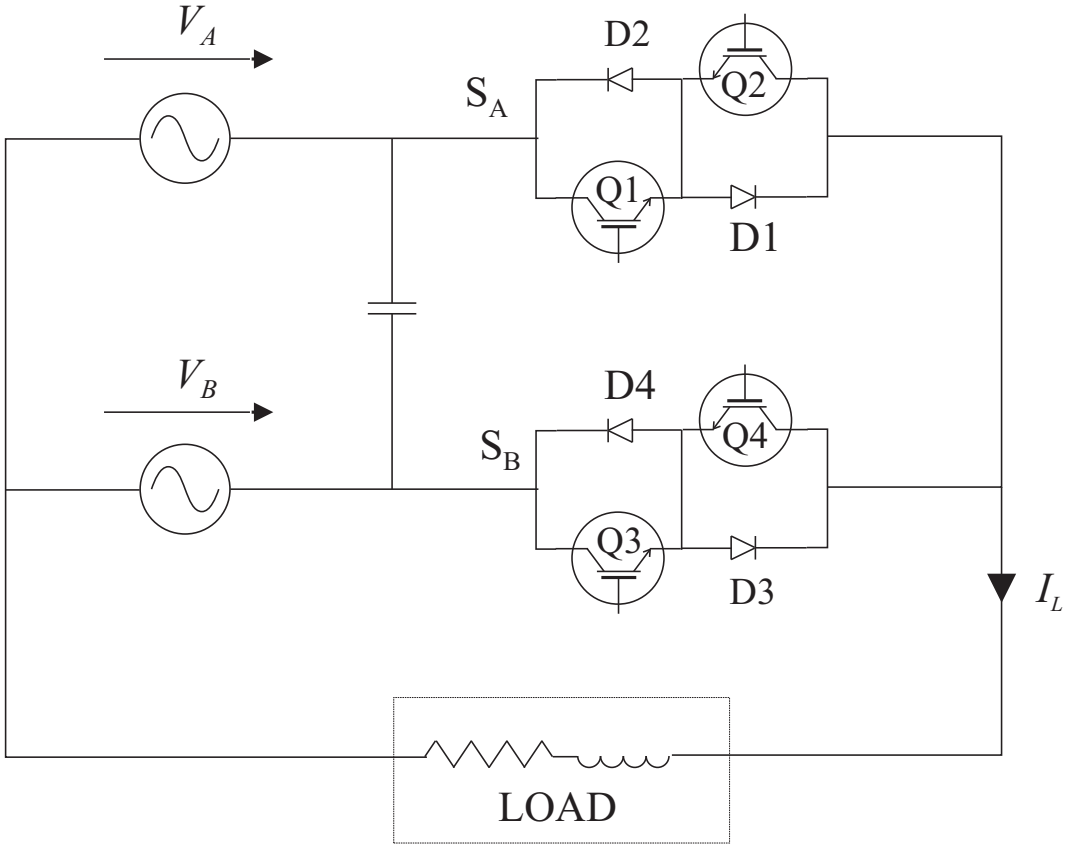

Figure 3.16: 2-phase to 1-phase converter

3.6.1 Current Direction Based Commutation Method

Figure 3.16 shows a schematic of a two phase to single phase matrix converter. In steady state both of the devices in the active bi-directional switch are gated to allow both directions of current flow. The following explanation assumes that the load current is in the direction shown and that the upper bi-directional switch (S_A) is closed. When a commutation to S_B is required, the current direction is used to determine which device in the active switch is not conducting. This device is then turned off. In this case Q2 is turned off. The device that will conduct the current in the incoming switch is then gated, Q3 in this example. The load current transfers to the incoming device either at this point or when the outgoing device (Q1) is turned off depending on the polarity of the input voltage. The remaining device in the incoming switch (Q4) is turned on to allow current reversals. This process is shown as a timing diagram in Figure 3.17, the delay added between each switching event is determined by the device characteristics. If a mistake is made as to the current direction either due to circuit failure or due to the uncertainty at low currents, an open circuit in the load current will result. This can be a problem if no protection strategy is employed but can be an advantage over some commutation strategies if the correct protection strategy is employed (Section 5.1.4.

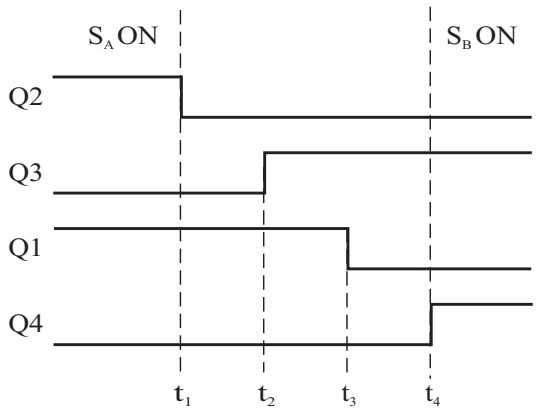

Figure 3.17: Timing diagram for four-step current commutation between two switches

A variation on the four-step current commutation concept is to only gate the conducting device, which creates a two-step current commutation strategy as shown in Figure 3.18. This is done to reduce commutation times and hence reduce the minimum pulse width. This is desirable because the minimum pulse width often dictates the maximum voltage transfer ratio of the converter [28].

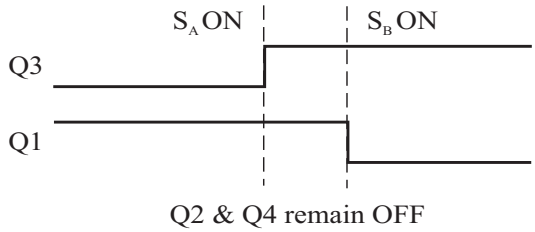

Figure 3.18: Timing diagram for two-step current commutation between two switches

All the current commutation techniques in this category rely on knowledge of the output line current direction. This can be difficult to reliably determine in a switching power converter, especially at low current levels in high power drives. To avoid this problem a technique for using the voltage across the bi-directional switch to determine the current direction has been developed [29]. This technique provides a reliable commutation achieved using an intelligent gate drive circuit which controls the firing of the IGBTs and detects the direction of current flow within the bidirectional switch cell. The current direction information calculated by the active gate drive via the use of an FPGA controller is passed to all of the other gate drivers on the same output phase. In this way it is ensured that all the gate drivers contribute to operate a safe commutation. This method, like all two step strategies, offers poor performance and causes a distortion in the output waveform when the load current is low. In this condition there is not enough load current to turn the outgoing device off and incoming device on effectively. This is not a problem for the four-step method since the final step of turning on the non-conducting incoming device completes the commutation.

3.6.2 Voltage Magnitude Based Commutation Method

The second advanced commutation strategy uses measurements of the input voltage magnitude to determine the switch sequence for each commutation [30]. Referring to Figure 3.16 consider a commutation from S_A to S_B if $V_A > V_B$, Q3 can be turned on because D3 is reverse biased. If the current is in the direction shown it will commutate to Q3 when Q1 is turned off, otherwise the commutation will take place when Q4 is turned on. The reverse biased device (Q2) can then be turned off completing the commutation. In contrary to the current direction based commutation technique, if a mistake as to the voltage input direction is made, the resulting commutation sequence will cause a line to line short circuit of the input supply. This can be difficult to protect against.

The two-step variant of the voltage magnitude based commutation method proposed in [31] is different in that only the devices needed to prevent shoot-through are turned off. The implementation of this method requires accurate measurement of the supply voltages. This can lead to difficulties at the zero crossing points of the line to line voltages as any inaccuracy in voltage measurement could cause the wrong commutation sequence to be used. The later work in [32] shows a method of providing a path for the current during these periods but commutation between certain phases is inhibited. The critical and uncritical areas of commutation are shown in Figure 3.19.

A technique to avoid critical situations of commutation, such as when two voltages of the input phases become equal, is discussed in [33]. This technique is based on the concept of replacing the critical commutation sequence with two uncritical sequences which will commutate to the remaining third input phase and then to the desired destination phase. Figure 3.20 explains the proposed sequence replacement.

Although the method is effective and easy to implement in the commutation logic a clear disadvantage comes from the extra sequences which are inserted because it will increase the switching losses of the converter.

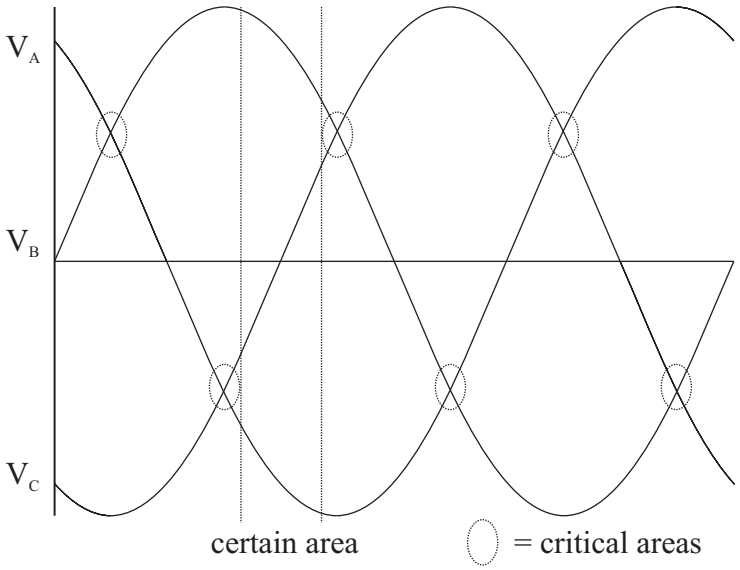

Figure 3.19: Critical areas of commutation sequence selection

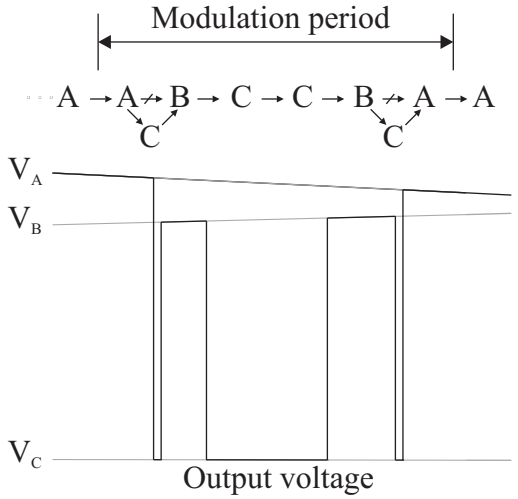

Figure 3.20: Critical areas between phase A and B - Two additional sequences to phase C are inserted in the modulation period

3.6.3 Voltage Magnitude and Current Direction Commutation Method

The commutation method proposed in [34] uses a combination of current direction and input voltage magnitude measurement. The principle idea is to turn on all the devices that will conduct in the same direction as the load current. Commutation between the three phases can be achieved by turning off one, or two of the devices simultaneously depending on the required switching state and the relative magnitude of the input voltages. This is a one-step commutation method as there is no need for staggered switch sequencing.

Although this method benefits from the advantages of both the current direction and the voltage magnitude based methods it also retains some of the disadvantages from both:

- At zero crossing points of line currents, small inaccuracies in input voltage measurement will result in commutation to the wrong input phase and lead to input current distortion.
- As only the devices that conduct in one direction are turned on there is no path for the current to reverse. This will result in distortion on the output waveforms at the zero crossing points of the load current [35].

3.6.4 Time Gap Regulation Current Commutation

This commutation method does not rely on output current direction or input voltage measurement. The principle is to adjust the deadtime/overlap online to minimise both the voltage overshoot and current shoot-through at each commutation [36]. This method is of academic interest, but it has some undesirable problems in implementation.

3.6.5 Commutation without explicit sign measurement

The matrix converter commutation method without explicit sign measurement is discussed in [37]. It proposes an alternative technique to avoid the critical switching patterns in the critical areas shown in Figure 3.19. The basic idea of this technique is that instead of adding sequences as it was for the "replacement" method in [33] in a critical area, the modulation patterns are reshuffled in such a way that no critical sequence appears. This is clarified by Figure 3.21, where the sequence $A \rightarrow B \rightarrow C$ is rearranged to the sequence $A \rightarrow C \rightarrow B$ avoiding the critical step $A \rightarrow B$.

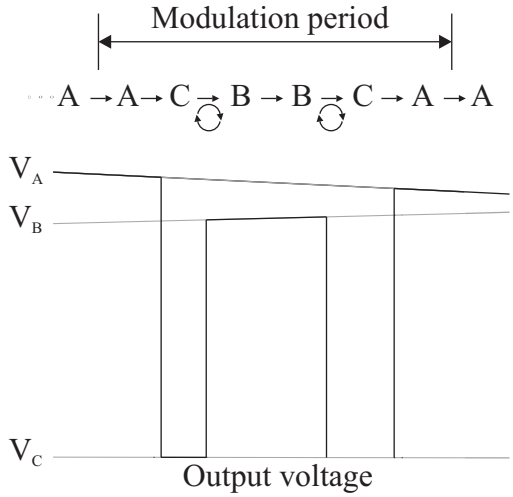

Figure 3.21: Critical areas between phase A and B - The switching patterns are rearranged

To implement this technique it must be considered that because no sign measurements are involved the information on the critical and uncritical areas as well as the voltage signs are deduced from the measured voltage signals. To do this two ways are highlighted in [37]. One possibility is to replace the exact sign detection circuit with high resolution A/D converters and to increase the processor sample rate which can lead to an expensive solution. An other possibility is to use an FPGA for PWM generation, commutation logic, sign detection and A/D converter control and the DSP to operate the sampling of the voltage signal independently from the demands of the PWM generation. Sigma-delta-converters for the A/D conversion are imple-

mented and filtering of the measured bit stream is provided to analyse the value of the input voltage. One problem highlighted in [37] which could occur with the "prevention" method is when a critical area is detected within a modulation period. In this case it is not possible to rearrange the commutation sequence which has already started. The combination of both the "replacement" and "prevention" methods is therefore proposed as a solution for an effective commutation technique without sign measurement.

The main disadvantage of this technique is that the switching sequence desired by the modulation algorithm is effectively altered by the PWM generator. Clearly this is done to provide safe commutations during the six critical points per supply cycle. This may introduce low order harmonics in the output voltage and input current spectra which may further complicate the design of the input filter. This method would also be unsuitable for modulation techniques that do not cycle through the input phases in turn such as some space vector modulation techniques.

3.6.6 Soft Commutation Techniques

There has been some interest in the application of resonant, zero voltage or zero current switching in matrix converter circuits to reduce the losses and increase switching frequencies. To date all of the suggested circuit topologies have significant disadvantages as well as increased component count. The soft switching circuits can be generally separated into two groups. The first is where the soft switching or resonant components are included as part of each of the bi-directional switches. The second group have auxiliary resonant components on each output phase of the matrix converter and have the advantage of reducing the component count. The following Sections discuss some of these soft switching techniques.

3.6.6.1 Diode Bridge Soft Switched Arrangement

This bi-directional soft switch cell shown in Figure 3.22 was proposed in [38]. It consists of a diode bridge arrangement with a uni-directional central switch circuit. This uni-directional switch consists of two IGBTs and two diodes arranged in parallel with their mid points connected with a uni-directional capacitor. There is also an inductor in series with this central switch cell. Both Q1 and Q2 are gated together and the incoming and outgoing switch cells are turned on and off respectively at the same time.

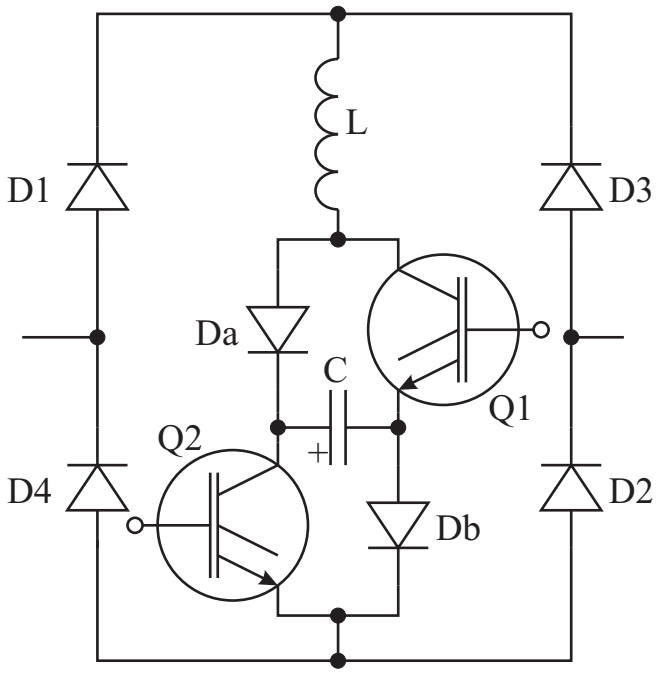

Figure 3.22: Diode bridge soft switch cell

The circuit operation is as follows. At turn on the capacitor C is initially charged in the direction shown reverse biasing diodes Da and Db. The two IGBTs Q1 and Q2 are gated simultaneously. The current in the switch increases slowly because of the series inductor. This causes zero current turn on of the devices. The path for the load current is through L, Q1, Q2 and C. This continues to be the path for the load current until the voltage across C has fallen to a level preventing the reverse biasing

of diodes Da and Db. These diodes then conduct and the load current path is then through L, Da, Q2, Db and Q1. This completes the turn on process.

The devices Q1 and Q2 are also turned off simultaneously. The capacitor voltage then rises slowly due to the load current. This causes the devices to turn off under zero voltage conditions. The capacitor voltage continues to rise until the load current is provided by another switch and the energy in the inductor has been removed. This ends the turn off process and the capacitor is charged ready for the next turn on.

This method has been shown to almost eliminate switching loss. Conduction losses are increased, however, due to the increase in devices in the conduction path compared to a back to back IGBT/diode configuration. This method also massively increases the component count. This method would require a total of fifty four diodes to construct a three phase to three phase matrix converter compared to eighteen using non-resonant techniques. This may hamper the construction of a commercial product. The inductor in each bi-directional switch cell also has to carry the whole load current for its period of conduction, making it large and expensive. This would remove the space advantage of the matrix converter since nine of these inductors are needed for a three phase to three phase matrix converter.

3.6.6.2 Auxiliary Resonant Commutated Pole Circuit

The Auxiliary Resonant Commutated Pole Circuit is the Matrix Converter equivalent of the Auxiliary Resonant Commutated Pole inverter [39]. Although it is reported that this technique works, only simulation results have ever been published and the circuit requires a significant increase in the number and size of passive components, particularly due to the resonant inductors being placed in the primary current path. The circuit is shown in Figure 3.23.

The circuit consists of a resonant capacitor placed across each bi-directional switch in the main matrix converter circuit and a resonant inductor in series with an auxiliary switch across each output phase. The main switches operate under zero voltage

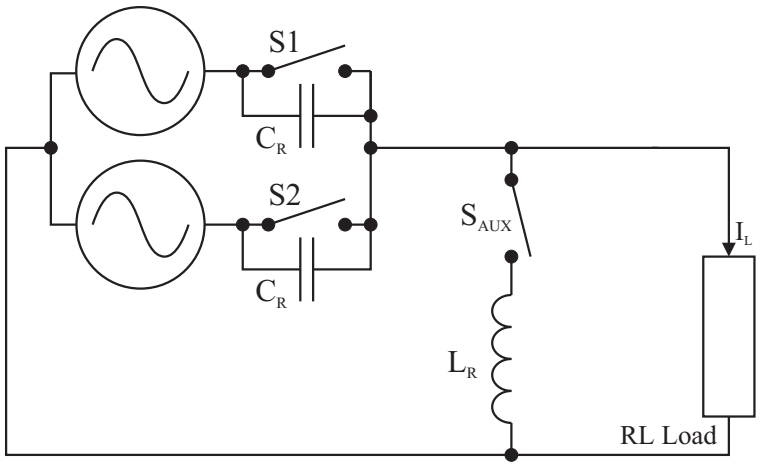

Figure 3.23: Auxiliary Resonant commutated pole circuit

conditions, with the auxiliary switch operating under zero current conditions. The auxiliary switch in the resonant circuit has to be bi-directional and additional voltage stress is placed on the main switching devices. Special control algorithms are also required when using this technique. However, this is currently the most promising of the published soft switching techniques for matrix converters.

3.6.6.3 Zero Current Switching Auxiliary Circuit

The Zero Current Switching Auxiliary Circuit [40] is shown in Figure 3.24. A resonant stage is simply connected across the load. The current in this circuit resonates causing the current in the active switch to be zero periodically. The commutation strategy then relies on the conduction path being passed between switches during the zero current periods. This restriction limits the time when the converter can be switched, reducing controllability. The circuit also suffers from increased device stresses, increased conduction losses and operational problems under low load conditions.

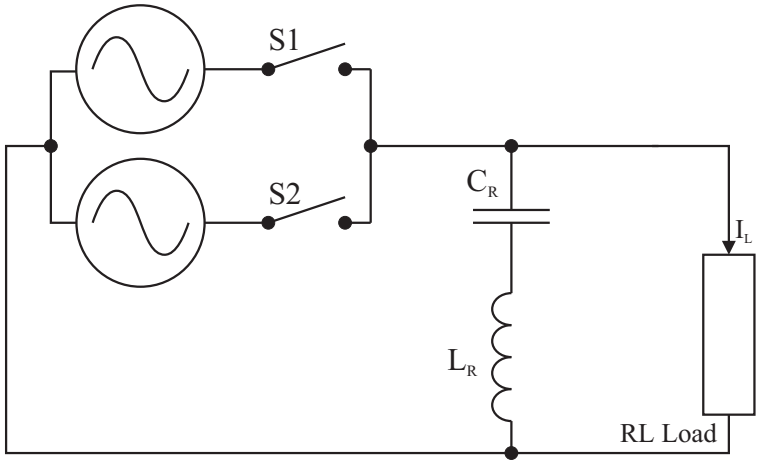

Figure 3.24: Zero current switching auxiliary circuit

3.6.6.4 Zero Voltage Switching Auxiliary Circuit

The Zero Voltage Switching Auxiliary Circuit [41] is shown in Figure 3.25. This is the resonant voltage equivalent of the Zero Current Switching Auxiliary Circuit discussed above. The circuit has the same limitations, with the additional disadvantage of having the resonant inductor in series with the load and therefore carrying the full load current. To date only simulation results of this circuit have been published.

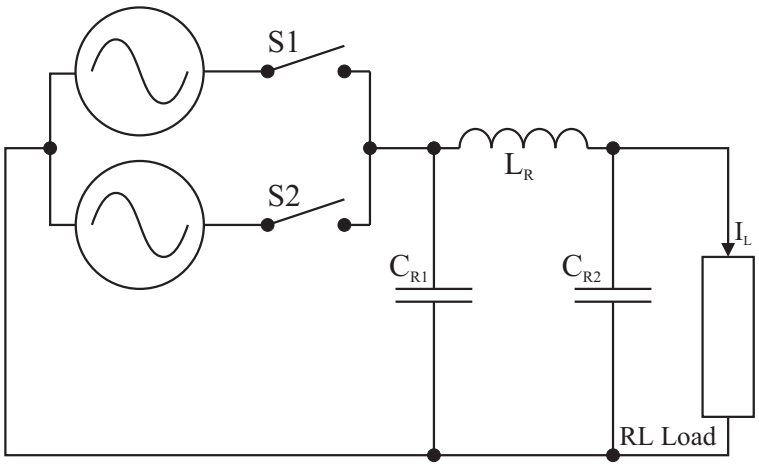

Figure 3.25: Zero voltage switching auxiliary circuit

3.7 Matrix Converter Reliability Study

As part of the EDAAS project, a reliability analysis was performed to determine whether the matrix converter is inherently more or less reliable than other standard drive topologies used in the aircraft industry. Several rectifier-inverter and matrix converter topologies were compared. The military handbook MIL-HDBK-217F [42] guidelines have been used to predict reliability. The matrix converter has several attractive features for aerospace applications such as potential size and weight savings. Although the matrix converter has a higher number of semi-conductor switches, they are subjected to a lower voltage stress, which decreases their failure rate. The following section will outline the circuits analysed, the prediction method and the predicted mean time before failure (MTBF) of the different topologies.

3.7.1 Drive Topologies Analysed

The drive topologies analysed are listed below:

- 6-Pulse diode bridge rectifier and PWM-inverter
- 12-Pulse diode bridge rectifier and PWM-inverter
- 18-Pulse diode bridge rectifier and PWM-inverter
- PWM-rectifier and PWM-inverter
- Matrix converter

Figure 3.26 shows a conventional drive topology using a 6-pulse diode rectifier bridge, connected via a DC-link capacitor to a PWM (Pulse Width Modulation) inverter. Depending on the harmonic specification, relatively complex and bulky tuned filters may be required to filter the low frequency 5th and 7th harmonics. This is further

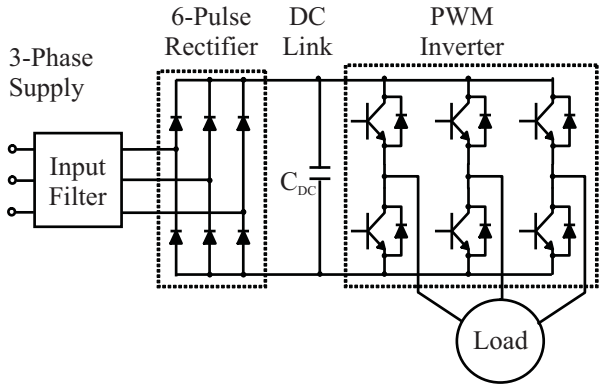

Figure 3.26: Six-pulse diode bridge rectifier and PWM inverter, linked using a DC-link capacitor

complicated due to the introduction of variable frequency (360-800Hz) supply voltage in future civil or cargo aircraft, for which tuned filters are not generally practical.

An effective way of cancelling the 5th and 7th harmonics is to use a 12-pulse rectifier with an autotransformer as shown in Figure 3.27 [43]. The use of this type of trans-

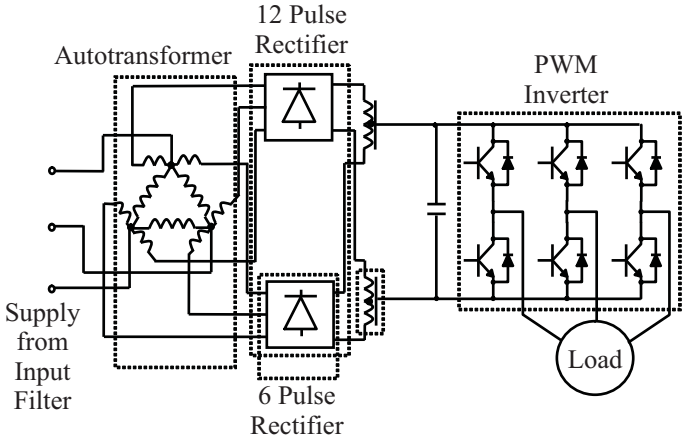

Figure 3.27: Twelve-pulse diode bridge rectifier with autotransformer, DC-link and PWM inverter

former allows a relatively low kVA rating of transformer, but inter-phase reactors must be included to ensure the independent operation of the two six pulse diode rec-

tifiers. Using a twelve pulse diode rectifier, harmonic specifications can be met with smaller input filter inductors and capacitors than is the case for a six pulse diode rectifier.

Another diode rectifier variant is the use of an eighteen pulse diode rectifier with a differential delta / fork autotransformer connection with three outputs, described in US patent "5,124,904" [44]. This topology has advantages in that inter-phase reactors are not required and the 5th/7th and 11th/13th harmonics are cancelled and can therefore comply with current aerospace power quality specifications without an input filter. The manufacturing complexity of the autotransformer, the significant power rating of the magnetic components (close to 60% of the power throughput), and its inherent impedance mismatch are considered as disadvantages [45].

A back-to-back topology with an active PWM-rectifier and PWM-inverter is shown in Figure 3.28, where the rectifier bridge is a duplicate of the inverter bridge [46]. This

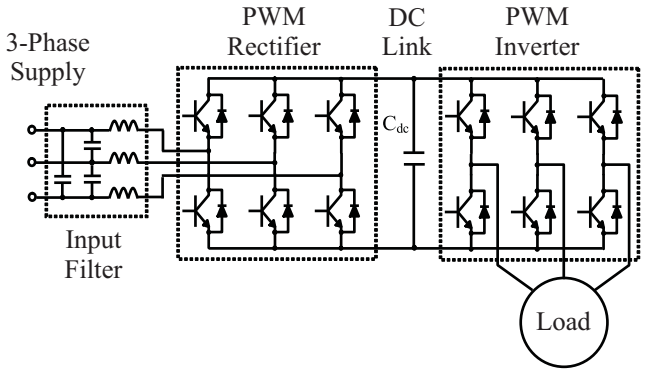

Figure 3.28: PWM-rectifier and PWM-inverter linked via a DC-capacitor

circuit allows regeneration during motor braking. This feature means that power can be controlled to flow back to the supply rather than being dissipated in a resistive breaking circuit, as is typically used in a drive with a diode rectifier. The inductors of the input filter see a large amplitude PWM voltage ripple and must therefore be fairly large to limit the current ripple. However, due to the high frequency PWM used, the input harmonics are of high frequency and the total filter size will be much

less than that for the six-pulse diode rectifier.

In rectifier-inverter drives for industrial applications the DC-side capacitance value is normally chosen to be quite high to keep DC voltage ripple low and to provide energy storage to reduce the effect of transient dips in the supply voltage. For aerospace applications however its value is chosen to be as small as possible, since film capacitors need to be used, to save space and weight. The minimum possible capacitance value that can be chosen is dictated predominantly by:

- The need to keep the voltage ripple within limits that will allow the inverter and its control to function adequately
- The need for the capacitor to be physically large enough to handle the ripple current requirement
- The bandwidth of the overall control strategy to limit charging of the DC link during regeneration

There is a potential to make substantial space and weight savings, when a matrix converter is used, due to the absence of a relatively bulky DC-link capacitor. The input filter inductors and capacitors are also small and light compared with the input filter or auto-transformer required for the rectifier-inverter configurations described previously. This is because the input filter only needs to remove high switching frequency harmonics[1] (typically at least 10 kHz).

It is possible with the matrix converter to return regenerative power to the supply which can result in further space and weight savings by omitting a resistive dump circuit. Although the output voltage is constrained to a theoretical maximum of 86%, this is not a problem if the load system at the output can be operated with a proportionally higher current to achieve the required power flow. In order to make a fair comparison between converter topologies it has been assumed that the lower

[1] Assuming the load has a constant power. This will be discussed further in Chapter 4

voltage transfer ratio of the Matrix Converter will result in a higher output current demand in order to achieve the same output power.

3.7.2 Prediction Method

Reliability can be defined as a probability of failure-free performance of a required function, within a specified environment, and over a given period of time. There is a difference between the way reliability is predicted and the way it is actually achieved. Industry tries to increase product reliability by separate activities such as design, involving previous engineering experience, development testing, manufacturing process control and product screening. Unfortunately, a link between these activities is not always made, and the degree to which the various activities are carried out successfully may not be represented accurately in reliability prediction methods [47]. Therefore, a discrepancy is generally expected between reliability prediction results and the 'real' reliability measured from products in service. Nevertheless, for proposed new systems, that only have limited in-service data or none at all, reliability prediction methods are important as they offer the only option to obtain quantitative reliability information. This reliability information can be considered valid for comparative purposes where the design and experience issues can be considered to be constant for all converter topologies.

The reliability prediction method chosen here is based on the military handbook for reliability prediction of electronic equipment MIL-HDBK-217F [42]. This method is still most widely used and accepted for military and civil aerospace applications, although it has been shown to be unrepresentative of real products [47]. One problem is that the handbook was last updated in 1995, and micro-electronics and power electronics technology have developed considerably since then. However the techniques are suitable for developing comparisons between circuits.

Reliability prediction has been carried out for the five different converter topologies discussed in the previous paragraph. The procedure for calculating the reliability of

a system starts with establishing its hierarchy of subsystems and components. For a rectifier-inverter drive, the following subsystems are defined: input filter, converter module, control and monitoring platform, power connectors, and DC link with clamp circuit. The converter subsystem is further subdivided into the switch modules, and the gate drives that control the semi-conductor switches. The controls and monitoring platform is subdivided into the FPGA (Field Programmable Gate Array) and DSP (Digital Signal Processor) boards. The DSP boards include algorithms to control motor speed and currents. The FPGA boards derive the exact switching instants of the power switches.

Assuming that the failure rates are relatively small, the total system failure rate is the sum of the failure rates of all subsystems. The failure rate of a subsystem is the sum of the failure rates of its components. Reliability handbooks provide failure rate data of components depending on parameters that have to be defined such as environment, temperature, quality and stress. The same environmental conditions (airborne, uninhabited, cargo), temperature of 25°C, and high quality components and connections have been assumed for all drive configurations.

Component data for the EDAAS 20kW matrix converter drive was used for the reliability calculations. The matrix converter data has been adjusted according to the different number of components that are present in the four rectifier-inverter topologies to predict their reliability. The difference in the main electrical power components used in these configurations is illustrated in Table 3.2, showing that the Matrix Converter has a larger number of active semiconductor devices.

Device	Inv' Rec' 6-pulse	Inv' Rec' 12-pulse	Inv' Rec' 18-pulse	Inv' Rec' PWM	Matrix Converter
Diode	12	18	24	12	18
IGBT	6	6	6	12	18
DC Capacitor	1	1	1	1	0
Large Inductor	3	0	0	1 (3-phase)	0
Transformer	0	1	1	0	0

Table 3.2: Main electrical components of the drive topologies

The general experience with electrolytic capacitors often used in traditional industrial drives is that they have a short life time and are quite unreliable. For this reason it was expected that a higher reliability can be achieved with a matrix converter due to the absence of a DC capacitor. However, a metal film capacitor was considered in this study for reliability prediction of the rectifier-inverter drives, since they would be likely to be used for aerospace applications due to their higher reliability and longer life time.

The matrix converter uses the highest number of semi-conductor devices, whereas the topology using the six-pulse diode rectifier has the least number of semi-conductors. It was expected that this fact would contribute to a decreased reliability of the matrix converter, but this appears to be only partly true as the voltage stress is important for the failure rate of the semi-conductor switches.

3.7.3 Voltage Stress Factor

A voltage stress factor is specified in the MIL-HDBK-217F for diodes which takes into account the voltage stress that the device is subjected to during its operational life time. This stress factor is derived from the voltage stress ratio $Vs = \frac{AppliedVoltage}{RatedVoltage}$

The voltage stress ratio maps to an electrical stress factor π_s according to tables laid out by the specified in the MIL-HDBK-217F. This stress factor is one of the factors (others involve environment, temperature and quality) used to derive the part failure rate λ_p by multiplication with the base failure rate λ_b.

Simulations have been carried out to determine the applied voltage on the switching devices. Table 3.3 shows the calculated rms and average values of the voltages across the diodes of a six-pulse rectifier and anti-parallel diode/IGBT pairs of respectively an inverter and a matrix converter.

The voltage applied on the diodes in the twelve-pulse and eighteen-pulse rectifier configurations are the same as in the six-pulse rectifier, since they comprise six-

Voltage	Diode Rectifier Rectifier	Inverter Diode/IGBT	Matrix Converter Diode/IGBT
Average [V]	135	135	67.5
RMS [V]	190	190	89.3

Table 3.3: Voltages across the semiconductor devices in the different converter topologies

pulse rectifiers connected in parallel on the DC-side. The voltage applied to the diode/IGBT pairs in the matrix converter are half, or less than half when considering rms, than that of the voltages across the switches of the rectifier diodes and inverter diode/IGBT pairs. This is due to the fact that there are two anti-parallel diode/IGBT pairs connected in series in a bi-directional switch, each of which take their share of blocking the voltage for half of the time in a cycle.

One drawback of using MIL-HDBK-217F guidelines is that it does not include an IGBT device, since its commercial use only grew significantly after MIL-HDBK-217F was produced. The failure rate of a MOSFET type low frequency transistor given in paragraph 6.4 of MIL-HDBK-217F is used, because it is considered most applicable with respect to power rating. Although a voltage stress factor is provided for a diode, this is not the case for a MOSFET. This has been taken into account by an adjustment factor of 0.5 applied to the failure rate of the IGBTs.

3.7.4 Reliability Results

The reliability prediction results for the different converter topologies are summarized in Table 3.4. The MTBF (Mean Time Between Failure: inverse of failure rate) numbers of the different topologies are very similar in terms of reliability evaluation. The predicted reliability for the six-pulse diode rectifier with PWM-inverter appears to be somewhat higher than for the other topologies, followed by the matrix converter having virtually the same reliability as the twelve-pulse rectifier with inverter. The eighteen-pulse rectifier/inverter and PWM-rectifier/inverter topologies are both slightly less reliable.

Topology	Failure rate [1/hours]	Mean Time Between Failure (MTBF) [hours]
Rectifier(6pulse)-Inverter	26.60e-6	37,592
Rectifier(12pulse)-Inverter	29.02e-6	34,464
Rectifier(18pulse)-Inverter	30.72e-6	32,550
Rectifier(PWM)-Inverter	31.09e-6	32,166
Matrix Converter	28.66e-6	34,894

Table 3.4: Results of the reliability analysis

The failure rate of the converter module in the case of the six-pulse rectifier drive is lowest due to the lowest number of diodes used. The failure rate of the converter module of the PWM-rectifier/inverter scheme is higher than that of the matrix converter, because although the total number of semi-conductor switches is less, they are subjected to a higher voltage stress.

The failure rate of the gate drives block is highest for the matrix converter and lowest for the diode rectifier/inverter schemes, which relates directly to the number of gate drives needed for the IGBTs. The failure rate of the internal controls and monitoring of the diode rectifier schemes are somewhat lower than the PWM-rectifier/inverter and matrix converter schemes, due to their simpler control requirements. The DC-link/Clamp subsystems of the diode rectifier schemes have a slightly higher failure rate than in the case of the PWM-rectifier due to: (i) the soft-start (pre-charge) circuit required to prevent large inrush currents and (ii) the dump resistor with a control switch to dissipate energy locally when power flows back from the load side.

The reliability of the different configurations appears to be very similar. It was found that the voltage stress on the semi-conductor components is a significant factor. The voltage stress is lower in the case of the matrix converter, which reduces the failure rate of the converter module, but the larger number of semi-conductors and gate drives increases the failure rate. The MIL-HDBK-217F guidelines are used for the reliability prediction, which is still most widely accepted in the aerospace and military industry, although it is generally viewed as pessimistic. Specific shortcomings of MIL-HDBK-217F identified here are that IGBT devices are not included and current stress is not considered.

3.8 Summary

In this chapter, the matrix converter circuit and principle of operation has been introduced. The potential advantages of the matrix converter solution are summarised below.

- **No DC Link:** Since the matrix converter is a direct AC-AC converter there is no need for large energy storage components.
  - **High Power Density:** As the need for bulky electrolytic capacitors is removed there is potential for greatly increased power densities.
  - **High Operating Temperature:** For VSI circuits the operating temperature is usually limited by the electrolytic capacitors. Since these are not used in Matrix Converters there is a potential for increased operating temperatures.
- **Bi-directional Power Flow:** The Matrix Converter is inherently bi-directional so can regenerate energy back to the supply.
- **No Low Frequency Harmonics:** Both input and output currents are near sinusoidal and free from any low frequency harmonic distortion.
- **Controllable Displacement Factor:** Depending on the modulation method used, the input displacement factor can be controlled irrespective of the type of load.

Two of the main factors that have held back widespread commercial exploitation of the matrix converter are:

- **Output Voltage Limit:** The ratio of the input to output voltage amplitude is limited to 87%.
- **High Device Count:** The number of active devices needed to construct a Matrix Converter is higher than for alternative converter topologies

For most industrial applications the physical size of the drive is not of significant importance. Therefore the possibilities of higher power densities and increased operating temperatures are not seen as an advantage for these applications. The Matrix Converter has a 87% voltage transfer ratio limit which prevents the use of standard motors with standard supplies. For these reasons the Matrix Converter is not expected to replace the VSI for standard industrial drive applications. However, there are areas where Matrix Converters could provide a realistic alternative offering significant improvements in performance such as integrated drives, where the power electronics and machine are packaged together. These are difficult to fabricate at higher power levels using conventional technology due to the size of the DC link capacitor. Not only is it bulky, but the temperature limitations are a more serious problem than usual when the power circuit is integrated with the machine. The matrix converter is a very strong contender in such applications, particularly as the non-standard machine means that the voltage transfer ratio limitation is irrelevant. Apart from integrated drives, other applications requiring high temperature operation (for example electric vehicles, where the power electronics are cooled by the engine oil, and aircraft applications) are ideally suited to the matrix converter.

The matrix converter could be an ideal converter topology to exploit future technologies such as high temperature silicon carbide devices. These devices will operate at temperatures up to 300°C so the lack of large electrolytic capacitors, as normally used in an inverter, would again be a significant advantage.

It is important to note however that the size advantage can only be achieved if the input filter is sufficiently small. This is a complex, application specific issue but is basically dependent on obtaining a sufficiently high switching frequency.

The four step commutation technique is considered to be superior in terms of reliability, due to commutation information failure, when compared to all two or one step commutation strategies. This is because in a two step commutation technique, the current or voltage direction information is necessary for the commutation event and also for the conduction of current, whereas, for the period of conduction in the four

step technique, this information is not necessary since conduction is guaranteed by gating all of the necessary devices to conduct in both directions. The direction information is only necessary for a commutation event in the four step strategy. Here, the current direction based, four step technique has the further advantage because it is easier to handle commutation failures than in a voltage direction based strategy. This is because the failure to commutate properly in a current direction based strategy results in an open circuit of the load and not a short circuit of the input as in voltage based techniques (see section 5.1.4). Current or Voltage direction circuit failure would result in commutation failures for the four step techniques but also conduction failure for the two step strategies. It is for this reason that the four step current commutation technique was used in the final prototype matrix converter implementation.

The section on the reliability study has shown that the matrix converter is not inherently any less reliable than standard VSI based converters for the aerospace application considered even though the handbook used for the analysis is in need of updating.

Chapter 4

Drive System Simulation

Many comparative studies have been carried out [48] to find the most appropriate motor for aerospace applications. Issues such as reliability, fault tolerance, size and weight have been considered without paying much attention to the topology of the power converter. The choice of motor for this study is the result of a detailed examination and comparison of different drive systems which have been configured on the basis of the application, the desired control strategy and the type of converter to be implemented. Earlier in this study, the major advantages of using a matrix converter for an aerospace application, in particular the absence of bulky and unreliable electrolytic capacitors, in this topology of converter has been mentioned. The use of a matrix converter means that, unless heavy filtered, power fluctuations in the load are directly fed to the input supply with consequent distortion of the line currents. A series of simulations of different drive systems have been run to understand the impact of the choice of the motor among the available sinusoidal and non-sinusoidal machines for the proposed 30kW matrix converter driven rudder actuator system. The different motor types that will be analysed are as follows:

- Switched Reluctance Machine
- Trapezoidal Permanent Magnet AC Machine

- Induction Machine
- Sinusoidal Permanent Magnet AC Machine

The SABER software package has been used to carry out the simulations. This numerical engine is a powerful tool which allows simulation of mixed-technology systems and the analysis of their effects under different operating conditions. Each simulated system is the result of a set of components or subsystems which can be found in libraries of standard components or user-defined templates. The user-defined templates are achieved using programs written in the MAST modelling language. A symbol is generated and associated with each template. The components are interconnected using a network list (netlist) which converts the simulated model in to an ASCII file containing the connection points and values for the model parameters. The simulated system, represented by all of its components which can be, linear, non linear, continuous, time discrete, digital or analogue, mechanical, electrical, hydraulic, generates a system of equations which, depending on the model complexity, can be large. SABER is capable of solving the system of equations given chosen analysis methods to both verify the functionality of the design in the time or frequency domain and to fine tune the design parameters. Such is the effectiveness of SABER that many subtle effects and components normally excluded from other simulation methods can be included.

Before any of the drive systems could be simulated, the matrix converter needed to be modelled. The following parts needed to be implemented

- Input filter
- Matrix of bidirectional switches
- Over voltage clamp circuit
- PWM generator
- Modulation strategies
- Commutation strategies

The electronics have been modelled using electrical components (i.e. switches, diodes, capacitors, resistors, inductors, power supplies and comparators) from the SABER standard library, selecting for each of them the desired parameter values.

The next stage was to create the necessary switching signals which would generate a safe commutation of the bidirectional switches. Using MAST, events can be scheduled at particular points in time so that logic signals can be generated to mimic the digital logic functionality of a Field Programmable Gate Array (FPGA)(which would be used for logic implementation in a real controller) with the correct time resolution of a real system. This function was used to re-create a current direction based commutation technique (four-step current commutation, see Section 3.6.1). A voltage based commutation technique (Metzi commutation, see Section 3.6.2) was also implemented. The two techniques were tested with the SABER simulator by simulating the logic signals coming from a modulator using two ideal clock units with different duty cycles. The results were compared and were both found to work well according to the literature. Since the protection of a matrix converter is more robust when using a current direction based commutation technique (Section 5.1.4), this method was used in all of the motor drive simulations.

The modulator has been successively designed, again using MAST, and different modulation techniques have all been implemented and compared using simple models of test circuits such as a three input phase to single output phase matrix converter. The modulation techniques implemented are as follows:

- Venturini basic algorithm (Section 3.2.1)
- Optimum Amplitude Venturini Algorithm (Section 3.2.2)
- Space Vector Modulation methods (Section 3.2.4)

Again, events were scheduled using MAST to generate the same type of PWM resolution that would be used in a real system. A simulation of the matrix converter driving a permanent magnet synchronous machine (Section 4.2.1) was run using dif-

ferent modulation techniques. Figure 4.1 shows the Iq, torque producing, currents produced by the two modulation techniques during speed transients. These results show that there is a different harmonic content in the output waveform for each modulation technique.

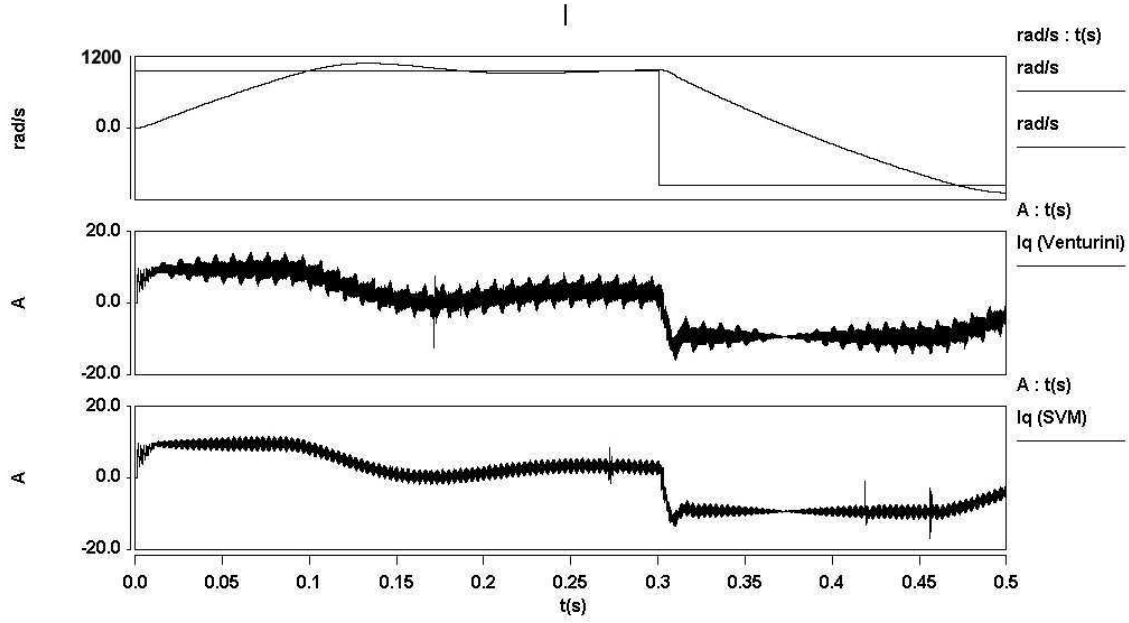

Figure 4.1: Comparison of Space vector modulation and Venturini modulation

4.1 Non-Sinusoidal Machines

The Switched Reluctance and Trapezoidal Permanent Magnet AC machines are characterised by switched, non sinusoidal input voltages and draw non-sinusoidal currents. Therefore we will refer to these machine as the "non-sinusoidal" machines. They are among the most favoured machines for aerospace applications, for different reasons, but for both of them it is possible to say that they introduce a higher degree of reliability compared to any other machine because they have a simple design.

4.1.1 Switched Reluctance Machine

The switched reluctance machine (SRM) is a variable-reluctance machine usually driven by a switching inverter [49]. It is characterised by excitation windings on the stator and a salient rotor made of magnetic material. Figure 4.2 shows a diagram of a cross section of an SRM showing the stator windings and salient rotor.

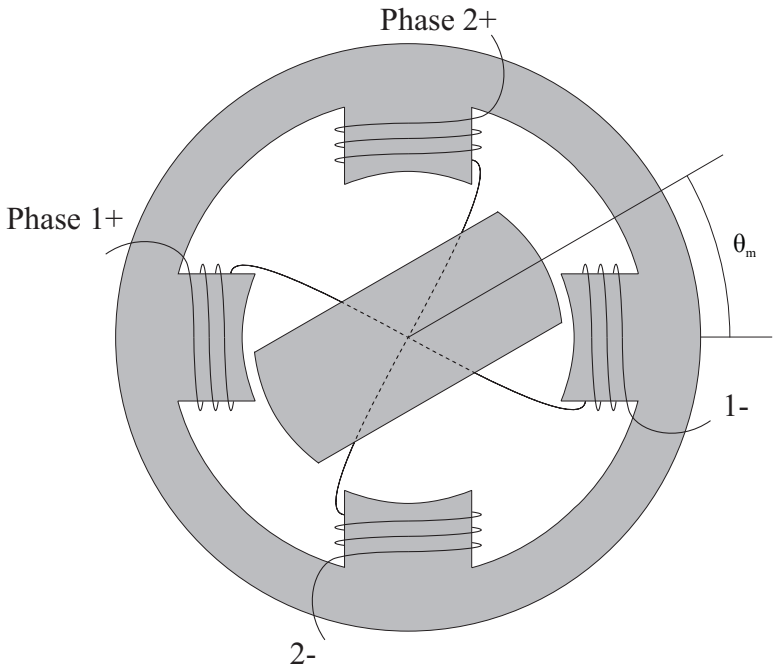

Figure 4.2: Cutaway view of a two phase, doubly salient switched reluctance machine

By energising a stator phase winding the rotor will rotate towards the position which will maximise the stator flux linkage produced by the applied current in the stator winding. Due to the saliency characteristics of this machine the stator inductances are a function of the angle θ_m between the rotor axis and the magnetic axis of the excited phase winding. The inductances will be maximum in correspondence of minimum reluctance because they are inversely proportional to each other. Considering that the stator flux linkage λ is related to the inductance by the following expression $\lambda = L \cdot i$, it suggests that, by sequentially exciting the phases of a Variable Reluctance Machine

(VRM), the rotor will rotate to minimise the reluctance. The electromagnetic torque produced by the interaction of the flux generated in the stator windings and the rotor is a function of the square of each individual phase current, the derivative of the self inductances of each phase and mutual inductances with respect to the angle θ_m.

The most commonly used SRM has saliency in both the rotor and the stator because a larger torque for a given frame size can be produced. This is the configuration which will be referred to for the SRM drive simulation. In the double salient SRM the derivative of mutual inductances with respect to the angle θ_m are zero and this simplifies the expression of the torque which, assuming a two-phase doubly-salient SRM, is given as follows:

$$T = \frac{1}{2}\, {i_1}^2\, \frac{dL_{11}(\theta_m)}{d\theta_m} + \frac{1}{2}\, {i_2}^2\, \frac{dL_{22}(\theta_m)}{d\theta_m} \tag{4.1}$$

From (4.1) it is clear that the torque will depend only on the magnitude of the currents and not on their polarity leading to another interesting aspect of these machines, the electronics required to supply power. Only unidirectional solid-state switches are needed in power converters which drive SRMs and the implication of this will be discussed further in this section.

It can be seen that there are angles where zero torque would be produced, either when the rotor is aligned with the stator pole or perpendicular to it (where $\frac{dL}{d\theta_m} = 0$). In general this can occur when the ratio of stator poles to rotor poles (or inversely if the number of rotor poles is greater) is an integer number. A motor with six stator poles and four rotor poles is the first combination where positive or negative torque can be produced at any angle.

The simple layout of rotor and stator in the SRM make them easily manufacturable and because the absence of permanent magnet material in the rotor allows a higher range of operating temperatures. This leads to a smaller motor for a given rating and frame size. Another advantageous point in favour of the SRM is that it can still operate when one of the windings fails (or if the converter fails to drive one of the windings). This is important with regards to issue of reliability.

To be able to further analyse the SRM when driven by a matrix converter a simulation, in SABER, of the drive system has been carried out and its schematic is represented in a block diagram in Figure 4.3

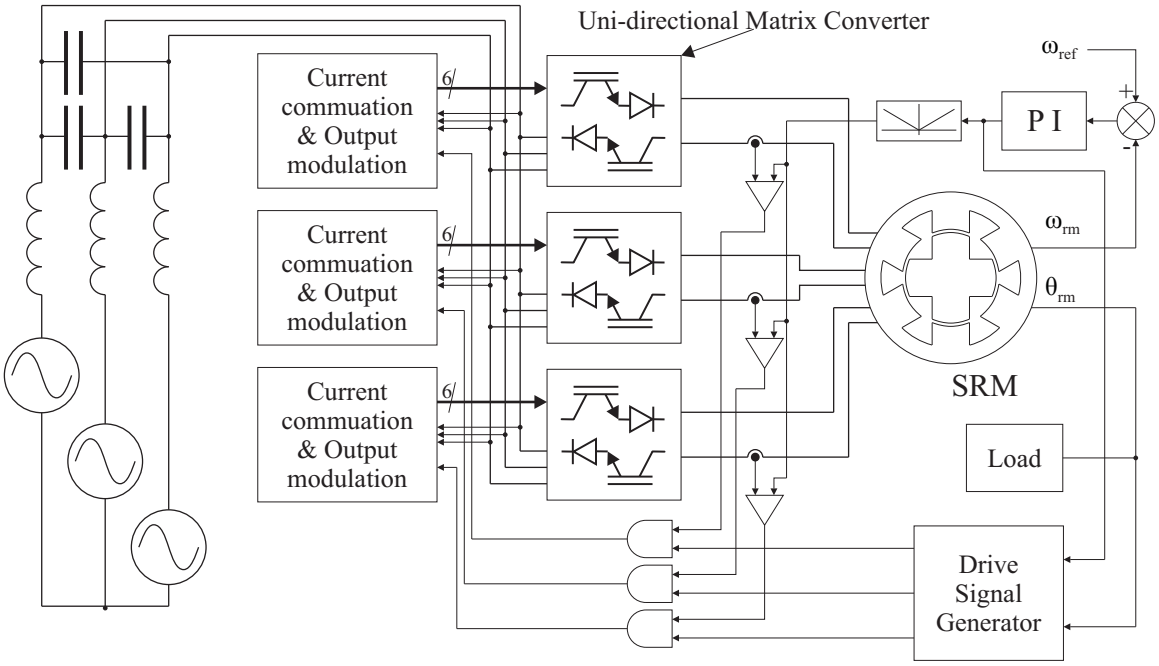

Figure 4.3: Switched Reluctance Drive System Block Diagram

The schematic includes a model of a 60kW, six stator pole and four rotor poles, 6/4 SRM, which is a template in MAST originally outlined in [50] and together with the load represented by two SABER standard components (an inertia and friction block) it completes the mechanical part of the simulated model. The electrical part of the schematic is given by the balanced three phase sinusoidal voltage source, the standard aerospace 230V phase to neutral and 400Hz, the input L-C filter and the matrix converter. Considering the topology of the SRM machine and the dependence of the torque from the magnitude of the phase currents, this required a different matrix converter configuration from the one described in Chapter 3. The matrix converter adapted for this type of motor is shown in Figure 4.4 and it is characterised by unidirectional switches with series diodes. The same number of switching devices are

needed to drive a 6/4 SRM with a conventional three phase to three phase bidirectional matrix converter. The control of the switching of the devices is implemented on

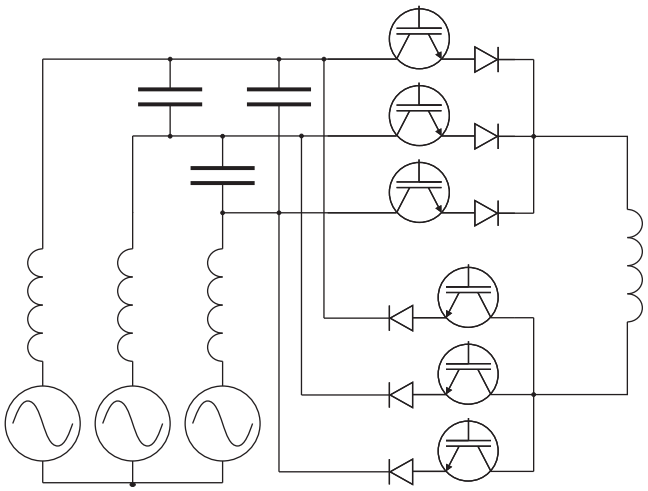

Figure 4.4: Unidirectional Matrix Converter to drive a single phase of the SRM

the basis of the information on the position of the rotor and on the hysteresis control applied to the winding currents. The stator phases will be energised and de-energised only between specific angles and, since torque is proportional to i^2, negative torque is produced by changing the excitation angles. The excitation is done in such a way that a positive voltage will be applied to a phase if the current in that phase is lower than the limit demanded and a negative voltage will be applied to reduce the current. The reference current is generated by a speed controller.

Given the set of three phase sinusoidal voltages and the logic signal which represents the feedback from the motor control, two strategies of modulation and consequent generation of the switching signal sequences have been implemented in two different simulated models and results from them have been compared.

In the first case, the most simplistic approach was to apply, when necessary, the most positive or most negative available voltage to the motor windings to increase or decrease the phase currents. Therefore a MAST template which could implement this commutation strategy was developed. In the second case the Venturini basic

algorithm implemented as described in Section 3.2.1 was used to generate the switch modulation duty cycles which were then employed to produce the appropriate commutation sequences to apply either a positive or a negative voltage to each of the six output phases of the converter. The two simulations with different voltage modulation approaches were run in SABER to test the control of the machine in the four operating quadrants, to analyse the behaviour of the motor currents and torque during acceleration and especially to investigate the effect of the torque pulsation on the input line currents.

There are angles, when using a 6/4 SRM, that can produce torque when two stator phases are energised. This is at the end of the outgoing phase's conduction period and the beginning of the incoming phase's conduction period. This would result in twice the phase current flowing in the machine for a short period and may further increase the pulsation of power through the converter. It is also possible to not energise the phases for all of the possible time and have no current flow for some periods. This would also provide power pulsations through the converter. It is for this reason that the sequence of energising and de-energising angles has been configured to avoid overlap and dead-time between them to be able to attempt to achieve a more constant power flow.

Figures 4.5 and 4.6 show the motor phase currents and torque generated during the acceleration and deceleration of the SRM using the two different modulation techniques, the former using the simple modulation method and the latter using the Venturini algorithm. Clearly the current control response when using the simple modulation method is superior to the Venturini method. This is because the output voltage of the Venturini modulator is limited to 50% of the input voltage and hence the rate of change of the motor phase current will be lower. Pulsations in the motor torque can be clearly seen in both simulations. These will cause power pulsations in the motor and hence current distortion at the input to the matrix converter.

Figure 4.7 shows the supply current and voltage waveforms during the period of acceleration of the SRM. The input current waveforms are clearly distorted by the

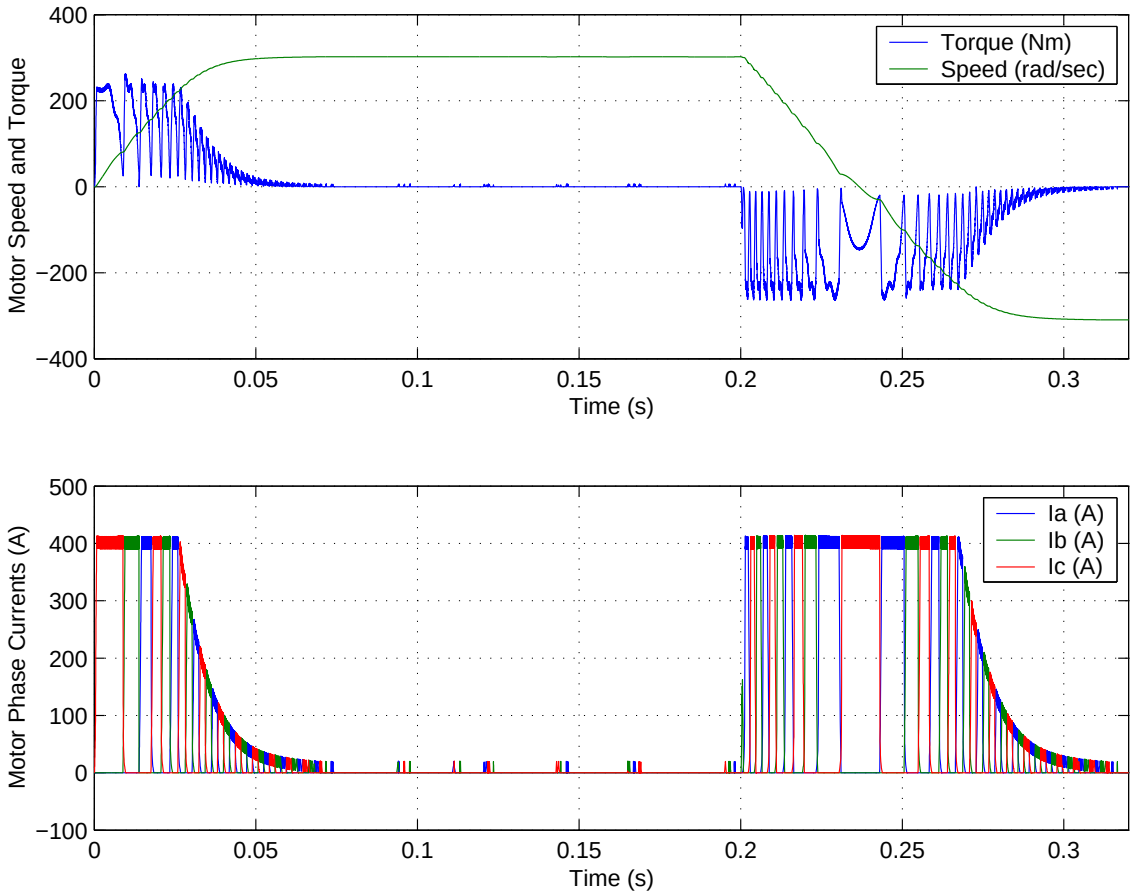

Figure 4.5: SRM performance when using the simple modulation method

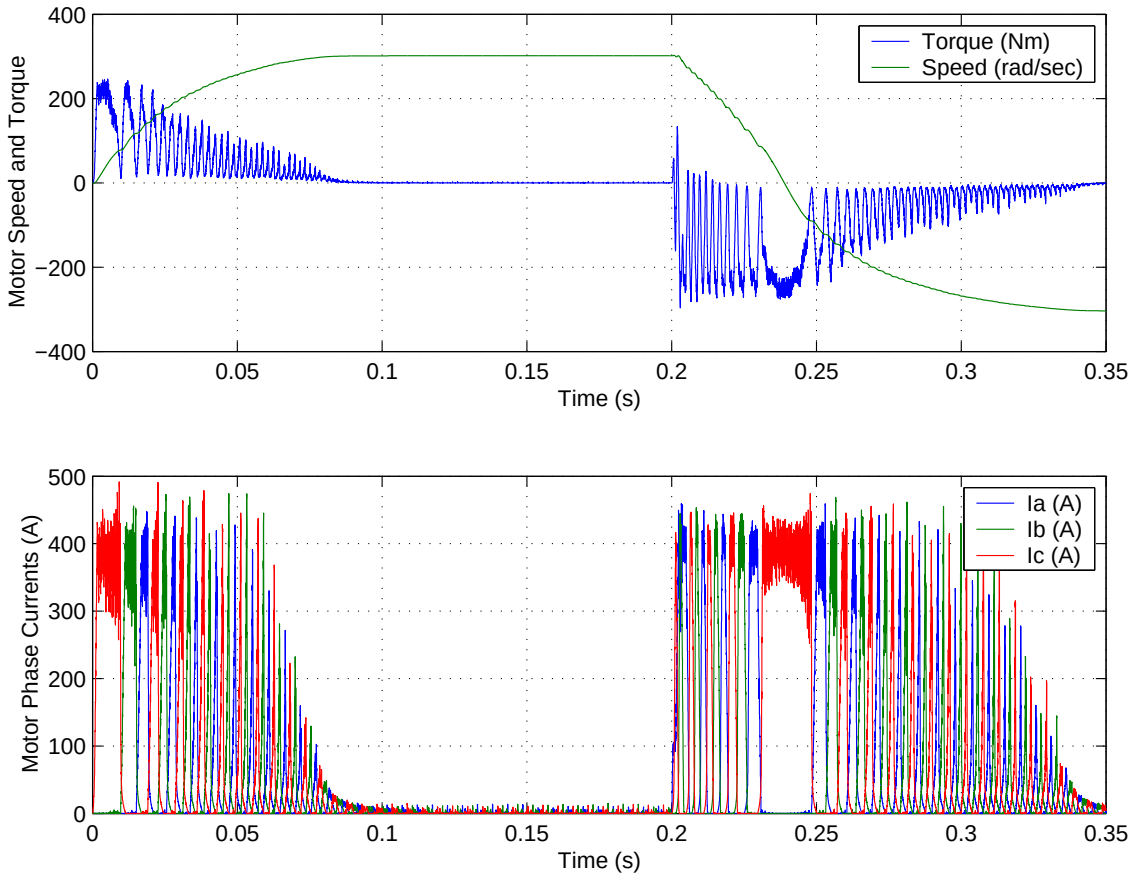

Figure 4.6: SRM performance when using the Venturini modulation method

power pulsations of the drive system. No improvement can be seen when using the Venturini modulation algorithm. This type of current waveform will be unacceptable for most applications and large filter components would have to be employed to make them acceptable.

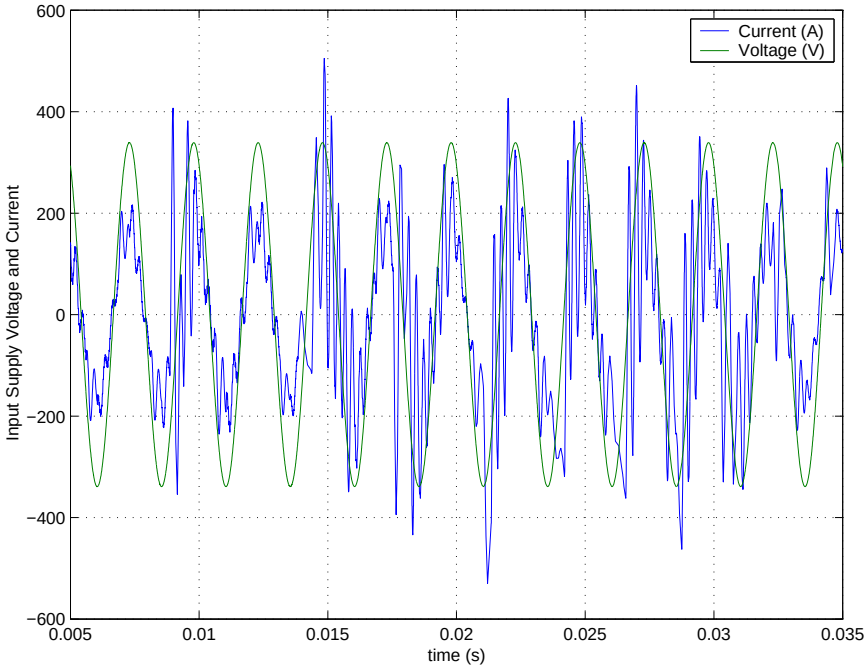

(a) Simple modulation method

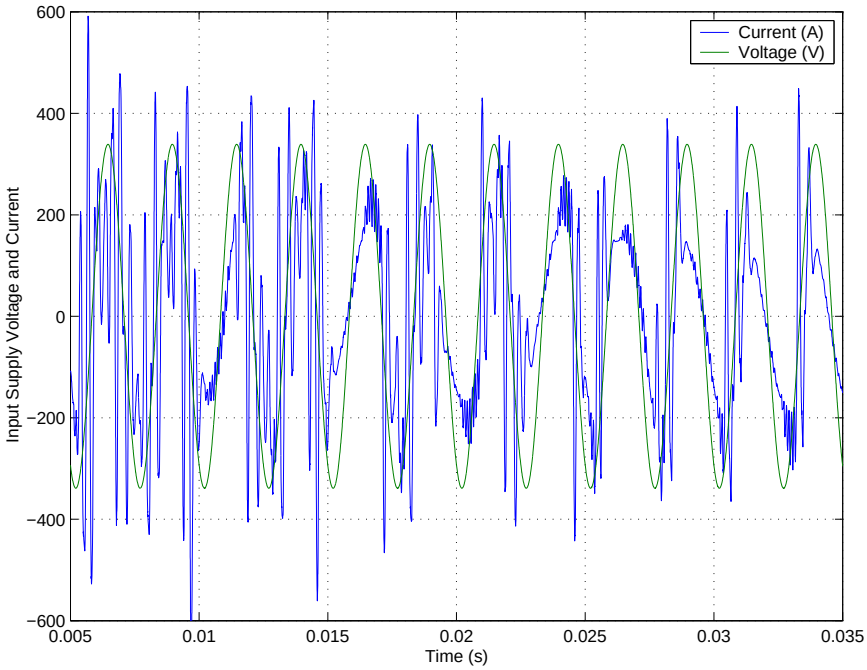

(b) Venturini modulation method

Figure 4.7: SRM Drive system supply voltage and current waveforms

4.1.2 Trapezoidal Permanent Magnet AC Machines

Another non-sinusoidal machine, the trapezoidal permanent magnet AC machine (PMAC) has been investigated in simulation when using a matrix converter to drive it. The reason that this machine has been considered for this application is linked to its characteristics which make it very appealing for aerospace applications and there are some examples in the literature [51][52][53]

Looking at the main features of synchronous machines [54] in which alternating currents in the stator windings produce a rotating magnetic flux and DC currents in the rotor windings produce a flux wave which is stationery with respect to the rotor, it is possible to recognise the permanent magnet AC machine as a particular case of the former machines. In the permanent magnet AC machine, the rotor is a permanent magnet which will produce a constant flux. As for all synchronous machines including PMAC machines, a constant torque is produced when the rotor rotates in synchronism with the stator flux wave. This condition is verified when there is a constant angular displacement between the rotor and the stator flux waves resulting in a torque which is proportional to the sine of the displacement angle.

In PMAC machines, according to the way the stator windings are distributed on the stator and the way the magnets are arranged on the rotor, it is possible to have either a trapezoidal or sinusoidal distribution of the stator flux. The first case, which will be analysed in this section, trapezoidal PM machines are characterised by surface magnets on the rotor and concentrated stator windings which result in a trapezoidal back-EMF voltage waveform being induced in each stator phase during rotation.

If the stator windings are excited with rectangular current waveforms switching the gates of the IGBTs so that two of the phases of the trapezoidal PM machine are energised at a time, a nearly constant output torque will be developed. Looking within an electrical cycle, every sixty degrees, one of the phases will be excited with either a positive or negative current and for a third of a cycle there will be no current through the windings. This is shown in Figure 4.8 which represents the ideal current

excitation waveforms applied to each phase winding in an electrical cycle. This results

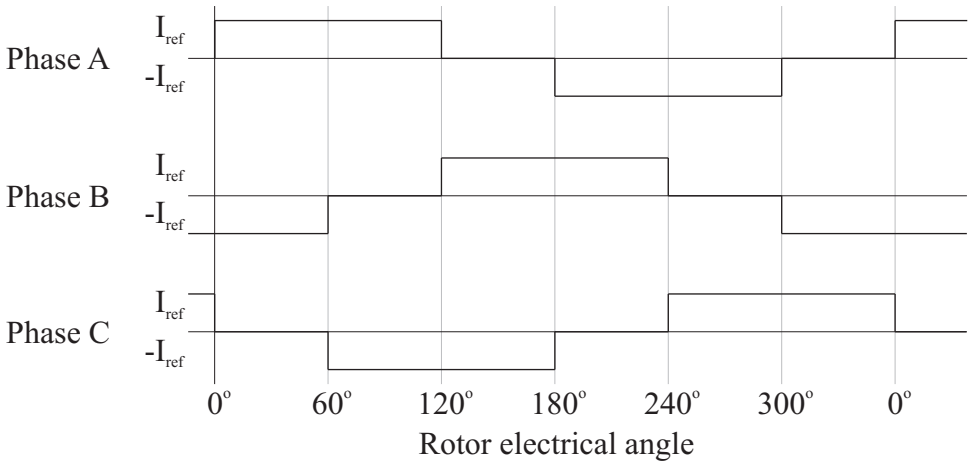

Figure 4.8: Ideal current excitation waveforms applied to each phase winding of a trapezoidal PM machine in an electrical cycle

in the load energy fluctuating six times during the electrical cycle every time a phase commutation event occurs.

It can be noticed that the direct proportionality of the back-EMF to speed and of the torque to the fixed current amplitude flowing in the stator windings is the same as that in a conventional DC machine with constant field excitation. It is for this reason that one of the common names given to a trapezoidal PMAC machine is permanent magnet brushless DC machine where the job of the commutator is done electrically by the power converter.

Even though it is possible to obtain a higher power density motor drive using trapezoidal machines because of higher torque production than in sinusoidal PM machines [55], the torque ripple due to the motor parasitic effects and phase current commutations is reflected in the input power quality and thus the converter line current. This has been investigated by running a simulation in SABER of a model of a PM brushless DC machine driven by a matrix converter, shown in Figure 4.9.

The speed controller generates a current demand which is processed by the Current

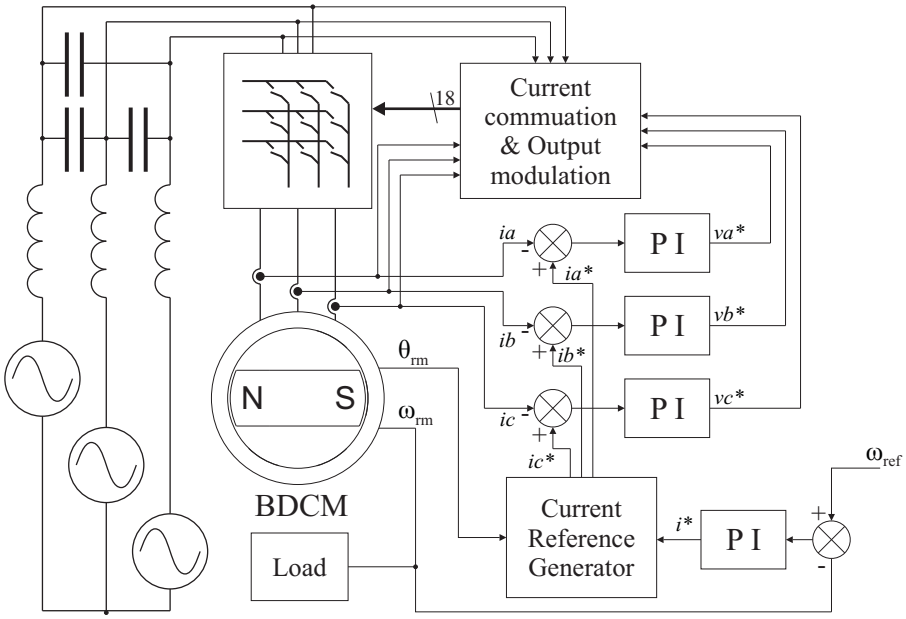

Figure 4.9: Block diagram of the simulated trapezoidal PM drive system

Reference Generator. This provides a current demand for each of the motor phase current PI controllers based on the motor angle as previously described in Figure 4.8. The current controllers generate voltage demands which are then processed to produce the switching signals that drive the matrix converter bidirectional switches.

Two different input supply frequencies, 400Hz and 800Hz, have been employed to analyse the effects of the interaction of the drive with the input at the selected filter resonant frequency of 4kHz on the line side current distortion. The reason for this is to investigate the possibility of using the input filter to help remove the current ripples associated with the motor input power pulsations. Figure 4.10 shows the supply voltage and current during acceleration of the brushless DC machine. Figures 4.10a and b are shown using an input supply frequency of 400Hz and 800Hz respectively. It can be clearly seen that the input current waveforms are unacceptable for most applications.

Waveforms for the current and voltage to be supplied to a 30kW brushless DC machine which was being designed by other members of the project were entered into the

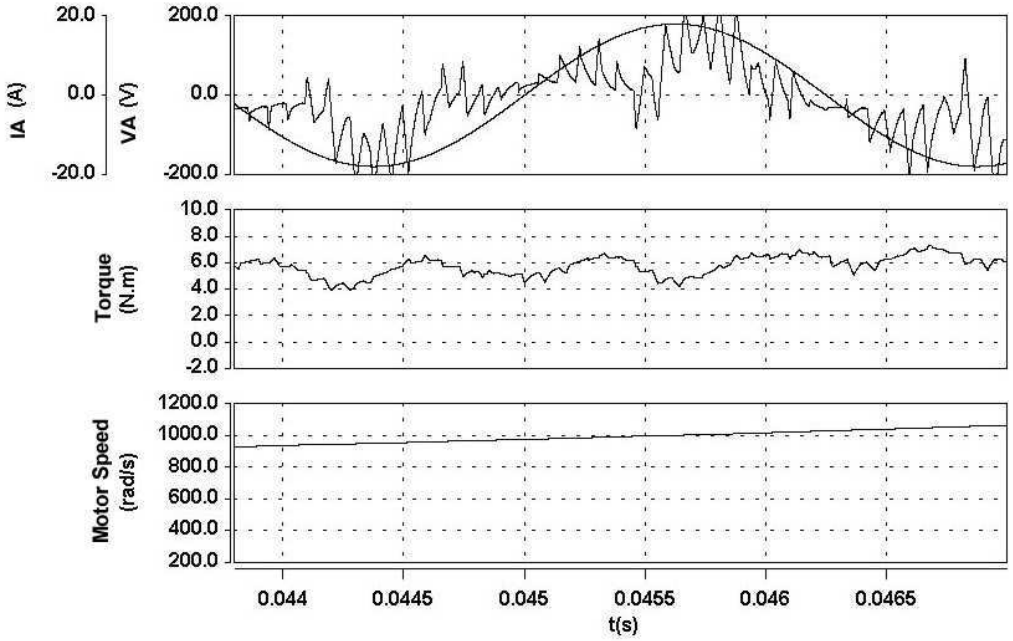

(a) Results using a 400Hz input supply

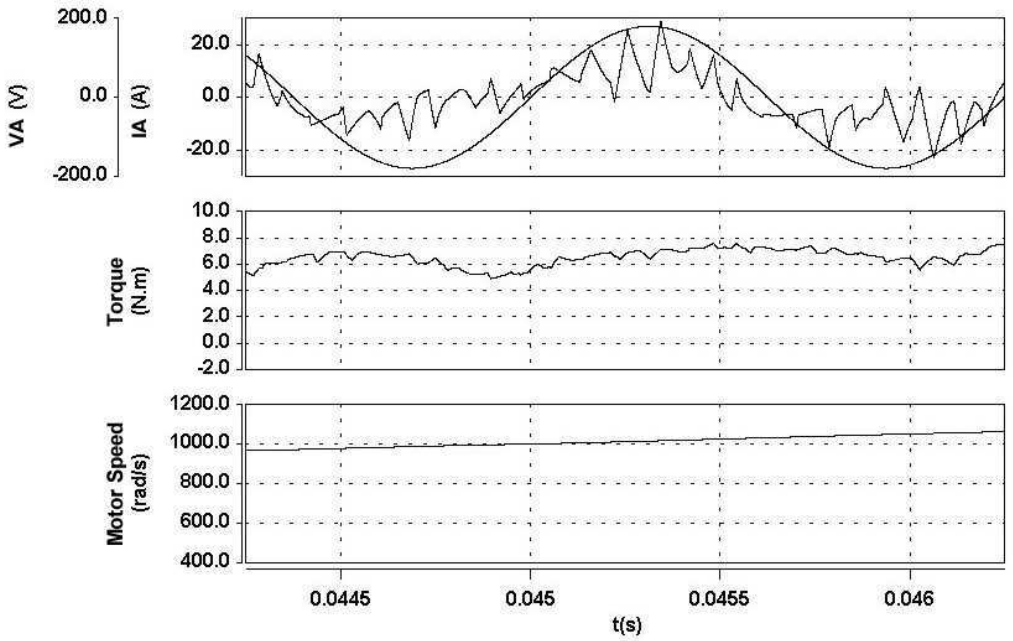

(b) Results using a 800Hz input supply

Figure 4.10: Waveforms from the simulated drive system with different input supply frequencies

simulation to determine the suitability of the converter-machine combination with regards to the input current quality. Figures 4.11a and b show the input current waveforms with supply frequencies of 400Hz and 800Hz respectively. The power pulsations in this case were well below the reasonant frequency of the input filter. Figure 4.12 shows the input supply current when the power pulsations are close to the 4kHz resonant frequency of the filter. In each of the figures, only one input current waveform is shown since the other two are similar.

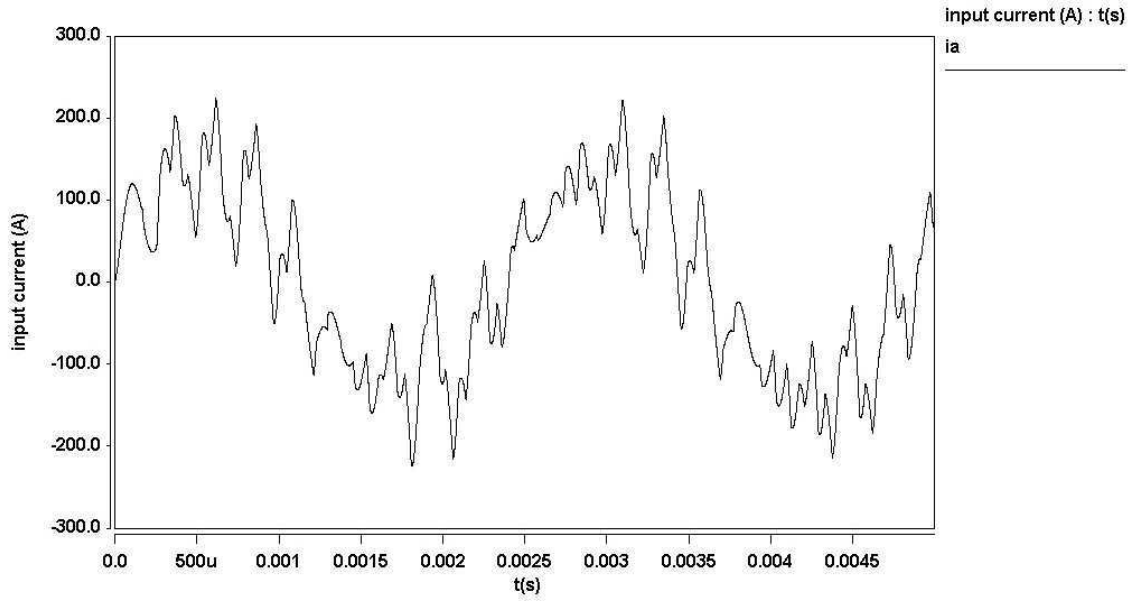

(a) Results using a 400Hz input supply

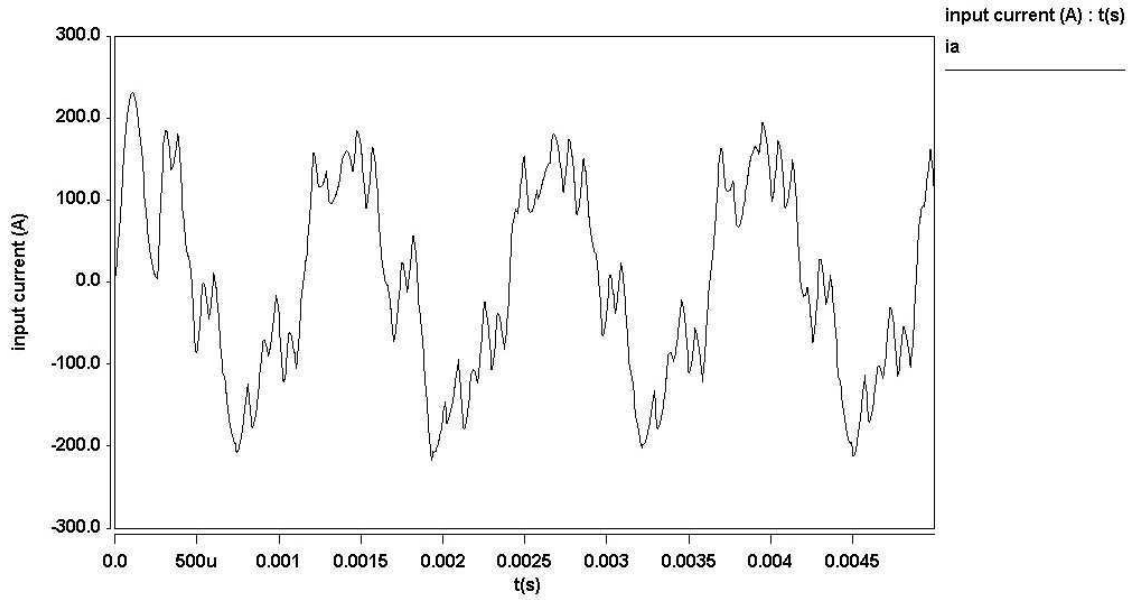

(b) Results using a 800Hz input supply

Figure 4.11: One phase of the input current for 400Hz and 800Hz supplies

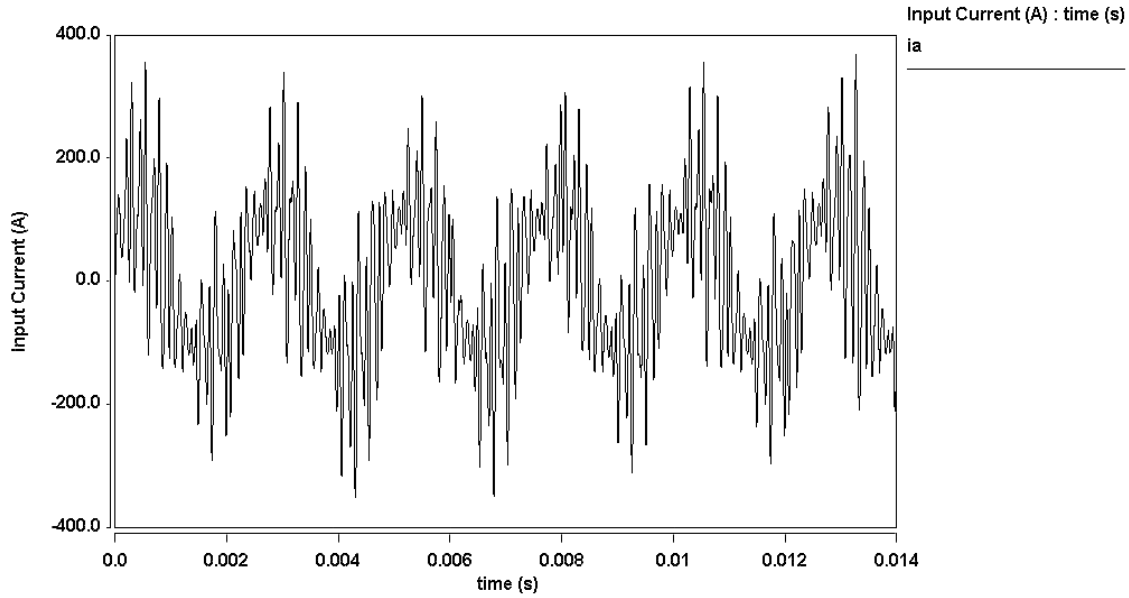

Figure 4.12: One phase of the input current when power pulsations are near to the filter corner frequency

4.2 Sinusoidal Machine Drive Systems

This section will highlight the features of the 'sinusoidal machines' such as the sinusoidal permanent magnet AC and induction motors which draw sinusoidal currents when supplied by sinusoidal voltages. In this case when the supply is a three phase balanced system the real power and the reactive power are constant and are not pulsating as in the case of the non-sinusoidal machines described in the previous section. The input filter of the matrix converter is therefore now mainly responsible for filtering the line current distortion due to the matrix converter (i.e. switching harmonics) and not distortion due to large power pulsations in the motor.

4.2.1 Permanent Magnet Synchronous Machine

To help to generate a sinusoidal back-EMF in sinusoidal PMAC machines, the stator windings are distributed sinusoidally over multiple slots while the rotor is generally characterised by having buried magnets and salient poles. The back-EMF results in being proportional not only to the speed but also to the magnetic flux linkage amplitude. For the instantaneous torque there is the expression (4.2) given in terms of the d-q phasor representation assuming that the d-axis is always aligned with the rotor flux vector.

$$T = \frac{3p}{2}[\Psi_f i_q + i_d iq(L_d - L_q)] \tag{4.2}$$

Equation 4.2 shows the dependence of the torque on two components, on the left the "magnetic" torque is directly proportional to the torque producing current iq and on the right the "reluctance" torque, which depends on the product of the i_q and i_d currents and on the difference $(L_d - L_q)$ due to saliency in the rotor. This means that the PMSM can operate as a Synchronous Reluctance motor if the rotor magnets are demagnetised which introduces a good degree of fault tolerance. The PMSMs have a superior speed range to PM brushless DC machines because of their increased controllability in the field-weakening region.

The major advantage when a PMSM is driven by a matrix converter is the possibility of exciting the stator windings with sinusoidal currents and voltages which eliminates the abrupt phase to phase commutations which occur in the trapezoidal PMAC machine and hence supply the machine with constant power. This will be shown in the following subsection with results from a simulation of a $1.5kW$ matrix converter permanent magnet motor drive for an Electro-Hydrostatic Aircraft actuator (EHA) which has been built and demonstrated for the Totally Integrated More Electric Systems (TIMES)[56] initiative. The experimental results from this project have been used to validate the simulation results and confirm the structure and methodology of the simulated model which can be employed to carry out detailed analysis of the whole drive system including unexpected practical issues.

4.2.1.1 TIMES Drive System

The system has been simulated in SABER and includes many of the non linearities found in a DSP based matrix converter drive. A simplified diagram of the simulated model is shown in Figure 4.13. The matrix converter circuit was implemented using switches and diodes to form a matrix of bi-directional switches gated according to the four-step commutation strategy based on the output current direction. Simulating the matrix converter circuit in this way allows the effect of different characteristics such as devices forward voltage drops and commutation times, which add to the circuit non-linearities, to be examined in more detail. The times used for the four-step current commutation can be changed to accurately represent a real drive system, gate drive delays can also be included. This is normally implemented in an FPGA or programmable logic in a real system and has been achieved in simulation by using programmes written in MAST. Figure 4.13 shows the speed and current control loops required from the vector control applied to the machine.

To represent the sampling action of a DSP based PWM interrupt driven system, the motor control is achieved using time discreet control blocks. The current controller blocks are executed at the same rate, $12.5kHz$, as the PWM clock while the speed

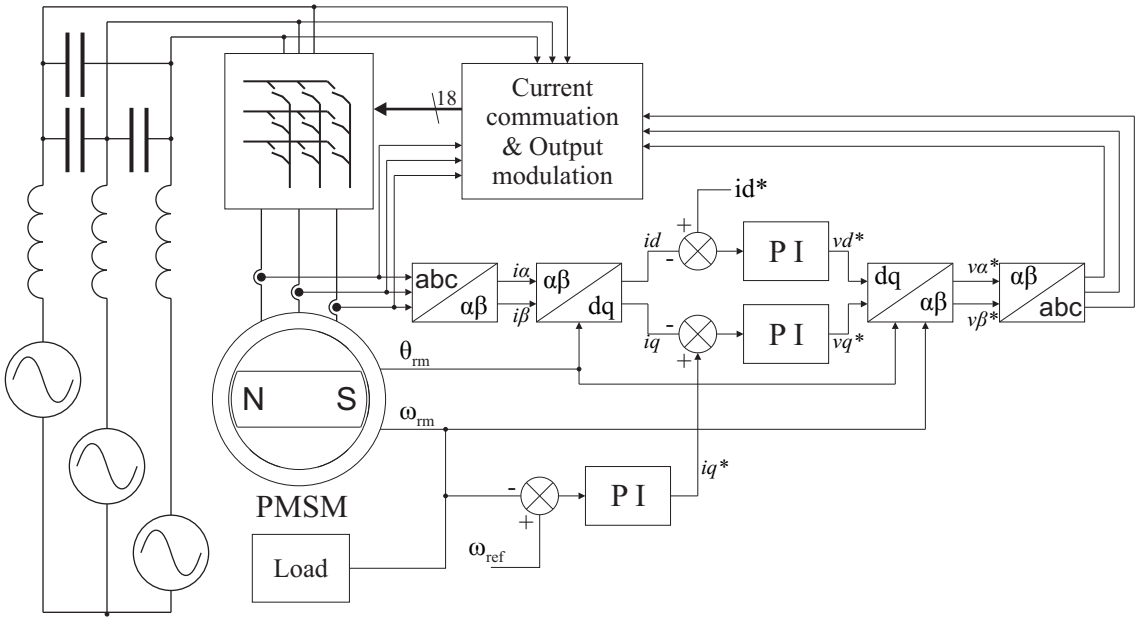

Figure 4.13: Block diagram of the simulated PMSM drive system for TIMES

control uses a slower clock of $1.25kHz$. The modulation calculations (the space vector modulation method was implemented), are also calculated at discreet points using the same PWM interrupt clock. The PWM output vectors are then output one cycle later as in a real system to allow time for calculations. The motor model used includes both electrical and mechanical parameters necessary to simulate a real drive system more accurately.

To validate the simulation structure, a Matrix Converter Permanent Magnet motor drive for an aircraft actuator application and the associated control system has been simulated. The motor and control parameters were based on a 1.5kW demonstrator A320 Electro-Hydrostatic (EHA) Aileron Actuation System [56] provided for the TIMES project. Figure 4.14a shows the performance of the experimental system in the form of a speed reversal of the motor from 10000 rpm to -10000rpm and one motor line current. Figure 4.14b shows the simulated results for the same conditions. The slight differences in the current waveforms are due to the two motors being at different angles when the speed reversal is commanded and hence the point in the

current waveforms when the motors reverse speed is different. The time for the speed reversal is slightly different due to a discrepancy between the data sheet value of the inertia of the machine (used in simulation) and the real value inertia.

The timings of the commutation sequence from one input phase to another can cause a distortion in the output voltage of the matrix converter which is only noticeable in certain operating points. The simulation model can be used to examine the effect of such phenomenon on the whole drive system. Figure 4.15a shows a simple representation of a two phase to single phase matrix converter containing two bidirectional switches.

For explanation purposes, positive current is in the direction shown by I_L and Sa is initially gated and therefore Sa1 is carrying the load current. In this condition the output voltage (V_{out}) will be Va. Figure 4.15b shows the four steps in a commutation sequence from Va to Vb for the positive and negative current directions. The output voltage will commutate between the two input voltages at either step 2 or 3 depending on the polarity of VAB and the load current direction. For the conditions shown in Figure 4.15b, Sb will remain reverse biased until Sa1 is turned off during step 3 and will result in the output voltage changing at this point. If I_L is negative, Sa2 is initially carrying the load current and Sb2 is blocking Vba. In step 2, Sb2 is gated and starts to conduct, reverse biasing Sa2. This results in the commutation of the load voltage at step 2. A similar analysis can be performed for the conditions where Vab is negative.

The result for all conditions is that when the current is positive, the commutation will occur at the point at which the most positive voltage will be applied to the load and when the current is negative, the most negative voltage will be applied to the load. Since the matrix converter is continuously commutating between positive and negative input voltages, the resulting average output voltage distortion changes as the load current changes direction. Any time delay between steps 2 and 3 will cause an uncertainty for the modulator when deciding on the output voltage vector times. This effect can be seen in the performance of the current controller. As the current

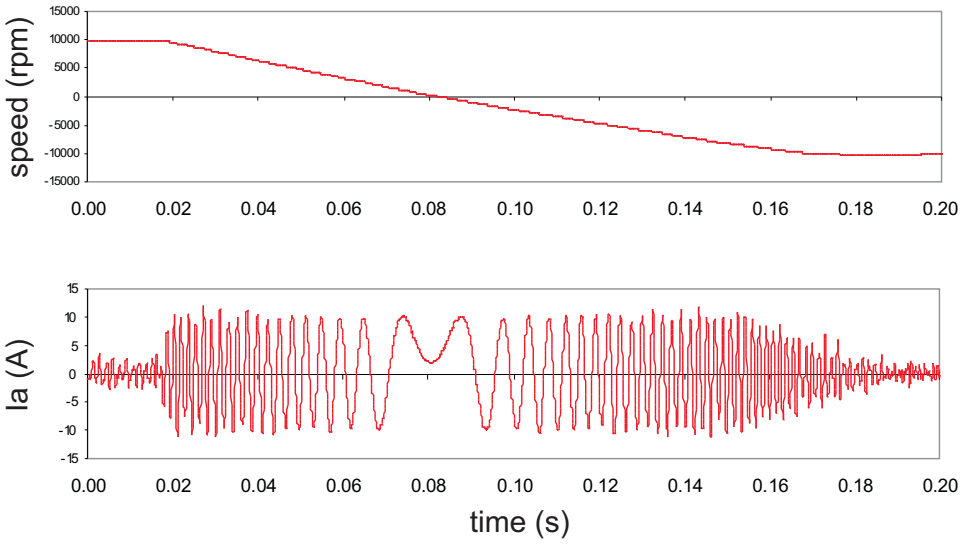

(a) Experimental results

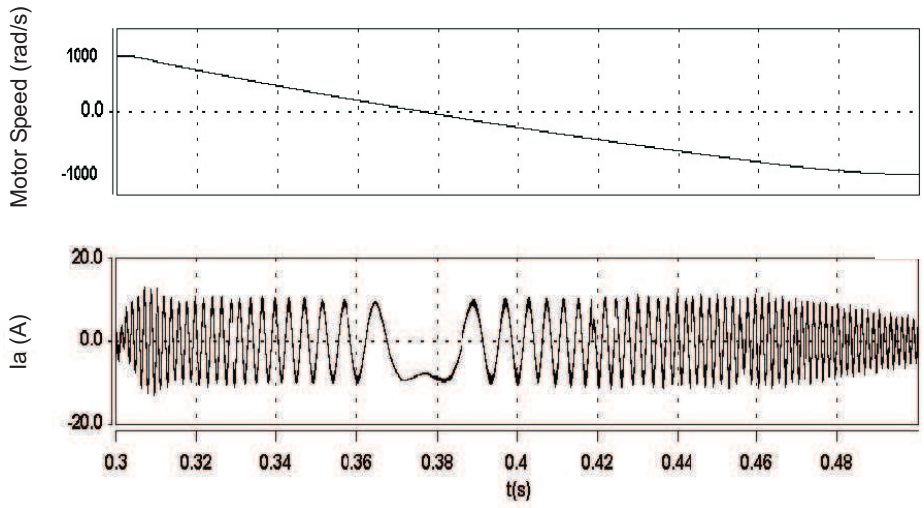

(b) Simulated results

Figure 4.14: Experimental and simulated results of the PMSM drive system for TIMES

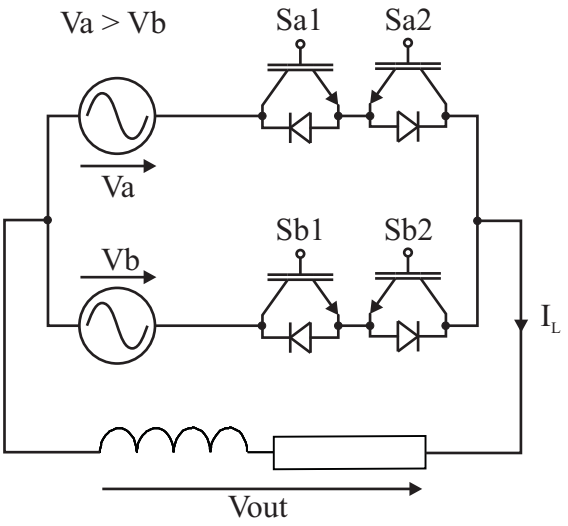

(a) Simplified diagram of a two phase to single phase matrix converter

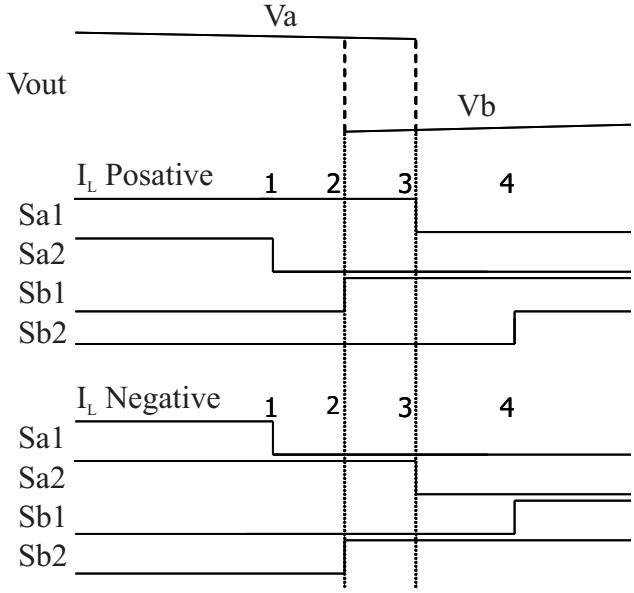

(b) Commutation sequences for positive and negative load current

Figure 4.15: Output voltage distortion caused by commutation times

crosses through zero, the resulting small but fast change in output voltage acts as a disturbance in the current control loop which the controller then tries to compensate for. Results to compare the effectiveness of the simulation structure with those of the experimental system with regards to the change in output voltage due to current direction at zero speed demand are shown in Figure 4.16a and Figure 4.16b. If the speed demand is zero and the actual speed is zero then the current demand will also be zero. As the motor phase current approaches zero, the current controller is demanding the correct voltage to control the current and will be a value to oppose the added voltage introduced by the commutation times. As the current becomes very small and crosses zero, the voltage addition due to the commutation times will suddenly change. This means that the output of the current controller will now be incorrect and the current is propelled away from zero until the PI controller corrects itself and brings the current back to zero. The process then repeats itself in the opposite direction.

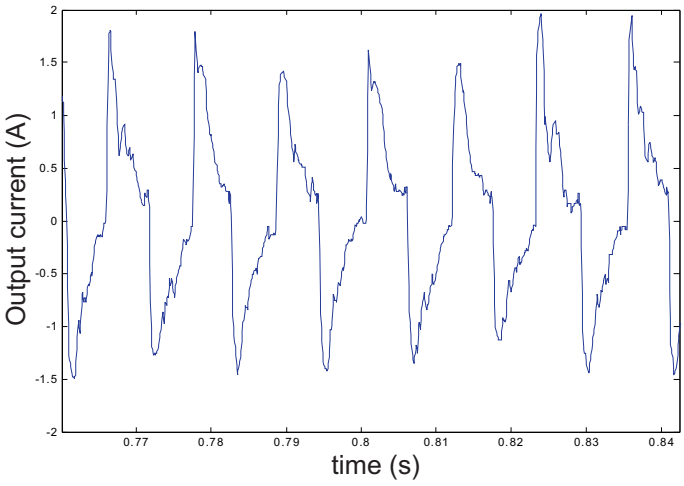

(a) Experimental results

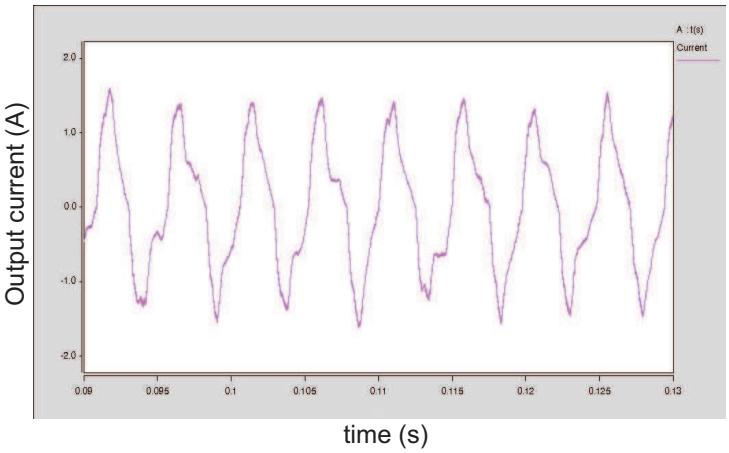

(b)

Figure 4.16: Experimental and simulated current waveforms of the PMSM drive system for TIMES when demanding zero speed

4.2.2 Induction Motor (IM) Drive System

The low torque ripple induction machine is another good candidate for a matrix converter drive system. It is characterised by a simple design, low manufacturing cost, low maintenance and high speed performance where no position sensor needs to be employed. When the stator windings are excited with a balanced polyphase alternating source, a magnetic field is produced in the air gap which rotates at a synchronous speed determined by the number of stator poles and the applied stator frequency [49]. The rotating air-gap flux induces voltages in the rotor windings which are short circuited. Consequently, rotor currents result from the induced voltages which depend on the rotor impedance and produce a magnetic field which, by interacting with the rotating stator field, generates a torque. The generated torque turns the rotor in the direction of rotation of the stator field. As long as the mechanical rotor speed and the stator field synchronous speed are different a torque will be produced and the rotor conductors will not be seen to be stationary by the stator field. The difference between the synchronous speed ω_e and the rotor speed ω_r is known as the slip s of the rotor which is expressed as a fraction of the synchronous speed as follows: $s = \frac{\omega_e - \omega_r}{\omega_e}$.

The induced rotor voltages are characterised by the electrical slip frequency(ω_{sl}), which is the product of the slip and the applied stator frequency. The resulting rotor currents will generate a flux wave rotating at a speed with respect to the rotor expressed as the product of the slip and the synchronous speed while with respect to the stator flux wave it will be rotating at synchronous speed.

The torque produced by the interaction of the magnetic stator and rotor fields is expressed by Equation 4.3:

$$T = -K\, I_r \sin \delta_r \tag{4.3}$$

where the rotor current, I_r, is equal to the negative voltage induced by the air-gap flux divided by the rotor impedance at the slip frequency. The angle δ_r is the displacement between the rotor mmf wave and the air-gap mmf wave while K is a constant. The torque will indirectly depend on the slip since the torque is a function of the rotor

current which depends on the rotor induced voltage, which is slip dependent, and the rotor impedance as mentioned earlier. For low values of the slip, the rotor frequency will be low and it is possible to assume that the rotor impedance is mainly resistive and therefore independent of the slip. The rotor voltage induced is proportional to the slip (via the slip frequency), consequently the rotor current will result in being directly proportional to the slip and so it would also be for the torque. For higher values of the slip the rotor impedance increases due to an increase in the leakage inductance so that the rotor current is no longer directly proportional to the slip while $\sin\delta_r$ decreases. This results in a torque which increases with the slip up to a maximum torque and then decreases for higher values of the slip for the reasons explained above.

It is possible to control the slip at which the maximum torque occurs by changing the rotor resistance. This on the other hand does not allow the reduction of the rotor losses to zero which contribute to directly decrease the motor's efficiency and does not make it an appealing machine for low speed applications. Although this does not make the induction machine the most favourable machine for this project, it has been taken into consideration for this study and analysed in simulation. The drive system, which includes a matrix converter driving an induction motor with its appropriate control, is described in the block diagram of Figure 4.17.

The approach of the simulation model is similar to the permanent magnet synchronous machine drive for TIMES described in the previous section. A vector control scheme is applied to the machine with a speed controller and dq current controllers implemented. In order to perform the correct transformation from the three phase stator quantities to the two axis dq quantities through the intermediate stage of transformation into the $\alpha\beta$ co-ordinates and their inverse transformations, the displacement between the rotor flux vector, which is aligned with the d-axis, and the α-axis, which is aligned to the A stator coil, needs to be calculated. Considering that the dq frame rotates at the synchronous speed, and that it can be expressed as the sum of the slip frequency

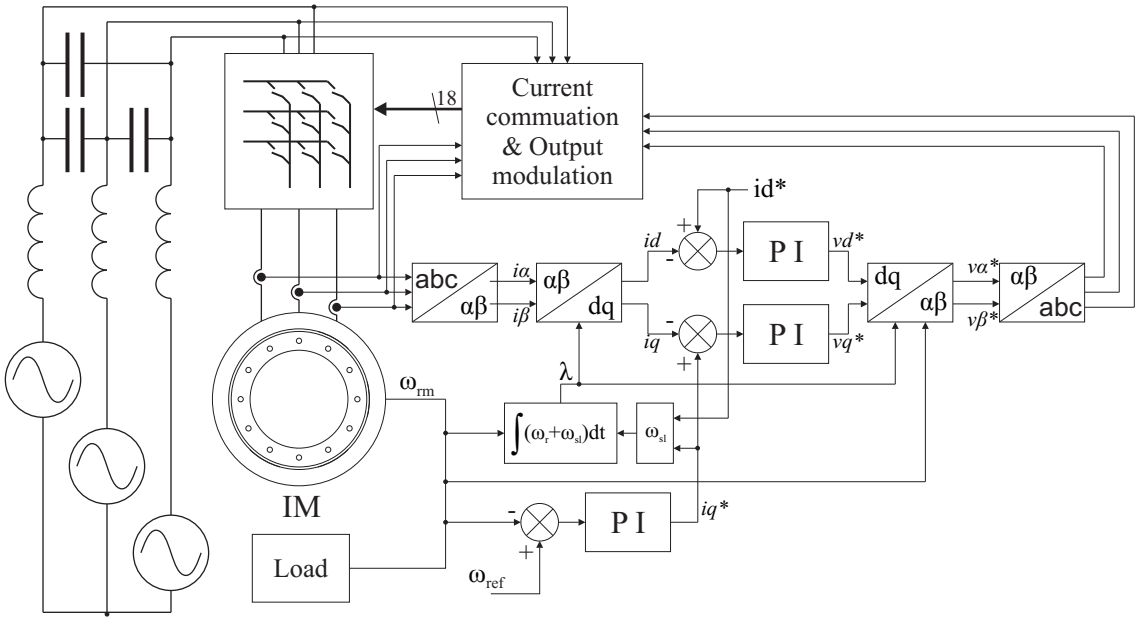

Figure 4.17: Block diagram of the simulated IM drive system

and the rotor speed, it is possible to indirectly calculate the flux angle λ as follows:

$$\lambda = \int \omega_e \, dt = \int (\omega_r + \omega_{sl}) dt \tag{4.4}$$

It was therefore implemented in simulation, by the integration at every sampling instant of the resultant synchronous speed, to determine the angle necessary to perform the above mentioned transformations. From the vector control equations the slip frequency can be expressed as follows:

$$\omega_{sl} = \frac{R_r}{L_r i_{mrd}} i_q \tag{4.5}$$

where R_r and L_r are the rotor resistance and inductance respectively, and i_{mrd} is the magnetising current which can be replaced by the reference for the current producing flux id_{ref} when operating under constant flux (no field weakening). Figures 4.18 and 4.19 show results from the simulation of the induction machine drive. Figure 4.18 shows the drive performance when a square wave speed demand is required. Figure 4.19 shows all of the motor phase currents in more detail for the speed reversal. Figure 4.20 shows the current and voltage of one of the supplies during motor accel-

eration. It can be seen that the power factor is capacitive, this is due to the input filter capacitors and the high input frequency.

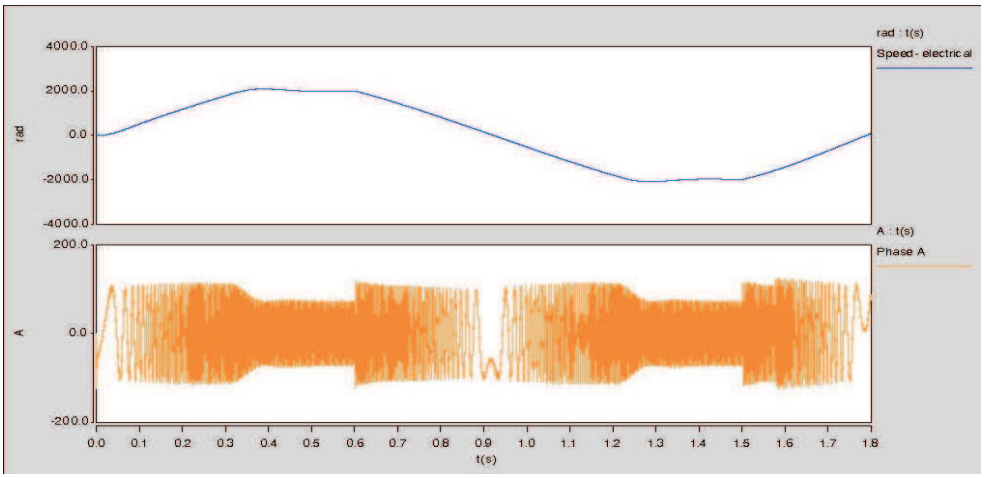

Figure 4.18: Motor speed with and motor line current

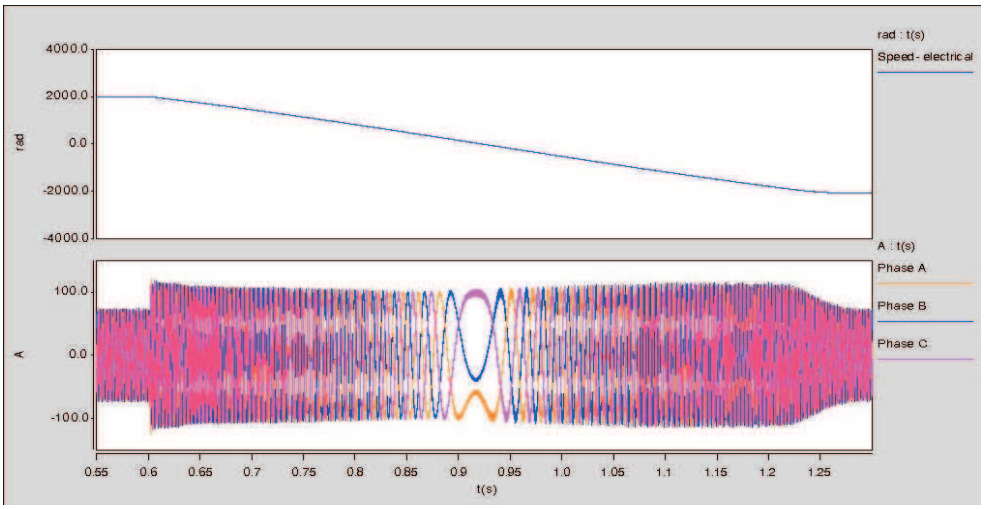

Figure 4.19: Motor speed with and motor line currents during speed reversal

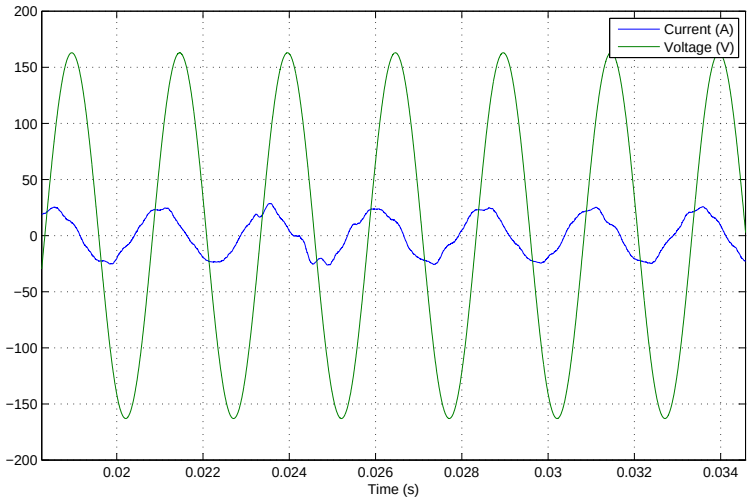

Figure 4.20: Voltage and current of one of the 400Hz input supplies during motor acceleration

4.3 EDAAS Drive System

As has been described in previous sections and, as the literature has presented, each one of the machines considered is characterised by features which make them individually favourable when an aerospace application is considered. Table 4.1 summarises these points when the motor is driven by a matrix converter. An important issue

Feature	Switched Reluctance Machine	Trapezoidal PMAC Machine	Induction Machine	Sinusoidal PMAC Machine
Construction	Simple	Less Simple	Simple	Less Simple
Power/Weight	Good	Best	Good	Good
Robustness	Good	OK	Good	OK
Low Speed Performance	Good	Good	Poor	Good
Power Quality	Poor	Poor	Good	Good
Reliability	Best	V.Good	Good	Good
High Temperature	Good	Poor	Good	Poor

Table 4.1: Summary of the advantages and disadvantages of the different motor types

for this sort of application is reliability and the SRM and trapezoidal PMAC are characterised by a high degree of fault tolerance as mentioned earlier. Particularly preferred for aerospace applications is the "Brushless DC" machine because of the high power to weight ratio which it can offer and the simplicity of its control. It is not the ideal machine if it is to be driven by a matrix converter because of the power pulsations which are directly transferred from the input of the motor to the input of the converter and therefore to the input supply. The issue of power quality is also important for this application. Both of the non-sinusoidal machines would require large filters to be able to be driven by a matrix converter and pass the aircraft power supply specifications.

Given the selected topology of the converter, the application and the results of the analysis of the different machines, it was finally decided to design, build and implement a sinusoidal PMAC machine which used a buried magnet construction with double layer stator windings in order to generate a sinusoidal back-EMF. By implementing a salient rotor, the torque is dependent on both of its components, the "mag-

netic" and the "reluctance" torque and the control of these components is achieved by acting on both iq and id. Each of Figures 4.21 and 4.22 show the motor speed with a motor line current and one with the torque producing current iq respectively. Figure 4.23 shows a supply voltage and current during the acceleration period of Figures 4.21 and 4.22. It can be clearly seen that the quality of the line current is far superior to those of the non-sinusoidal machine drive systems.

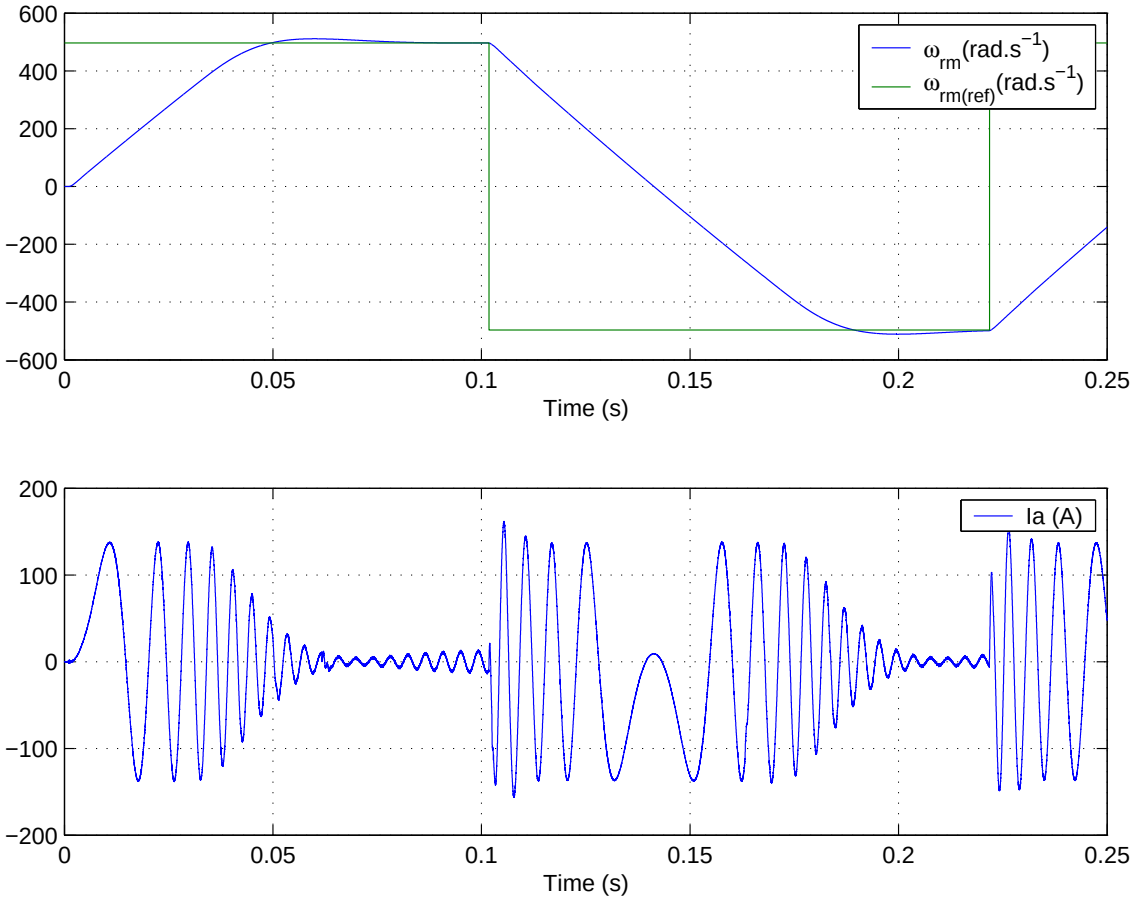

Figure 4.21: EDAAS PMSM - motor speed and motor line current

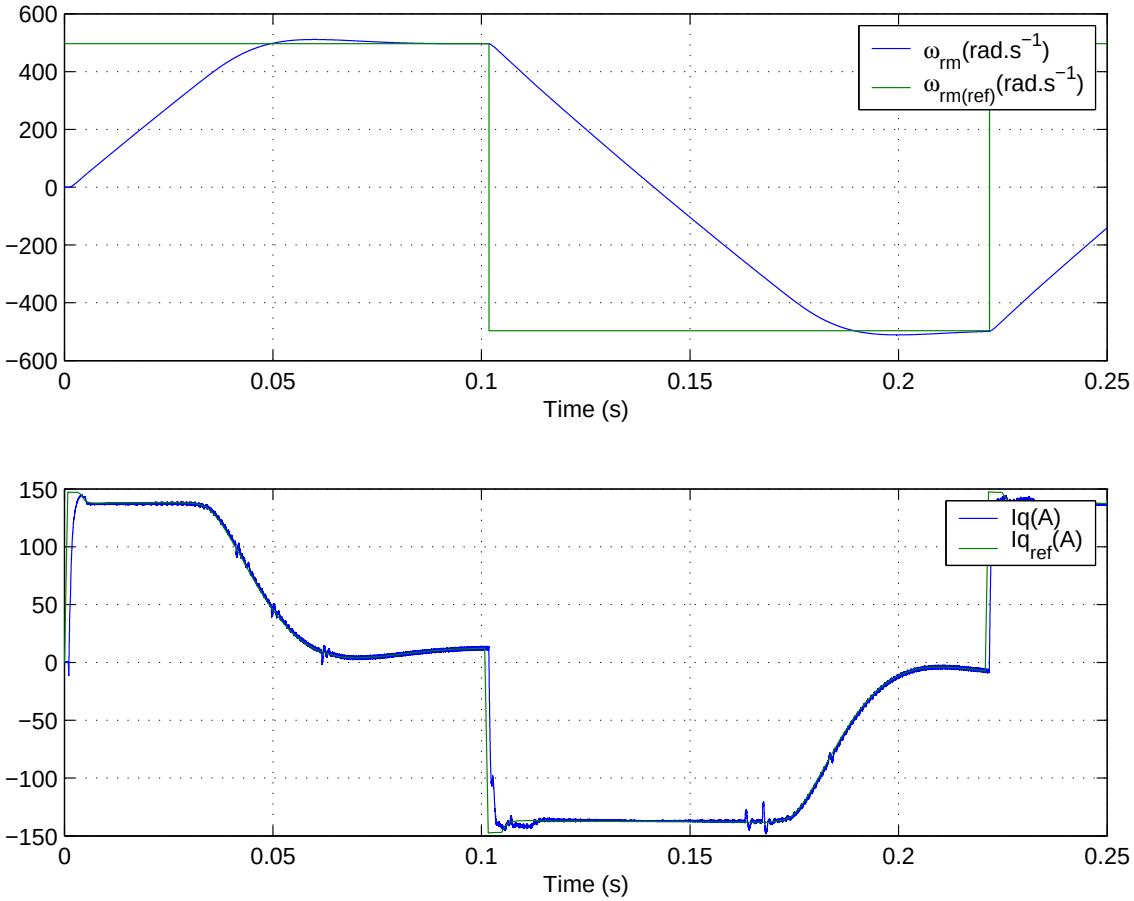

Figure 4.22: EDAAS PMSM - motor speed and i_q, torque producing current

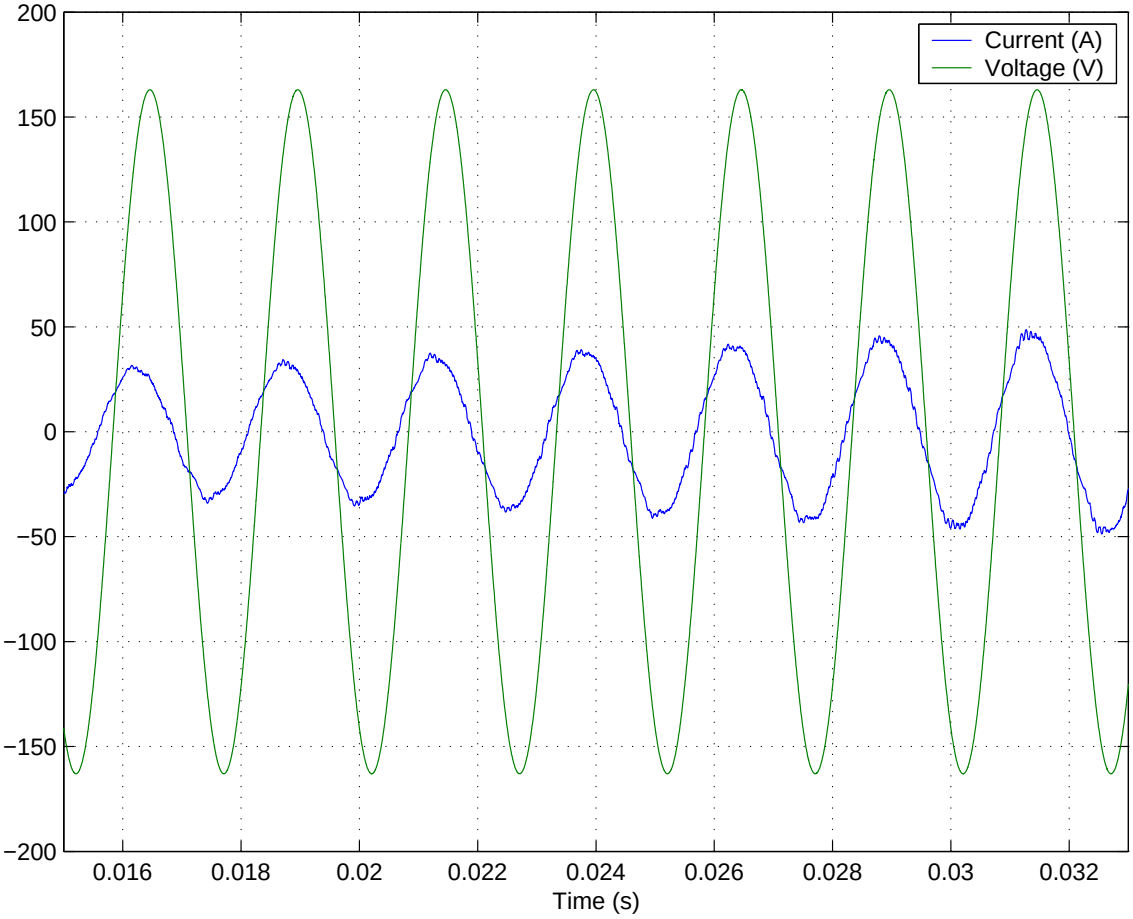

Figure 4.23: Voltage and current of one of the 400Hz input supplies during motor acceleration

4.4 Summary

The analysis of the different matrix converter drive systems has been carried out to investigate the most appropriate topology of machine which could be implemented for the application described in this study, a rudder actuator drive system. Each of the sinusoidal and non-sinusoidal machines has been studied in simulation when driven by a matrix converter and for each of the resulting drive systems the appropriate control strategy has been implemented. The aim was to highlight their advantages and disadvantages with the prospect of real implementation in order to optimise the design of the drive. The choice of the machine implemented is mainly dependent on the topology of converter used to drive the machine together with the implications on the application involved and the desired control strategy.

Chapter 5

Prototype Matrix Converter Implementation

The initial design of the prototype matrix converter has been analysed and investigated through simulations in SABER, as it has been shown in Chapter 4, leading us to the next part of this study, the implementation of the prototype matrix converter. This Chapter will describe what is included in the power circuit and how it has been achieved and the hardware and software implementation of its control structure. The assembly and commissioning of the overall system will be discussed in Chapter 6. A block diagram of the matrix converter implementation is shown in Figure 5.1.

Before introducing the following sections it is important to mention the input supply conditions and the desired output specifications. The power converter is supplied with a variable frequency three phase supply from 360 to 800Hz, where the line to neutral voltage is 115V rms.

The main feature of this drive is linked to its application and its response to the worst case operating condition that is the abnormal operating condition of an engine failure. In this case the rudder is required to compensate for the resultant yaw moment providing a steady force to maintain a required rudder offset which will

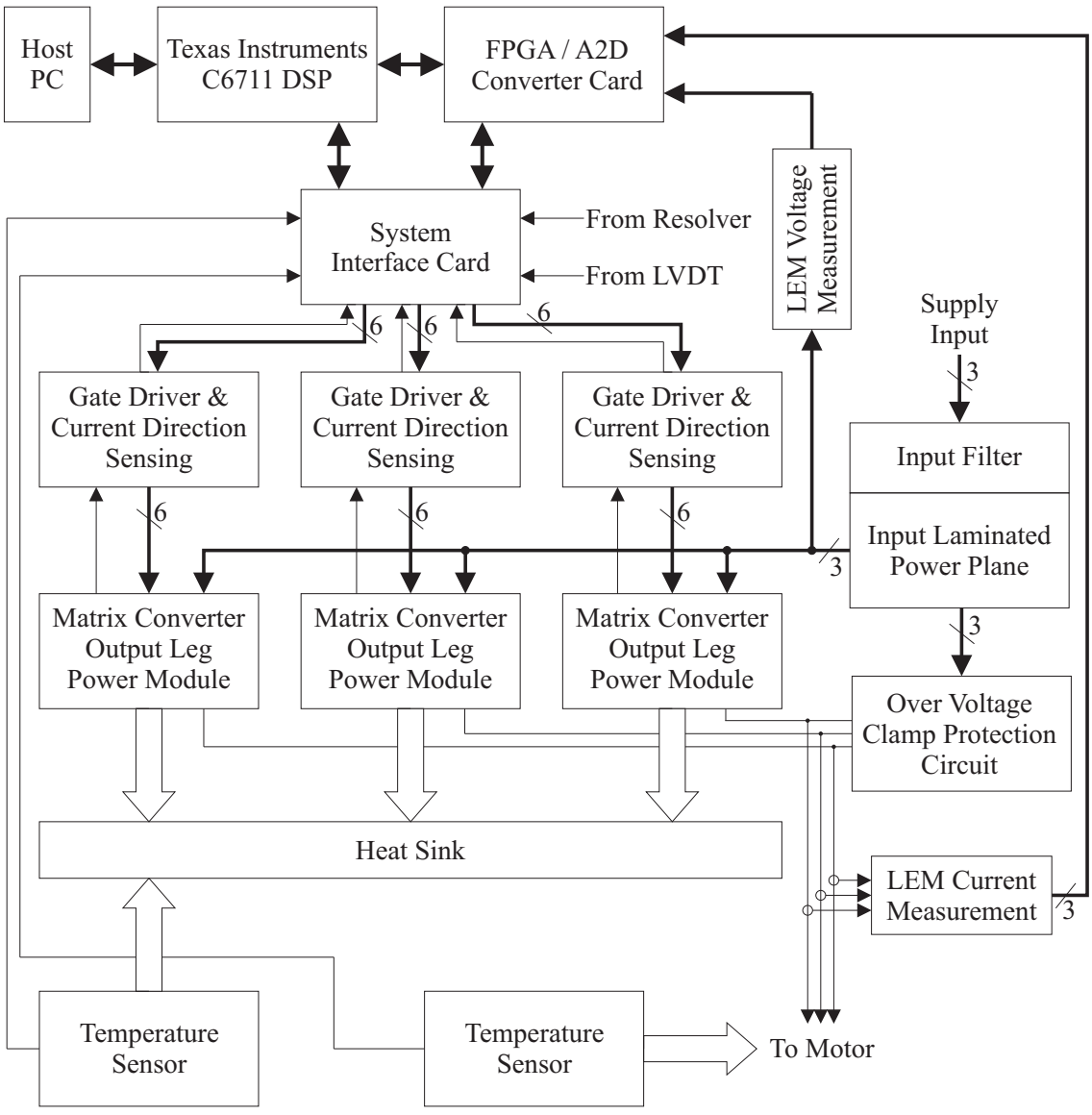

Figure 5.1: Block diagram of the matrix converter implementation

allow the aircraft to complete the flight.

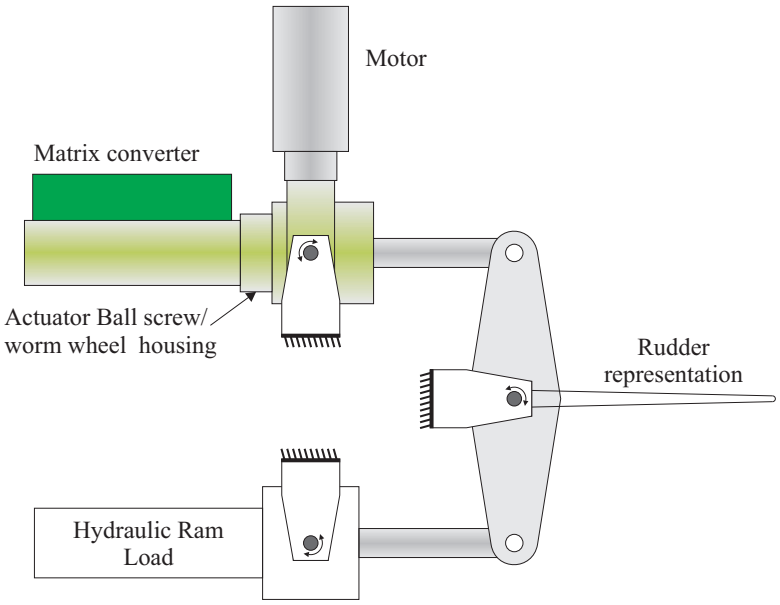

Figure 5.2: Load rig

In order to practically demonstrate the actuator operation in a lab, a test rig has been built. A simplified representation of the rudder actuator drive system is shown in Figure 5.2. The matrix converter drives a motor which is in turn connected to the actuator through a worm wheel/ball-screw and the output of the ball-screw is connected to a 200mm lever arm which operates a rudder surface. The load applied to the rudder actuator will increase linearly from 0kN at 0 degrees to a maximum load of 159kN at 30 degrees in either direction. The maximum torque and speed required for the drive is 17.9Nm at 9045rpm respectively which leads to the requirement that the motor should be able to provide 16.9kW at its output.

In the abnormal condition mentioned above the drive is required to deliver half the rated torque continuously at zero speed. This is the worst case in terms of heat dissipation for the actuator since it can occur for a long time whereas the high power situation occurs much less frequently and for much less duration. The thermal analysis, as mentioned previously, was carried out by the School of Mechanical Engineering.

Their work involved the design and construction of a suitable heat sink to which the matrix converter could be attached.

This was a difficult task due to the requirements imposed on the drive system. It could not be force cooled with a fan since fans can decrease the system reliability. The air in the rudder section of the aircraft can be anything up to 75° C when in a hot, sunny country. The surface skin of the rudder section could not be used as a heat sink since in future aircraft, such as the Boeing 787, the whole structure is likely to be constructed from non-metallic composite materials. The final heat sink was able to be made larger than the space required for the matrix converter by incorporating the oilcan/ball screw housing into it. Figure 5.3 shows a thermal image of the heat sink while it is being tested.

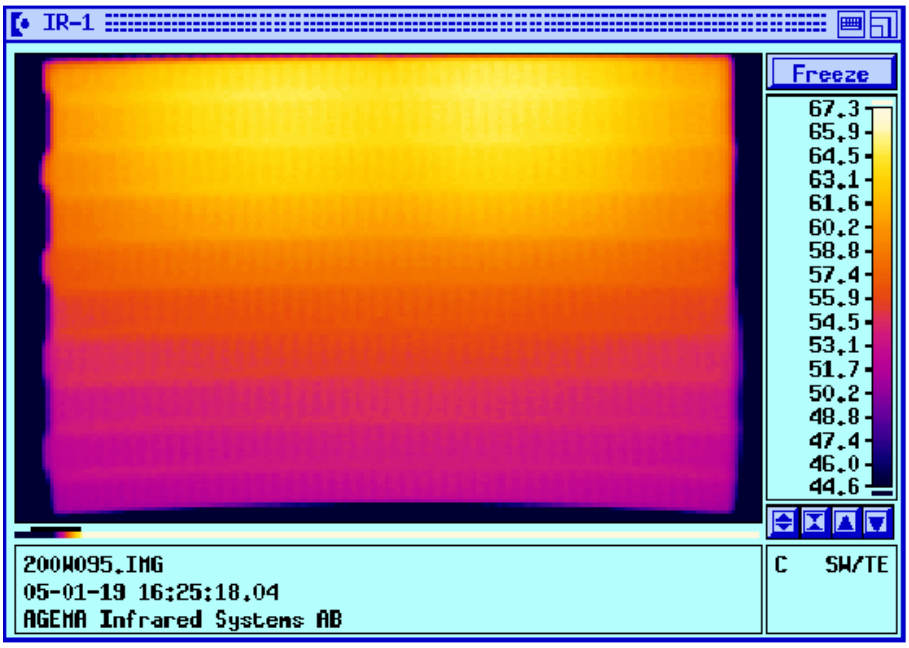

Figure 5.3: Thermal image of the heat sink under test

The individual components that made the EDAAS demonstrator actuator were designed to be completely integrated with the actuator. This meant that separate heat sinks for the actuator and power electronics could be integrated into one, which was

also used to provide the housing for the ball screw. This integrated concept means that the actuator does not need any extra units containing the power electronics, for which space has to be allocated on the aircraft. This meant that the power electronics needed to be optimised in terms of the space available around the actuator. The following sections will describe the design and construction of the matrix converter.

5.1 Matrix Converter Power Circuit

At the time when the specifications for this project were discussed, one of the best candidate configurations of the drive system required was to develop a matrix converter drive system capable of delivering 30kW. Due to the availability of silicon components on the market and the initial design specifications, the converter's power circuit was sized accordingly even though in the final implementation a 20kW machine was required. The power converter had to address not only the electrical specifications but also restrictions linked to the nature of the application. The space available on the actuator housing has been optimised to implement the electronics and special care has been adopted for the choice of passive components used to realize the power circuit. Indeed no electrolytic capacitors have been used for either the input filter or the protection circuit. This is important because of the reasons outlined previously in Section 3.8. The performance of the power converter, as will be shown later in Chapter 6, confirms the validity of the design and compactness of the power converter. The main elements of the converter's power circuit are described in the following sections and include the power modules and low inductance power plane which allow the input power connections to be connected to the inputs of the power modules, the IGBT gate drive boards and the active over-voltage clamp circuit.

5.1.1 Power Modules

The matrix converter consists of three power modules each containing three bidirectional switches connected to form an output phase of the matrix converter. They have been custom made to aircraft specifications for this project by Semelab(UK). The modules are rated at 300A and 600V which means that the matrix converter implemented could easily drive systems up to 40kVA given the same three phase input supply. To achieve this current rating each individual switch is the result of two IGBT chips rated at 150A,600V connected in parallel, therefore a total of 4 IGBT die chips were used per bidirectional switch.

The IGBT chips used were manufactured by Infineon technologies and are developed in Non-Punch Through (NPT) technology. The particular way that the emitter has been implemented introduces better performance such as lower switching losses and higher switching robustness [57]. Each IGBT in a bidirectional switch has two diode dies with the same ratings mentioned above connected in antiparallel to block voltage when it is not conducting and to allow a path for the current when the other IGBT in the bidirectional switch is conducting. Figure 5.4 shows the layout of the circuit within a power module.

The circuit provides three bidirectional switches, one for each input phase (C1,C2,C3) and two ultra fast diodes with the same current rating as the IGBTs, connected in antiparallel on the path of the output phase connection. The voltage across these diodes will be used to generate the information on the sign of the output current of the module. This information is necessary to carry out a safe commutation of the IGBTs. The signal connections (Gif,Gir,Eif,Eir where i=1,2,3 and those for the current direction detection) are used by the gate drive boards which are mounted on the top of the modules.

The base of the power module is made from a metal matrix composite (MMC), aluminium silicon carbide (AlSiC). The main reason for this is that the thermal expansion coefficients of the aluminium nitride insulating tile, to which the semiconductor de-

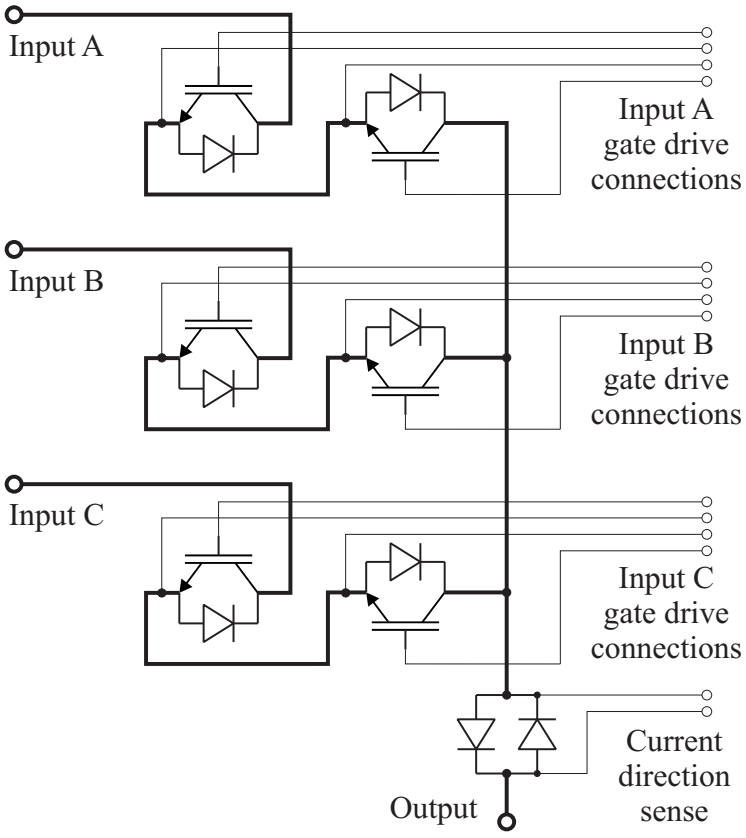

Figure 5.4: Power module circuit diagram

vices are mounted, and the AlSiC base can be matched. This increases the maximum number of thermal cycles to which the modules can be subjected when compared to a copper base and hence the reliability is increased. AlSiC base plates also offer good thermal conductivity and lower weight. A diagram to show the physical size and layout of the power module is shown in Figure 5.5 and a photograph of the power module is shown in Figure 5.6.

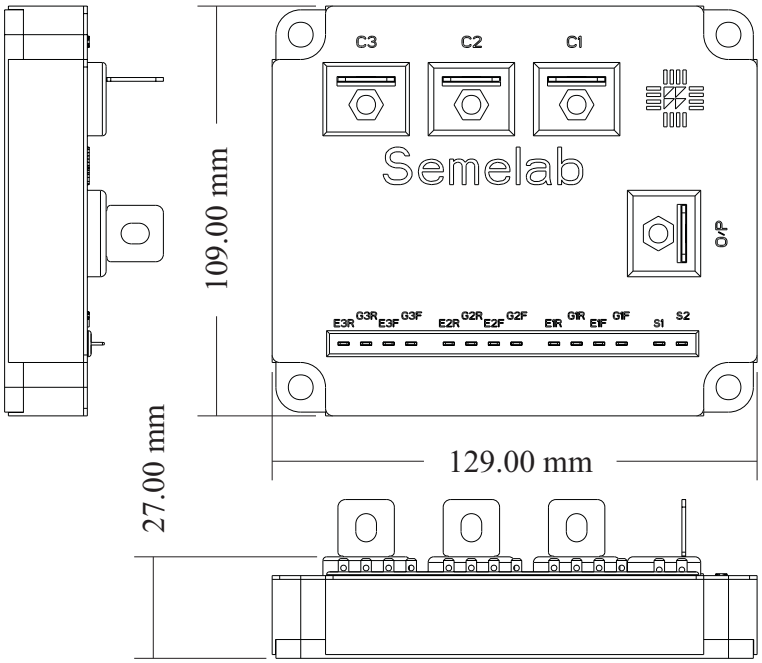

Figure 5.5: Line drawing of the power module

Figure 5.6: Photograph of the power module

Initial tests of the power module features have proved the high speed performance of the IGBT chips. Figure 5.7 shows the switching characteristics at the turn on and turn off of one switch (two 150A dies in parallel) in the power module. These tests helped to decide on the exact value of the gate resistance Rg to use. The value of Rg influences the turn-on and turn-off behaviour of an IGBT. Higher values of Rg reduce the switching transients, but increase the switching losses whereas a lower resistance decreases losses and increases the switching speed and hence transient problems. The smallest value of resistance that would prevent the overshoot at turn off becoming too large was chosen.

5.1.2 Low Inductance Power Plane and input LCR filter

In order to minimise the stray inductance of the interconnections between the IGBT modules and the input power connections a laminated busbar has been employed which includes connections for the input filter capacitors. The power plane has been

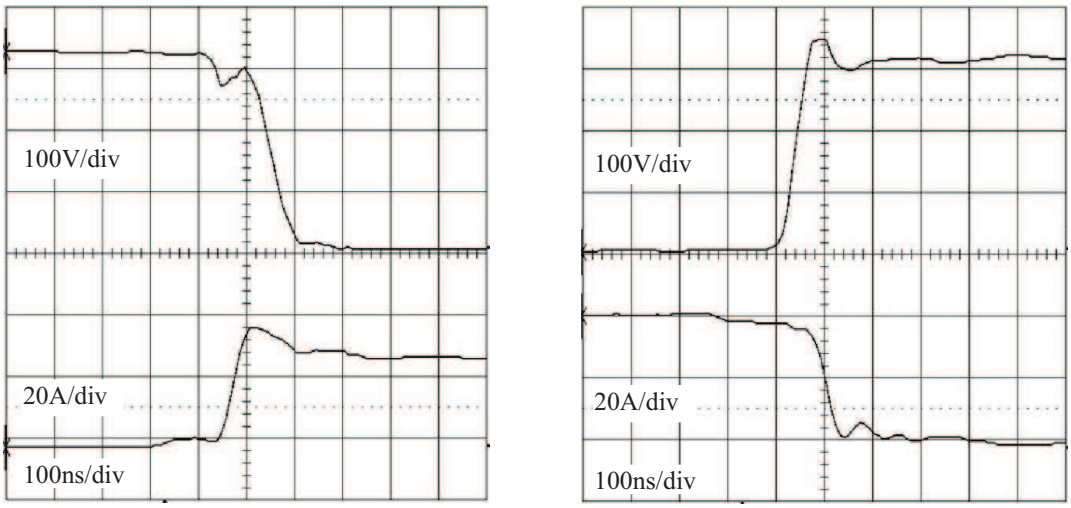

(a) Turn on (b) Turn off

Figure 5.7: Device voltage and current waveforms

designed to include three 0.8mm copper layers, one for each input power connection separated by two 0.5mm insulating layers made of nomex, normally used for insulating the windings in electrical machines. The different layers were glued together with epoxy resin. Figure 5.8 shows a diagram of the construction of the power planes. Connections to the different copper layers was achieved by first milling out the un-

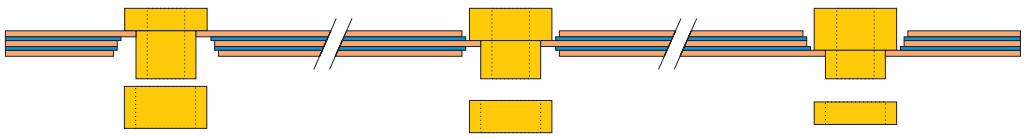

Figure 5.8: Construction of the connections to each layer of the power plane

wanted layers above and/or below the connection layer. A different sized cutter was used for consecutive layers to achieve a staggered/stepped profile. Connections to the different layers were created using different sized brass inserts. Holes through the power plane were made to be slightly smaller than the size of the brass insert. This creates an interference fit to ensure a good mechanical and electrical connection. A correctly sized brass washer, again with a hole slightly smaller than the brass

insert was used to complete the connection. The washer and brass insert were then compressed onto the power plane.

Due to the main factor which influences the criteria of the design of the power circuit, that is the physical space available for the electronics, on a side view the power plane is characterised by an L shape. This layout has contributed greatly to a very compact final assembly of the power converter on the actuator housing.

Figure 5.9 shows a photograph of the finished power plane. Polypropylene film capacitors with a low equivalent series resistance and inductance were chosen to further minimise the circuit parasitic elements. The input filter was designed by choosing C

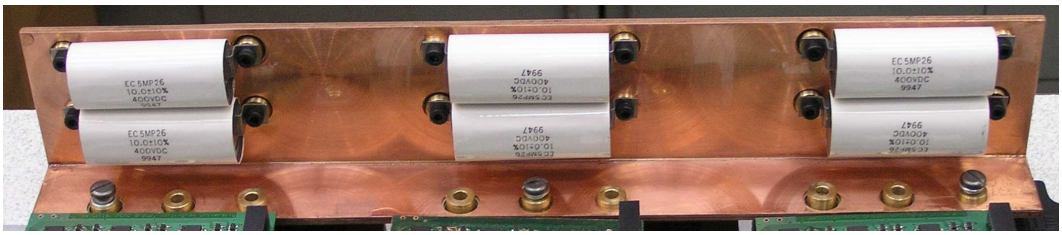

Figure 5.9: Photograph of the power plane and input filter capacitors

first, its size, type and ratings being based on the application. As mentioned earlier metallised polypropylene capacitors have been used and a total of 20μF capacitance per line to line (60μF equivalent line to neutral) was initially chosen.

Having considered that the input supply frequency varies in the range of 360Hz-800Hz and that the switching frequency is of 12.5kHz in order to avoid interference with these frequencies and their harmonics, a resonant frequency between 4kHz-5kHz has been initially assumed.

A parallel damped single section filter configuration [58], was chosen for this application as shown in Figure 5.10, where a resistor is placed in parallel with the inductor to provide appropriate damping according to the value or resistance selected. A very small value of R would result in a high degree of damping but a higher dissipation of energy.

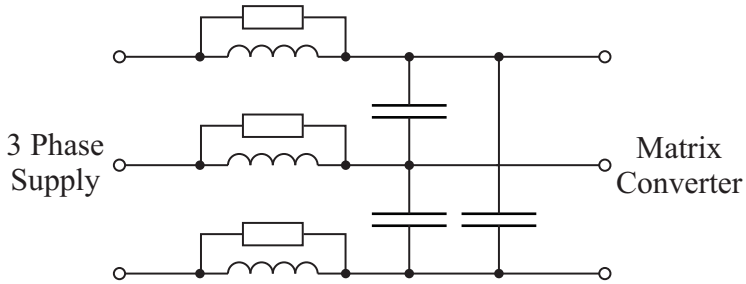

Figure 5.10: Schematic diagram of the input filter

Simulations of the input filter connected between the input supply and the converter have been run to fine tune the values of both the capacitance, the inductance and the resistor. Due to the necessary AC current rating of the capacitor two capacitors of 10μF each were connected in parallel per line to line. A three phase inductor of 60μH and rated at 800Hz and 90A rms and three resistors of 8Ω each have been implemented.

5.1.3 Gate Driver and Current Direction Detection Circuit

The gate driver and the current direction detection circuits have been designed to optimise their functionality and the space available on and around the power modules. A block diagram of the main components of the gate drive circuit is shown in Figure 5.11. These circuits have been implemented on a single printed circuit board (pcb) per power module, described from now on as the gate drive pcb. A schematic of the gate drive circuit for one bidirectional switch is shown in Figure 5.12(a). The logic signals generated from the FPGA to drive the gates of the two IGBTs in the bidirectional switch are transmitted through the interface board via a fibre optic cable. The fibre optic receiver (HFBR-2521)(F1)inverts the logic signal collected so it is first sent through an open collector inverting logic gate(U3). The output of U3, together with the pull-up resistor R1 is used to drive a gate drive optocoupler (U5) which provides galvanic isolation between the DSP/controller ground and the emitter (local ground) of the bidirectional switch together with an output drive voltage swing

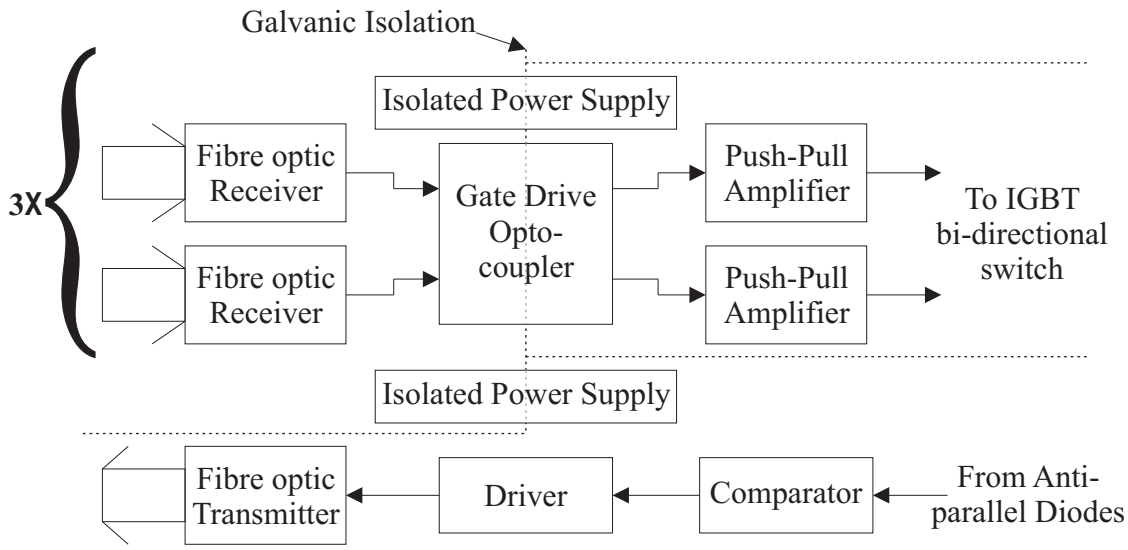

Figure 5.11: Block diagram of the important parts of the gate drive circuit

capability of ±15V. The output of U5 does not have enough current capability to directly drive the size of IGBTs used in the power modules. Therefore a push-pull amplifier is provided with a series resistor (Rg) which will influence the rise and fall times of the IGBT driven. A value of 10Ω was chosen for Rg in the final design of the gate driver pcb to prevent overvoltages across the IGBT due to the high speed performance and circuit parasitic inductances especially when turning the IGBT off.

Power supply isolation between the ground of the 5V control electronics supply and the local signal references is provided by dc to dc converters to generate isolated ±5V and ±15 V from the same 5V input supply. For the current direction detection circuit a Newport NMH0505S was used while for the gate driver circuit a Texas instrument DCP020515DU was chosen especially for its flexibility. It is a 2W DC-DC converter with a maximum 1kV isolation potential with the possibility of being directly connected in parallel with another if higher power is required.

Figure 5.12(b) shows the circuit used to detect the current direction information which is fed back to the FPGA to carry out a safe commutation of the IGBTs. The communication to and from the FPGA is done via fibre optic cable interfaced with

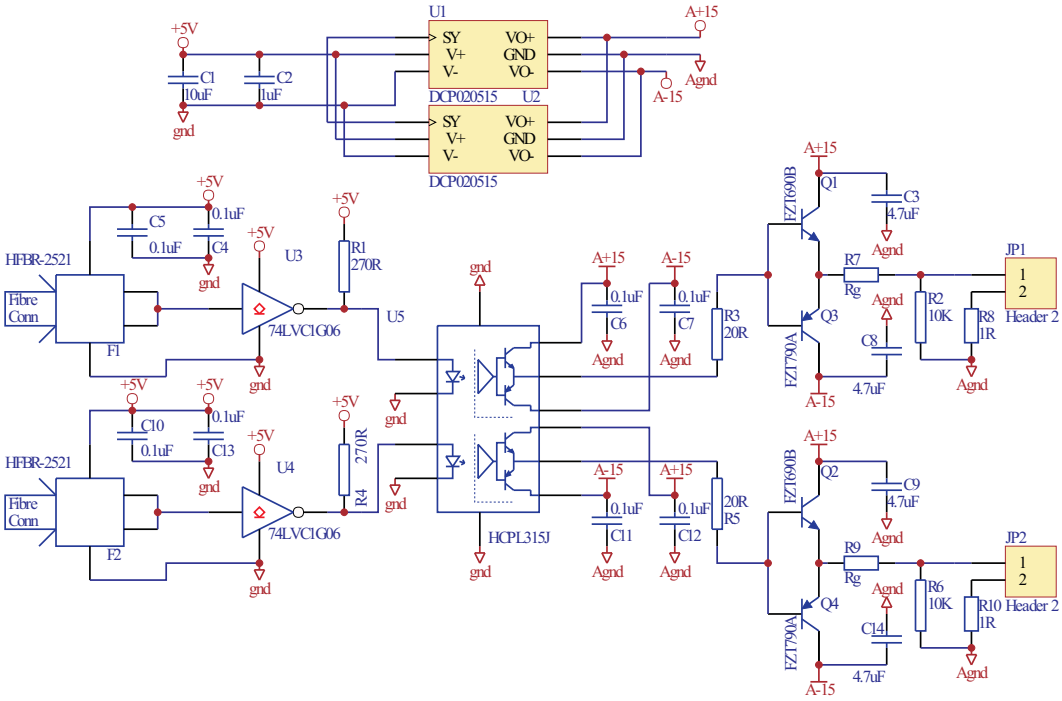

(a) Gate drive circuit

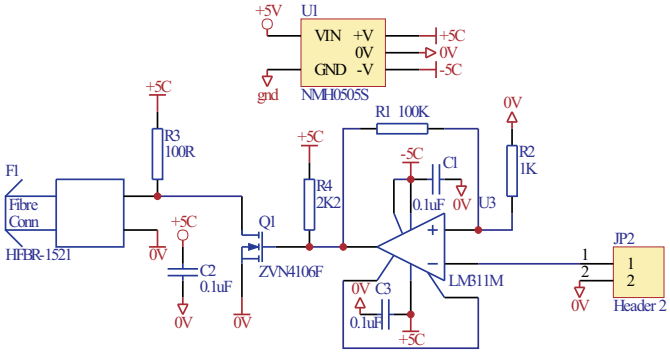

(b) Current direction circuit

Figure 5.12: Diagrams to show gate drive and current direction detection circuits

the appropriate transmitters and receivers to provide both voltage isolation and good noise immunity. The voltage across the two antiparallel diodes built in the power module caused by a positive or negative load current provides the current direction information. The voltage signal is input to a comparator (U3) and its logic output drives a MOSFET (Q1) with a pull-up resistor which is chosen to provide enough current to drive the fibre optic transmitter (HFBR-1521).

As mentioned previously at the beginning of this section, the gate drive pcb has been optimised in size to be able to directly use the space above the power module between the signal connections and the input and output power connections as shown in Figure 5.13. The aim for it is a more compact arrangement of the whole power circuit together with the active over voltage clamp as will be shown later in the description of the assembly of the prototype matrix converter.

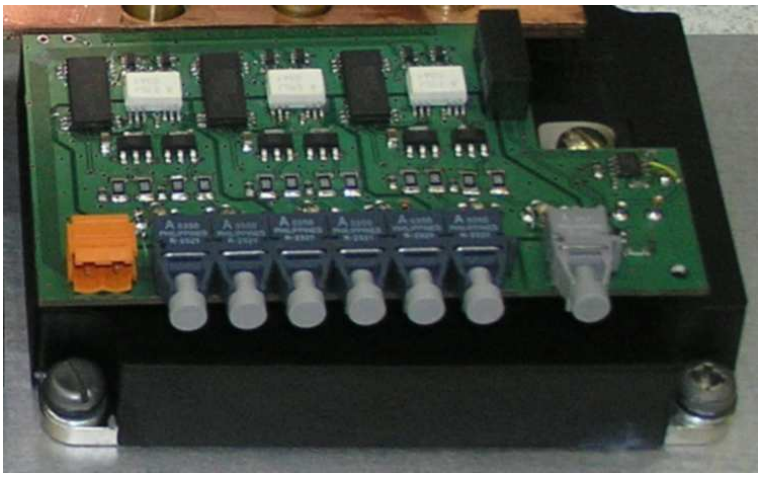

Figure 5.13: Photograph of gate driver board mounted on the power module

5.1.4 Circuit Protection

As mentioned earlier one of the most desirable feature of the matrix converter topology when implemented in aircraft applications is the absence of the DC link typical in

other voltage source inverter topologies. Therefore no electrolytic capacitors are used in a matrix converter. A direct consequence of this is that the matrix converter is not provided with an energy storage facility when the load energy needs to be removed in an emergency situation, such as failure in the commutation process, over-current situation or when powering up the matrix converter which sometime can cause high voltage at the input of the converter if the filter resonates.

By far the most widely used protection strategy employs the use of a high speed diode bridge connected to each input and output phase of the matrix of bidirectional switches and a capacitor [26][27][59]. A schematic showing this arrangement can be seen in Figure 5.14. This arrangement protects the device matrix from open circuits of the load during a shutdown and can prevent ringing of the input filter when the utility supply is turned on. The largest advantage is gained when using a current direction based commutation strategy since a mistake in this type of commutation strategy results in a load open circuit so the converter can be protected against commutation failure if the load current is small and unreliable. It cannot however protect against a continuous commutation failure due to current direction detection circuit malfunction since the clamp capacitor would rise to unacceptable levels. During this situation the converter would have to stop before destruction occurred. The input line to line short circuits which may result from failures in voltage based commutation cannot be protected against using this method.

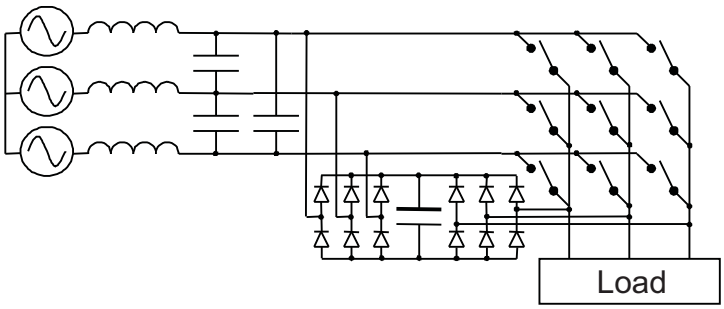

Figure 5.14: Diagram of a matrix converter with diode bridge clamp

The number of diodes used in this arrangement can be reduced to six [59] but this

involves the use of a mixture of common emitter and common collector arranged bi-directional switches. This may not be feasible because this makes the packaging of the semiconductors more difficult since power connections to the centre point of the bidirectional switches are needed.

All of the inductive load energy must be stored in the capacitor without creating dangerous over-voltages so the capacitor must be sized correctly. The size of the input capacitor is calculated based on the size of the maximum stored load energy and the maximum available clamp voltage [59],[60] and can be calculated as follows:

$$W_{Load} = \frac{1}{2}L(i_a^2 + i_b^2 + i_c^2) = \frac{3}{4}L\hat{I}^2 \tag{5.1}$$

The maximum load energy is calculated in (5.1) where W_{Load} is the energy stored in the inductance of the motor, L is the equivalent line inductance of the motor and i_a, i_b, and i_c are the line currents of the motor. The change in stored energy of the clamp capacitor from its initial voltage to its final voltage can be used to calculate the size of capacitor and is shown in (5.2):

$$W_{Load} = \frac{1}{2}\,C_{Clamp}(V_{MAX}^2 - V_{INI}^2) \tag{5.2}$$

where, C_{Clamp} is the capacitance of the clamp capacitor, V_{MAX} is the maximum allowable clamp voltage, V_{INI} is the initial clamp voltage and W_{Load} is the energy stored in the load inductance. The suitability of this system for the application can be ascertained by calculating the necessary size of the clamp capacitor. Some information about the drive characteristics used in the calculations can be seen in Table 5.1. If a maximum current of 1.5 times the peak nominal current is used as

Peak Motor Current	147A
Drive Supply Voltage	200V
Voltage Limit of Devices Used	600V
Max Allowable clamp Voltage	500V
Initial Clamp Voltage	282V
Motor inductance	0.646mH

Table 5.1: System parameters used to design clamp circuit

a worst case current during shut down, the system would need a clamp capacitor of

276μF. These calculations were based on the initial clamp voltages shown in Table 5.1 which are the theoretical values obtained from the peak to peak value of the supply but in practice the initial voltage is slightly higher because of switching harmonics on the filter voltages and parasitic elements within the power circuit. A slightly larger capacitor would be needed. Using the same type of high temperature film capacitors used for the input filter circuit would require a very large volume compared to the converter and hence an electrolytic capacitor should be used for the clamp. This is undesirable in an aircraft (and any other weight / reliability critical) application. A large clamp capacitance may also need a pre-charging circuit when turning on the power to the circuit to prevent unacceptable inrush currents [60] this would further add to the complexity of the circuit. A different approach was needed.

A system was needed that would enable the use of smaller film type capacitors but to still be able to dissipate the peak energy necessary during a shutdown and be able to handle a certain degree of circuit failure to potentially increase the survivability of the circuit. The same high speed three phase diode bridge mentioned above, connected both to the inputs and the outputs of the converter was used together with three small polypropylene capacitors of the same type used for the input filter, connected in parallel to make an equivalent of 30μF. To be able to control and limit the amount of energy stored in the capacitor, a resistor in series with an IGBT has been connected in parallel with the capacitor as shown in Figure 5.15 to enable energy from the clamp to be dissipated. An hysteresis control drives the switching of the IGBT. Once the IGBT is ON the energy in the capacitor is dissipated through the resistor. Simulations in SABER have been run to determine the voltage and current capability of the IGBT and the resistor employed in the control of the clamp circuit. Results of the SABER simulation can be seen in Figure 5.16.

The simulation starts at the point where the load current is at a maximum and the drive has tripped, sending all of the load current through the clamp circuit. The clamp capacitor voltage initially rises and the clamp IGBT then turns on. As the load current reduces, the energy in the clamp is removed by the dissipation resistor but while the load current is still high, the capacitor voltage continues to rise until

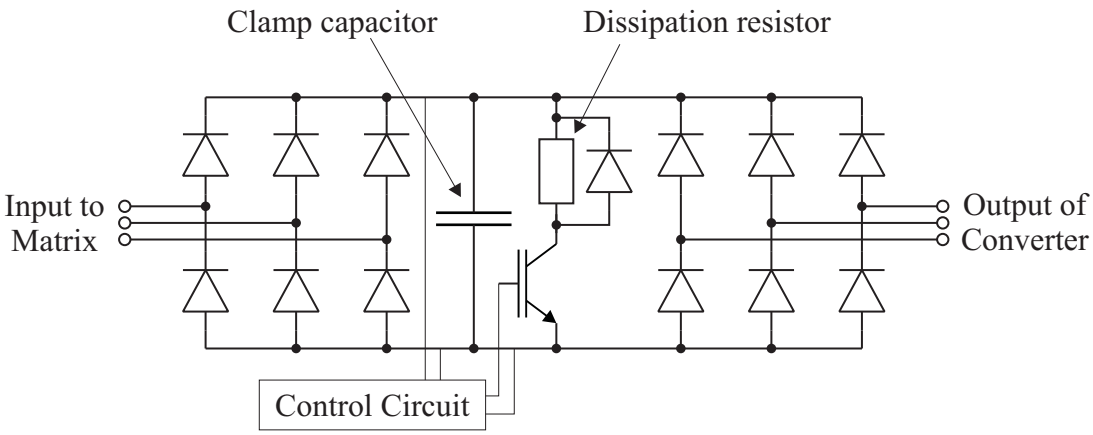

Figure 5.15: Schematic diagram of the diode bridge clamp circuit

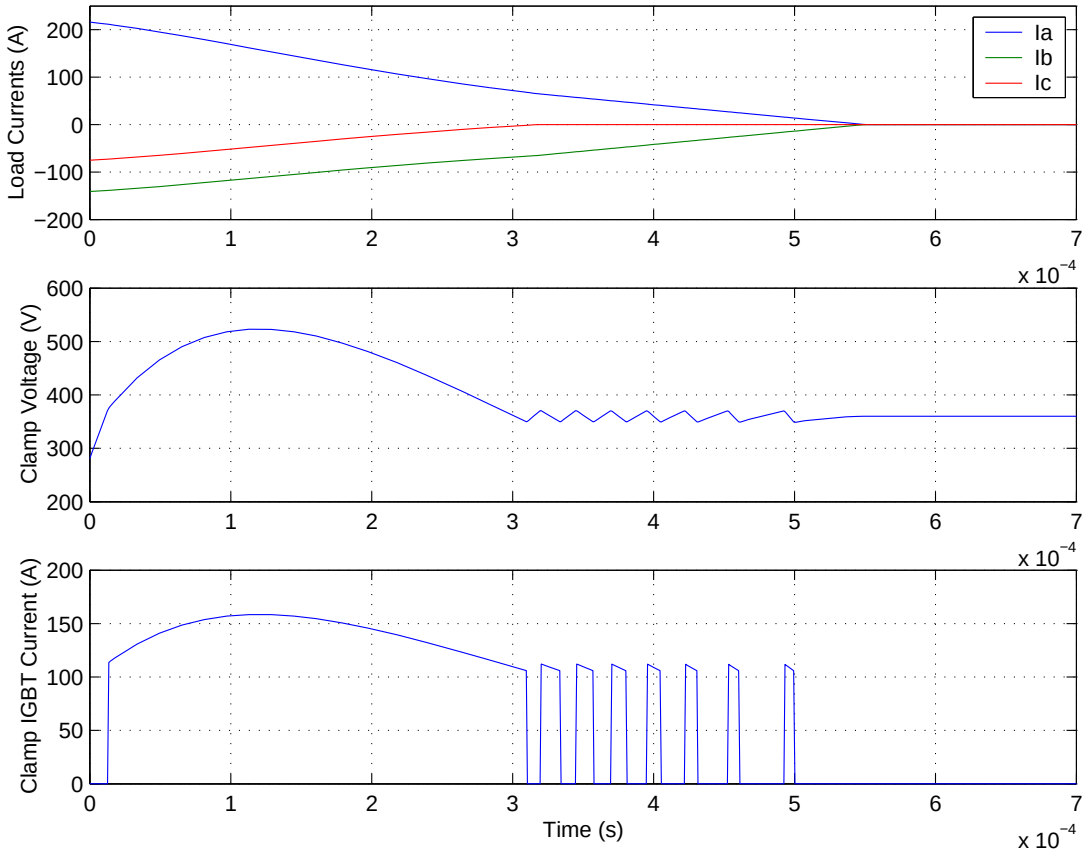

Figure 5.16: Simulation results of the clamp circuit

a point is reached at which the dissipation current is the same as the load current. At this point the clamp capacitor voltage falls and finally the hysteresis control can be seen as the remaining energy is removed from the motor windings. The resistance used for the dissipation resistor was 3.3Ω and was constructed using four, cement encased, wire wound resistors.It can be seen from Figure 5.16 that the IGBT only needs to conduct a peak current of 150A for a very short time.

The voltage across the capacitor of the protection circuit is measured and fed to the clamp control circuit which generates, depending on the voltage amplitude, two digital signals, the gate drive signal for the IGBT and a signal which will shut down the converter. The first signal is used to control the clamp over-voltage within an hysteresis band. The second signal is sent to the FPGA and is active when the clamp voltage has exceeded a maximum safe value.

The state of the gate of the IGBT is also sent back to the FPGA via a fibre optic transmitter. If the IGBT is ON for too long, in order to avoid the destruction of the resistor in series and the consequent destruction of the converter, the FPGA generates another signal which will turn off all the matrix converter gate drivers. A photograph of the completed overvoltage clamp can be seen in Figure 5.17.

Figure 5.17: Photograph of the clamp circuit

The ability of the clamp circuit to protect the Matrix converter is therefore dictated by the ability of the resistor to dissipate the load energy. High power thick film resistors were not available at a high enough pulse dissipation rating so steel wire wound cement encased resistors were chosen. The load energy that needs to be dissipated during a shutdown increases the temperature of the steel of the resistor. A simple calculation based on the quantity and specific heat capacity of the wire can be used

to determine the suitability.

The continuous power rating of the resistors used dictates the amount of full power commutation errors that can occur before the converter needs to be shut down and hence the robustness and susceptibility of the converter to failures is improved. The rating of the IGBT can be much less than those of the main power devices since only pulses of current are conducted. A 50A IGBT was used in the final implementation which was capable of handling pulsed currents of up to 200A. The lower clamp capacitance reduces the level of inrush current when the converter supply is turned on. The clamp also eliminates problems due to input filter ringing during turn on of the converter.

5.2 Matrix Converter Control Implementation

The control of the matrix converter is implemented using a Digital Signal Processor(DSP)/Field Programmable Gate Array(FPGA) based controller interfaced with a series of circuits which allow information such as gate drive signals and feedback measurement signals to be transferred to and from the controller boards. A more complete description of these circuits will be given in the following sections. A block diagram of the overall control structure implemented is shown in Figure 5.18.

The current, speed and position control loops of the drive system are implemented in the DSP which requires information on the input phase voltages and output phase currents as well as the speed and position feedbacks. The signals are provided by the voltage and current transducers, a resolver and a linear variable differential transformer (LVDT) and are fed to a series of A/D channels on the FPGA board. The digitised information is then transferred to the DSP via the FPGA using the external memory interface. The DSP processes the information and demands the correspondent output voltages to achieve the desired control which is then executed by the FPGA through the appropriate sequence of gate drive signals. The gate drive signals are transferred from the FPGA/Gate drive interface card to the gate drive boards via

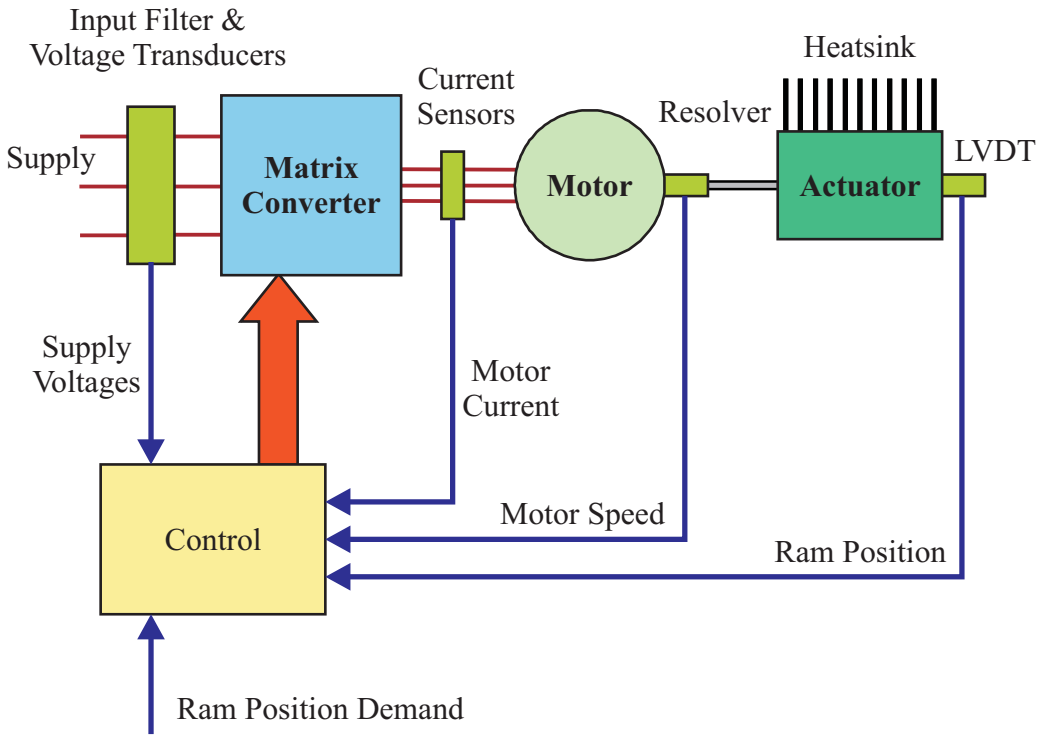

Figure 5.18: Diagram to show the overall cascaded control structure

optical fibres. The following sections will explain in more details the implementation of the control structure at a lower level.

5.2.1 TI-C6711 DSP/FPGA Controller

A fast and effective control of the converter has been achieved by implementing a Texas Instrument C6711 floating point DSP and the DSP Starter Kit (DSK) which, with its on board parallel port, allows the user to fulfil the specific application and connect the controller to a host computer for development and control purposes. The C6711 is a high speed floating point processor which runs at 150MHz and can perform up to eight operations per cycle. One of the major advantages of employing the C6711 DSK is linked to its peripherals and the ability to add external peripherals. Above all the external memory interface (EMIF) which not only supports 16Mb of on board SDRAM memory, Flash ROM, I/O port but also expands the memory interface through an expansion memory interface connector for a daughter board.

The DSP has four dedicated address spaces which allow both the on-board devices and the expansion memory interface to be selected individually without conflict. The expansion memory interface connector is mapped into the DSP's chip enable two (CE2) and chip enable three (CE3) address space. Only one of the two memory space enables (CE2) has been used in this application because only one daughter board was implemented, the FPGA card. All of the accesses to the EMIF are clocked at 100MHz while the CPU is clocked at 150MHz.

The parallel port interface of the DSK incorporates a connection to the host port interface (HPI) of the C6711. The HPI port is a high speed data port which allows a host to access the internal memory of the C6711 without interrupting the central processing unit (CPU) of the DSP. This allows a bi-directional data transfer between the host PC and the DSP to control the converter and download sampled variables. The parallel port interface also provides access to an embedded JTAG emulator for source code debugging.

The FPGA card represents not only a possibility to expand the functionality of the DSP using the memory mapped interface of the FPGA itself, but also provides the DSK with more interface circuitry and allows the analogue to digital (A/D) conversion of all the measured analogue signals. The FPGA card was originally developed by Lee Empringham from the PEMC group of Nottingham University for the TIMES [56] project, and it has demonstrated to be a very flexible and versatile card in many other applications. The board contains a total of 9, 12 bit A/D channels which are employed for this application as follows:

- ×**3** Output currents
- ×**3** Input voltages
- ×**1** LVDT position signal interface
- ×**1** Actuator position demand

It also provides for four D/A conversion channels, hardware comparators for overcurrent protection and digital I/O capabilities for trip information output, trip source inputs, event triggering. A photograph of the FPGA card is shown in Figure 5.19.

The main function of the FPGA is to provide the space vector PWM generator unit and the three state machines (one for each output leg of the matrix converter) to correctly commutate the current between the bidirectional switches depending on the direction of the load current and the demanded switch state. A schematic diagram of the FPGA is shown in Figure 5.20. The FPGA also provides a watchdog timer, trip monitor, trip information interface and temperature sensor interface.

As mentioned previously, the FPGA also provides an interface for the nine serial A/D converter channels. Once the A/D information has been gathered by the interface, it is transferred into registers within the FPGA which are memory mapped to the DSP's memory interface. The trip monitor disables the output of the state machines if any of the hardware or software trips occur. A maximum of sixteen hardware trips and

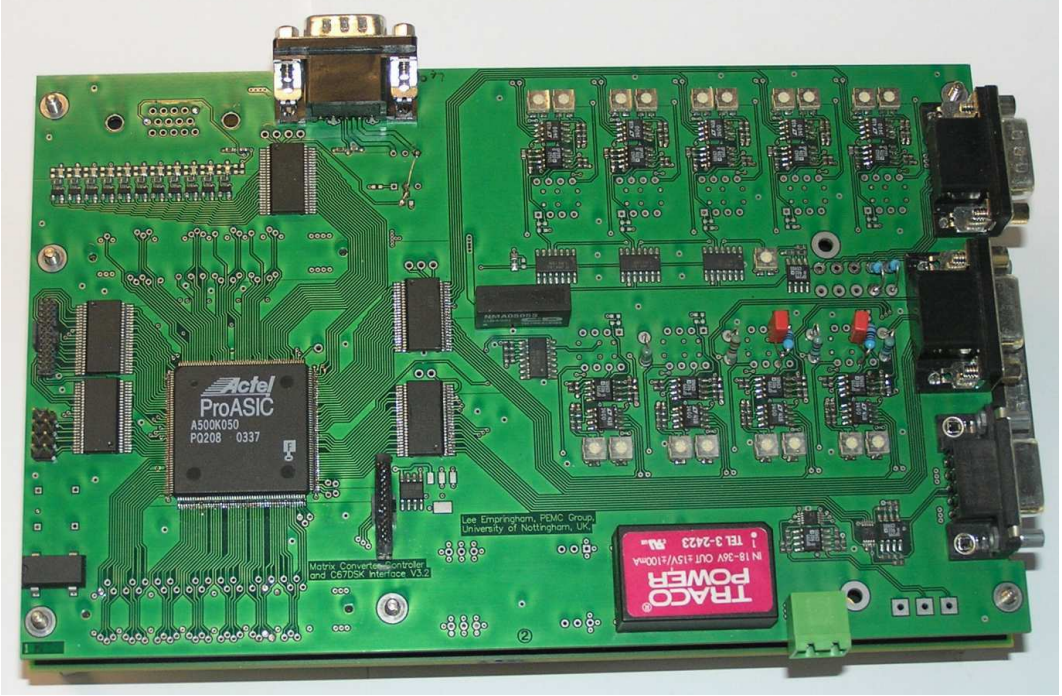

Figure 5.19: Photograph of the FPGA card

sixteen software based trips can be used although not all are used for this application. Table 5.2 shows the trip sources used.

Hardware	Software
Over-current	Instantaneous overcurrent
PWM Fifo Empty	Averaged overcurrent
Watchdog	Loss of supply
Resolver Fail	Motor Over-temperature
Clamp Overvoltage	Converter Over-temperature
Clamp Chopper Fail	
28V Supply Fail	

Table 5.2: Hardware and software trip usage

The output of the watchdog timer feeds directly into the trip monitor. The watchdog timer is serviced at the beginning of each control interrupt. If it is not serviced, for example if the DSP has crashed or is not functioning correctly, a trip will be generated and the converter disabled. The temperature sensor interface is effectively a synchronous serial port for use with the LM70 temperature sensor. The LM70

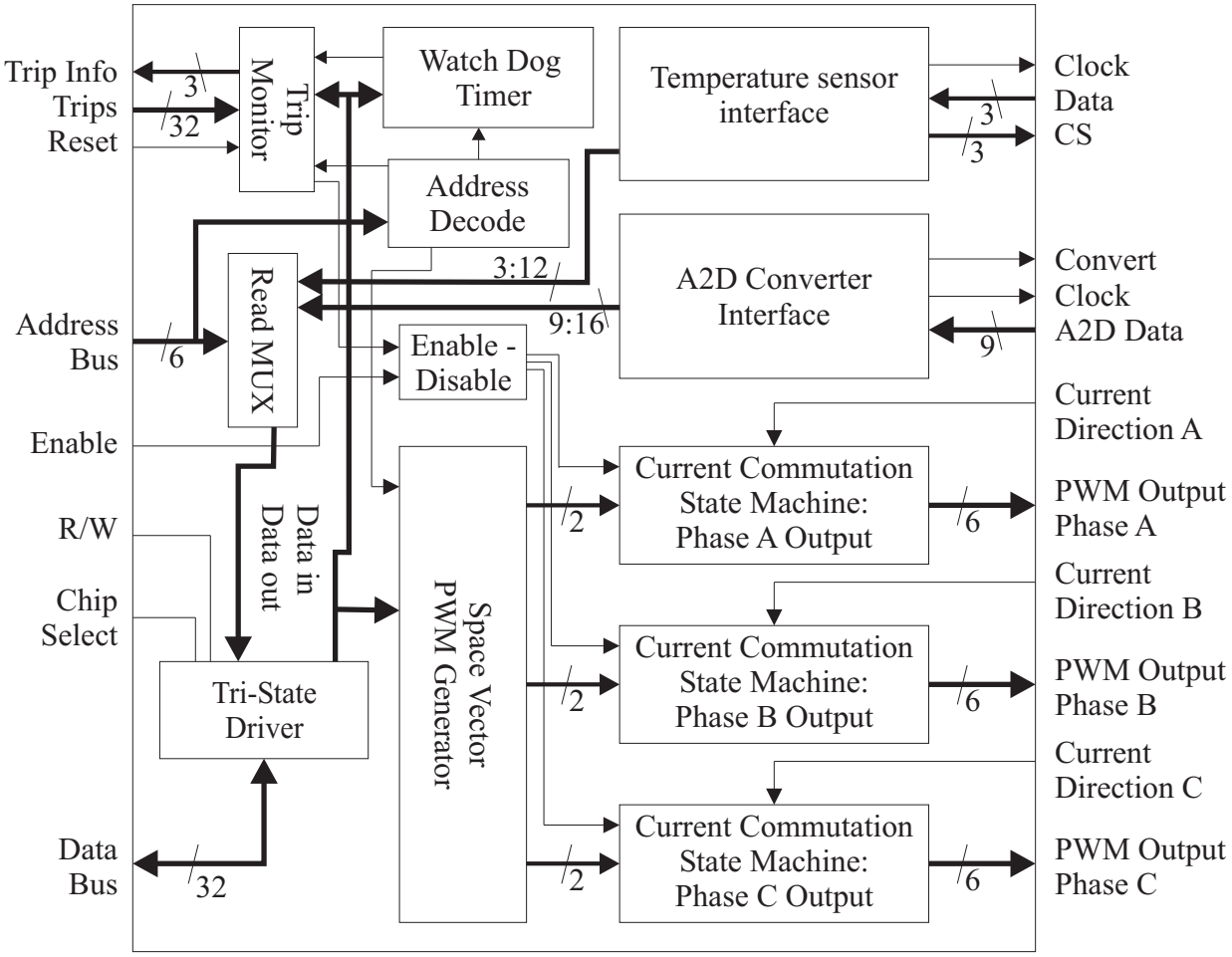

Figure 5.20: FPGA block diagram

contains a temperature sensor, A/D converter and a SPI compatible serial interface. The data from each of the three available temperature interfaces is continually placed in memory mapped registers within the FPGA. The trip information interface will be described in Section 5.2.2.

The source code executed by the DSP to control the matrix converter was originally developed by Maurice Apap from the PEMC group for the TIMES project and modified for this application. Different control parameters were needed due to the different machine implemented and specifications. In the main routine of the source code, after having set all the bits to prepare the external memory interface, FPGA configuration

registers and PWM generator period, the main routine of the DSP enables the PWM interrupt and then waits for the interrupt to occur, after the PWM generator timer is started. The PWM generator functions as the interrupt generator for the DSP. Each time the PWM generator reaches the end of the current period, an interrupt is generated. For this application a PWM sequence time of 80μs was desired and hence the sampling frequency for the system was 12.5kHz.

During the interrupt routine the information from the A/D channels are extracted from the FPGA registers, and manipulated so that the scaled output currents and input line to line voltages are calculated. This information, together with the desired input current angle and the output voltage angle and magnitude is used to calculate the duty cycles implemented in the space vector modulation algorithm. Finally, using the DATA BUS in the FPGA, the space vectors calculated by the DSP are loaded into the appropriate FPGA register to allow it to perform the built in Space Vector PWM Generator. The final sequence of digital signals which will drive the IGBTs is the output of the state machine for each output phase. The state machines require the output of the PWM generator and information about the current direction to perform a 4-step current direction based commutation routine. The calculated vectors will be output during the next PWM period. Figure 5.21 shows a diagram that represents the DSP functions during the interrupt routine. At point **A** the A/D channels are

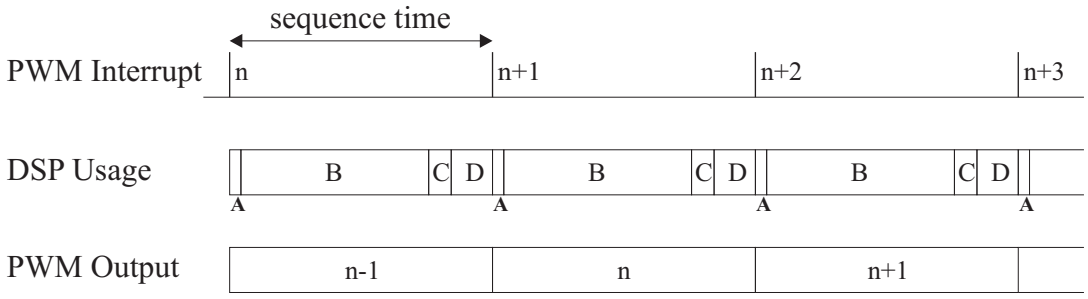

Figure 5.21: Diagram to show PWM interrupt DSP usage

sampled and the data is moved from the FPGA to the DSP. The time period labelled **B** is used to calculate the output PWM vectors and vector times acording to the space

vector control algorithm. The vectors and vector times are then transferred into the PWM generator within the FPGA at point **C**. The time remaining (**D**) before the next interrupt occurs is free to be used for the communication with the host PC. The combination of the characteristics of the high speed DSP and the versatility of the FPGA allows all of the necessary controller functionality to be implemented and the control calculations can be performed at the necessary speed.

5.2.2 FPGA/Gate Drive Interface Card

The interface card between the FPGA board and the gate drive boards is a four layer PCB where the power and ground connections are provided by the internal layers, reducing the stray inductance and increasing the noise immunity. Figure 5.22 shows the top layer of the interface card. The functions of the board are listed below:

- Resolver Interface
- LVDT Interface
- Trip Information Interface
- Gate Driver Fibre Optic Transmitters
- Current Direction Fibre Optic Receivers
- Temperature Sensor Interface

Starting from the right hand side of the board, the interface card supports the DSP/FPGA based controller functions by providing interface circuits for the LVDT (**A** on Figure 5.22) and the Resolver (**B**). Information about the trip signals generated by the FPGA as a consequence of abnormal operating conditions in the converter is presented using light emitting diodes LEDs (**C**). Part **D** provides interface circuitry for three digital temperature sensors which are connected back to the FPGA through a built in serial port. Area **E** shows the fibre optic outputs used to transmit the

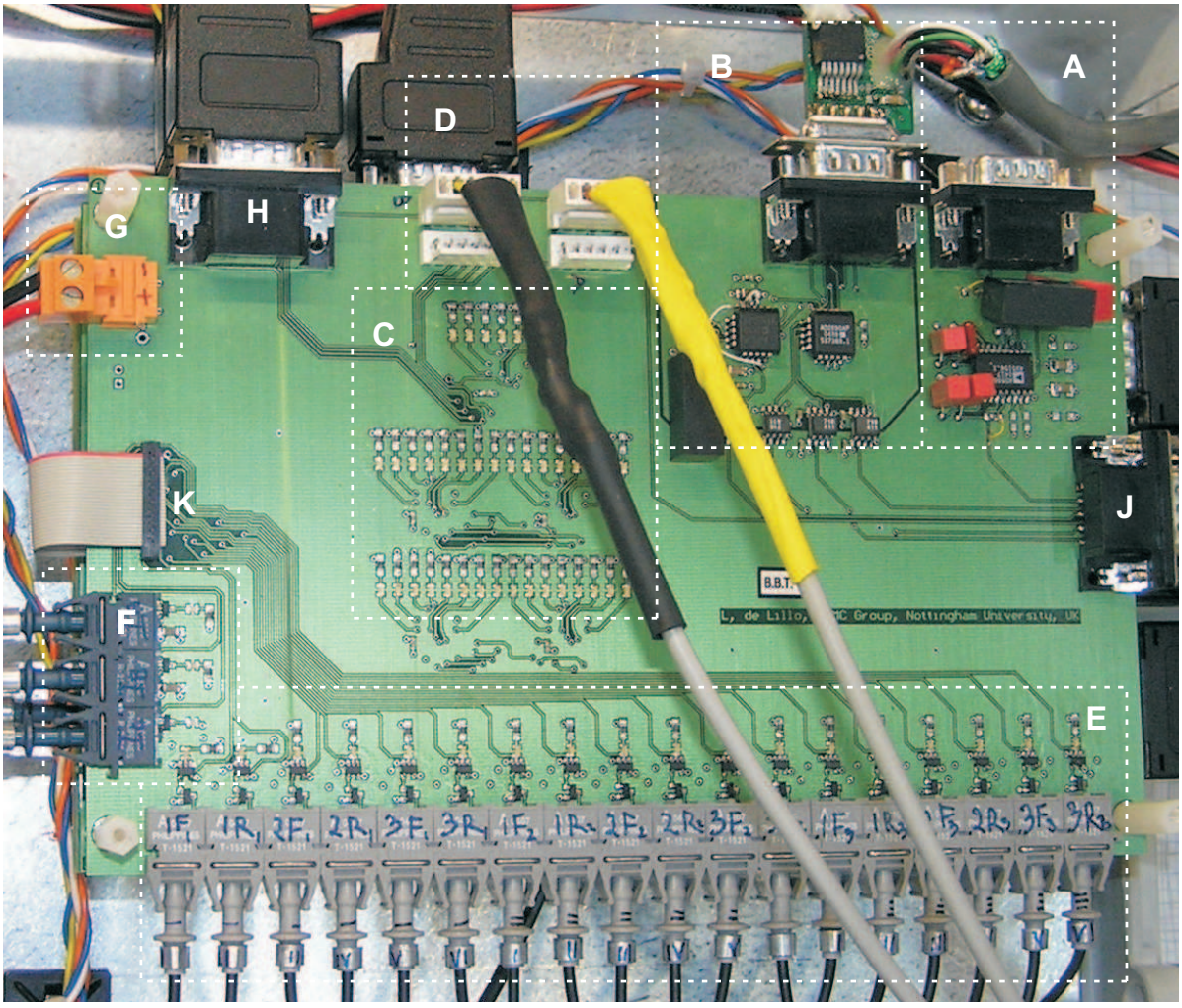

Figure 5.22: Photograph of the interface card

gate drive signals to the gate drive PCBs and fibre optic receivers to transfer the three current direction detection circuit's information to the FPGA is indicated in area **F**. Finally the 5V supply is provided (**G**) for the board and is used to derive the isolated ±5V for the resolver interface circuit and ±15V for the LVDT interface circuit using NEWPORT DC/DC converters. Extra LEDs have been placed close to the fibre optic connectors to indicate activity and therefore provide a visible feedback on the operation of the PWM generation and current direction information.

The LVDT is mounted onto the final test rig, located at Smiths Aerospace laboratories, and provides the conversion of the mechanical position of the actuator into a voltage signal. The LVDT signal conditioner, the Analog Devices AD598, located on the interface card (**A**), provides the sine wave oscillator to drive the LVDT primary coil and uses the two ac signals from the LVDT secondary output to produce an accurate scaled bipolar dc output which will be proportional to the LVDT position. This analog signal is sent to one of the nine A/D channels on the FPGA board through connector **J** on Figure 5.22 to be processed as described in the previous section.

The resolver is mounted onto the motor shaft. It is a rotary transformer which outputs a different ac voltage on each of its secondary windings in accordance with the angular position of the shaft. The type of resolver used in this application requires excitation of the rotor winding with a high frequency ac voltage and outputs sine and cosine voltages from the stator windings proportional to the rotational angle theta. The Analog Devices, AD2S99, is a programmable oscillator which provides the excitation signals for the rotor winding of the resolver. The AD2S90 is a twelve bit resolver to digital converter which operates together with the AD2S99 on the sine and cosine signals of the stator windings to generate an absolute angular position in a digital format (**B**). The AD2S90 uses a serial port to output the digital information. Therefore the digital rotary position of the motor is routed (also using connector **J**) through the FPGA and passed to the DSP using one of its two serial ports (having synchronised the clock of the serial port with the FPGA clock such that the generation of samples occurs at the PWM sampling frequency of 12.5kHz).

Connector **H** provides the digital lines coming from the FPGA for the information to be displayed on the LEDs in part **C**. The information is sent using a data line and two clock lines which are then converted into forty parallel lines by using five, 8-bit serial-in/parallel-out shift registers with output latches mounted beneath the interface card. The output lines from the shift registers are connected to the set of LEDs which are used to visualise the thirty two possible trip signals (sixteen hardware and sixteen software trip signals) and six control signals. (The six control signals are as follows: one LED is used to show the enable signal for each of the state machines, one signal shows the state of the enable switch; one is used to indicate that the PLL which measures the input angle of the supply has locked and one signal is used to indicate when data is being sampled by the DSP for download to the host PC).

Finally, going back to the block diagram which summarises the FPGA functions in Figure 5.20, it can be noticed that an additional serial interface has been implemented to read the data coming from the digital temperature sensors which are provided for the drive system to monitor the temperature of the heat sink, onto which the electronics are mounted, and the temperature of the motor. The information from the digital sensors are transferred to the FPGA through the interface card via the connector **H** in Figure 5.22

5.3 Summary

The design, construction and assembly of the first prototype matrix converter for a large civil aircraft rudder actuator drive system has been described. The final implementation of the actuator drive system did not need to employ all of the potential in terms of the rated power which the matrix converter is capable of delivering. The matrix converter, rated at 36kW, would only be required to deliver 20kW to drive the final motor. A photograph of the completed matrix converter can be seen in Figure 5.23.

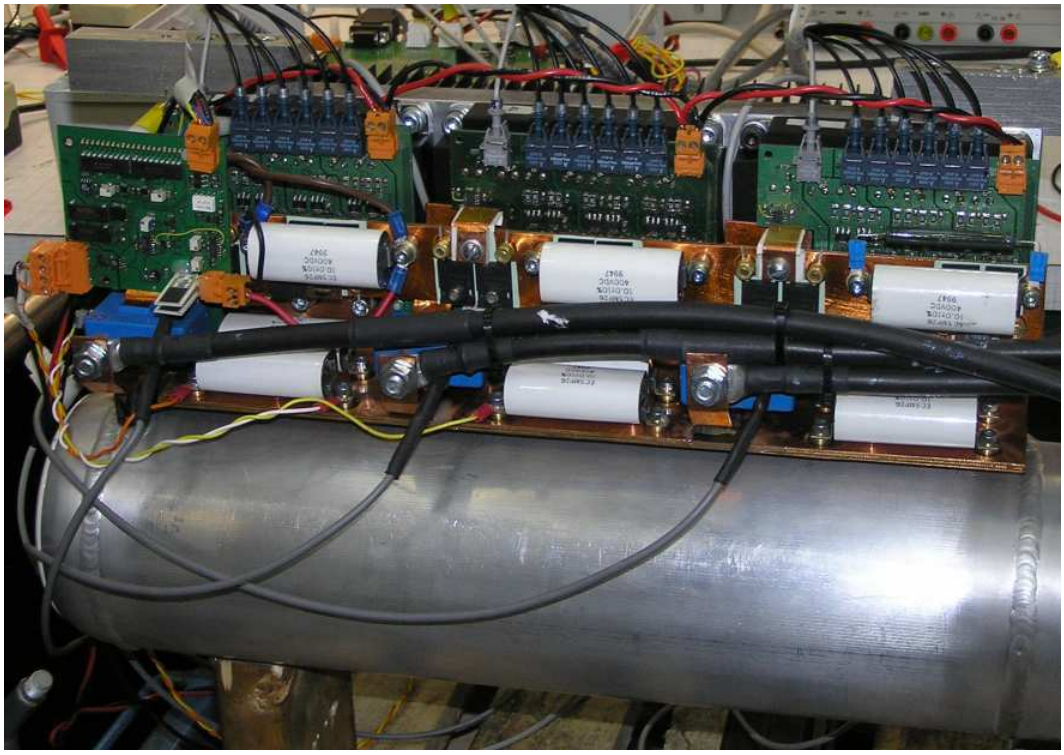

Figure 5.23: Photograph of the finished matrix converter

Chapter 6

EDAAS Drive System Assembly, Testing and Results

The matrix converter for the EDAAS drive system whose construction and assembly has been described in Chapter 5 was submitted to a series of initial tests to verify its functionality. The matrix converter was then used to drive the motor designed for EDAAS before the final assembly and testing of the actuator drive system could be carried out. This Chapter will describe the different testing stages and the results achieved.

6.1 Matrix Converter Drive System

Once the construction and assembly of the prototype matrix converter was completed it was necessary to run a series of tests to verify the power converter performance. Initially a two input phase commutation test was followed by a fixed duty cycle PWM generation test where the commutation of all the three output phases to each of the input phases was tested using a fixed number of output vectors for fixed times. For this test the output of the power converter was connected to an RL load. The output

vectors were arranged such that each output phase would commutate sequentially between input phases A, B and C using different duty cycles for each output phase.

The encouraging results of the initial tests, such as those shown in Figure 6.1, showed that the matrix converter practical implementation and control including the communication and transfer of information between the Host PC, the DSP/FPGA controller, the Interface Card and finally the Gate drive boards were working as expected. The next step was to replace the RL load with a small, 1.5kW motor, and the fixed duty cycle PWM generation, with the appropriate output modulation control.

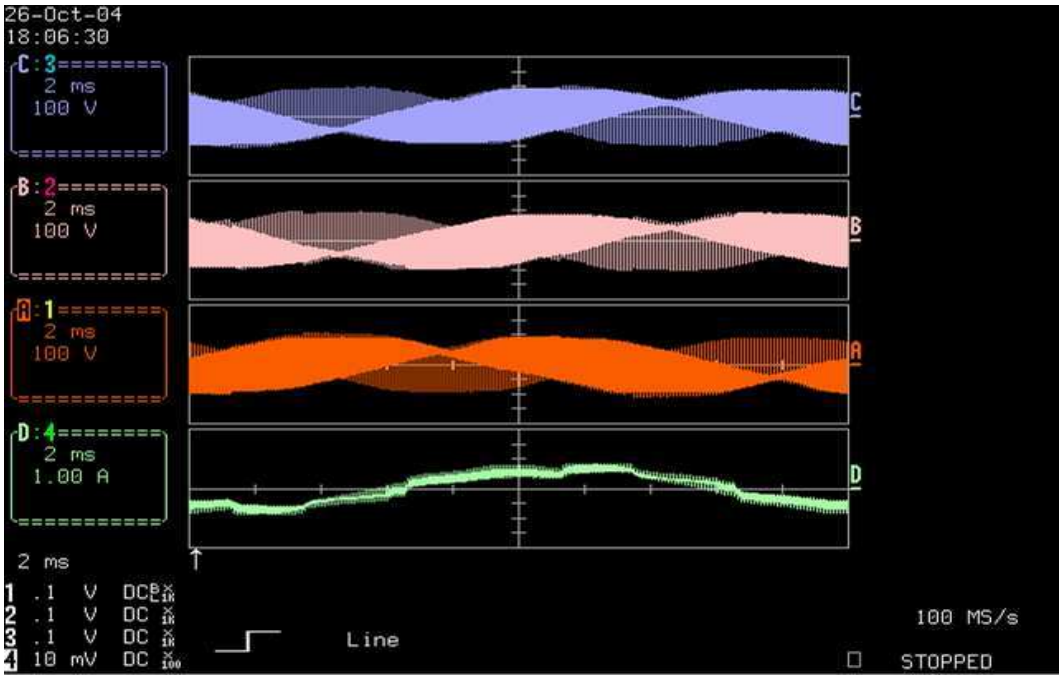

Figure 6.1: Initial test: Output voltages and line current using fixed duty cycles

Initial motor tests were run, first with a 1.5kW induction machine using a constant Volts per Hertz (V/F) control. Tests were then performed with the 3kW Permanent Magnet Synchronous Machine used for the TIMES project using vector based *dq* current control (Figure 6.3) with a cascaded speed controller. In both cases, space vector modulation and four step current commutation for the PWM generation were used. Results of the 3kW PMSM speed reversal from -9600rpm to 9600rpm with a

current limit of 21A during acceleration are shown in Figure 6.2. The input voltage

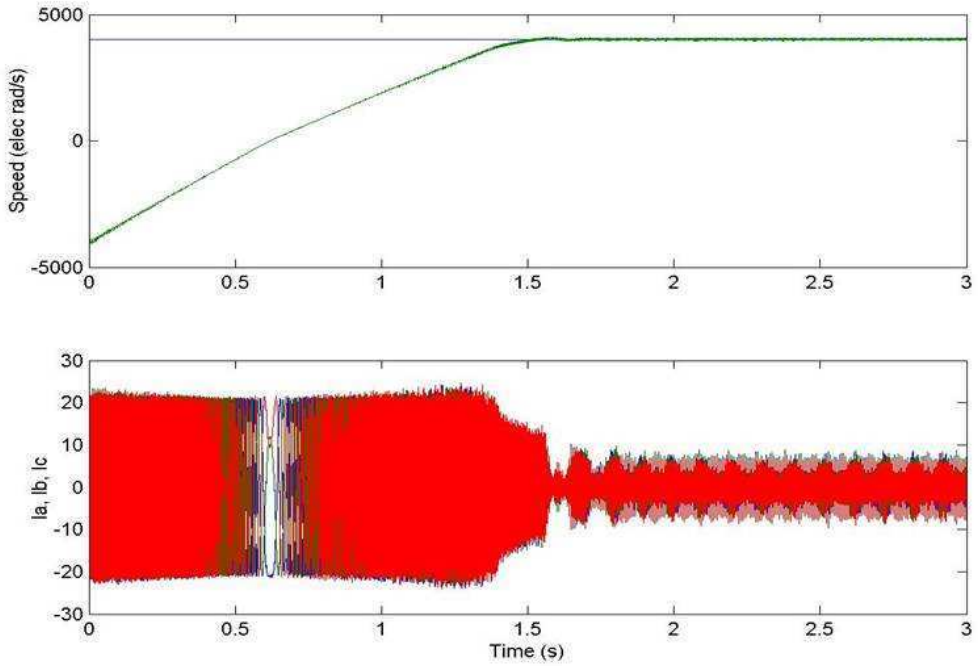

Figure 6.2: Matrix converter driving PMSM from the TIMES project: Speed reversal from -9600 to 9600rpm showing motor line currents

used is the standard aircraft three phase supply of 115V rms, line to neutral.

The code in C language written to implement both the control of the 3kW PMSM and the calculation of the vectors according to the space vector modulation technique as mentioned in Section 5.2.1 needed to be modified and adapted for the EDAAS drive. The host programme used as an interface to communicate between the PC Host (therefore the user) and the DSP/FPGA controller was also modified. The parts which needed to be modified are listed below:

- **DSP Code Changes**
- Motor parameters

- Current controller parameters
- Speed controller parameters
- Position loop parameters
- Id and Iq controllers were separated to have their own controllers (since $Ld \neq Lq$ in the EDAAS motor)
- Limits on current and speed
- A2D converter calibration
- Trip values changed
- The ability to use the resolver angle instead of the LVDT for position feedback was added
- Temperature interface code changed to use the digital temperature sensors

Host Changes

- Limits on current and speed demand as set by the user
- The ability to change the limits using the host was added
- The function to calibrate the absolute rotor angle prior to executing the position control was added

The first tests carried out on the EDAAS drive system were performed by implementing and progressively tuning the current control and speed control of the machine.

6.1.1 Matrix Converter Drive System Control Design Introductory Considerations

To achieve either the *dq* current control or the speed control, a resolver was required to continuously generate the rotor position feedback with respect to the d-axis of the

rotor. In order to be able to operate on an accurate measurement of the rotor position with respect to the d-axis, the offset between the resolver's reading and the actual position of the d-axis needed to be calculated. This was achieved by demanding a small current at zero degrees with respect to the stator. The rotor d-axis then moves to align itself to the imposed stator flux. The resolver reading at this point is the offset between the resolver reading and the d-axis of the resolver. To gain a more accurate reading, the angle of the injected current was altered around 0° to move the rotor to the zero position from both directions. The reading of the resolver at the 0° position was then recorded again. An averaged offset value from the 0° of the d-axis was therefore found.

The dynamic equations of the PMSM in the *dq* reference frame are shown in equations 6.1 and 6.2:

$$v_d = Ri_d + L_d\frac{i_d}{dt} - \omega_r L_q i_q \tag{6.1}$$

$$v_q = Ri_q + L_q\frac{i_q}{dt} + \omega_r L_d i_d + \omega_r \Psi_{rd} \tag{6.2}$$

where v_d and v_q are the components of the stator voltages, R is the winding resistance per phase, L_d and L_q are the stator inductances, ω_r is the rotor electrical angular frequency and Ψ_{rd} is the magnitude of the stator flux linkage due to the rotor flux. We will refer to the terms $-\omega_r L_q i_q$ and $+\omega_r L_d i_d$ as the back-EMF voltage terms. The general block diagram which includes the cascaded current and speed control loops of the EDAAS salient PMSM is shown in Figure 6.3. The speed control loop generates the demanded torque T^* which is processed to generate the demanded i_q^* and i_d^* for the inner current control loop. The back-EMF voltage terms are added to the output voltages of the current controllers to generate the desired output voltages $v_q^*$and v_d^* for the matrix converter. The difference in the control scheme of the salient and non-salient PMSM machine will be discussed in the next section.

The approach adopted to design the cascaded position (see Section 6.2.1), speed and current control loops was to analyse their dynamic response to a step input. This was done by determining for each control loop, the equivalent closed loop transfer function in the s-domain whose parameters depend on those of the plant transfer

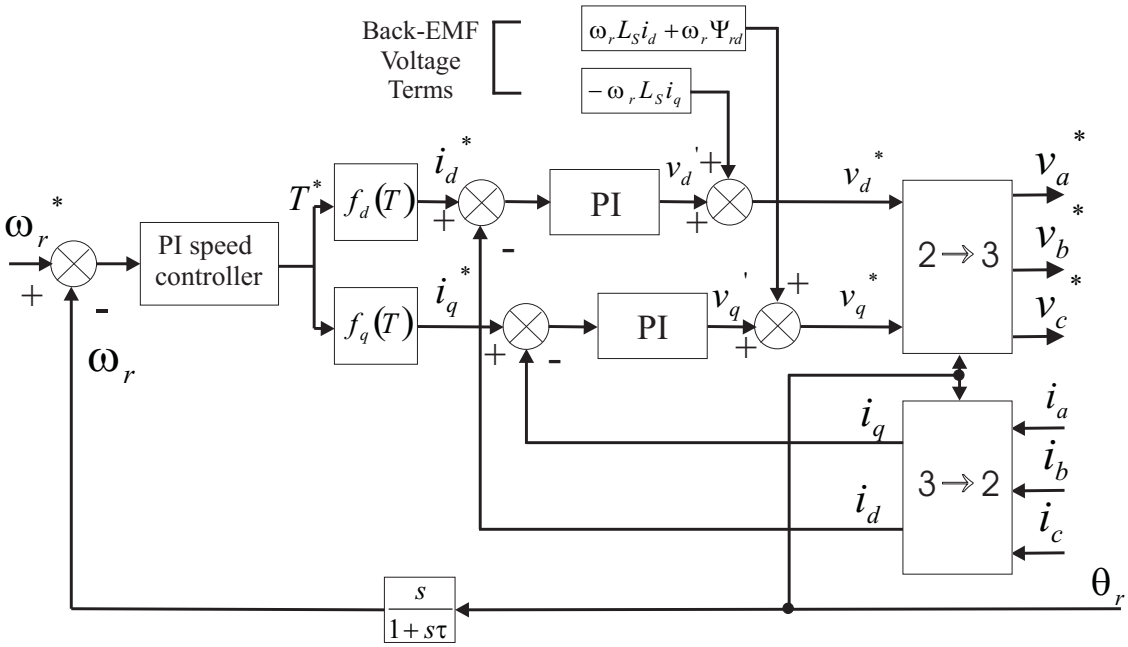

Figure 6.3: General speed control structure for the salient PMSM

function related to the system, which are known, and of those of the controller transfer function, which are unknown and need to be implemented. The resulting closed loop transfer functions are of a second order system for the speed and current control loops and it has the general expression as a function of the natural frequency, ω_n, and damping ratio, ζ, given as follows:

$$\frac{K}{s^2 + 2\zeta\omega_n s + \omega_n^2}$$

or of the first order system such as for the position control loop, in which case it would have the following general expression:

$$\frac{K}{Ts + 1}$$

where T is the time constant of the system, which determines the system speed of response.

The controller parameters for the different control structures have been determined by considering the project specification which required a bandwidth of between 2 and

3Hz for the most external control loop, the position control loop. On the basis of this specification, in order to be able to decouple the control loops of the cascaded control structure from each other, the bandwidth of the inner loops are chosen to be a factor of 10 higher progressively. This is also justified by the fact that the mechanical system is certainly characterized by higher time constants then the electrical system which therefore require the highest controller bandwidth. More details on how the controller parameters have been determined are given in the following sections as each of the control structures are discussed.

6.1.2 EDAAS Matrix Converter Drive System Current Control

The rotor saliency of the PMSM machine designed for EDAAS makes its torque dependent on both the "magnetic" and "reluctance" torque components as defined in section 4.2.1. This implies that the control of the torque is achieved by not only controlling i_q but also i_d, assuming once again a dq frame vector control for the machine control [54]. From the equation (4.2) it is also evident that the reluctance component of the torque depends on the difference $(L_d - Lq)$ which is a negative value since $L_q > L_d$ and therefore i_q and i_d must have opposite sign to be able to give a positive contribution to the torque. In order to implement a working current control which could operate on both the torque components, it was decided to progress gradually and design first a current control of the machine as if it was a non-salient surface magnet PMAC machine ($L_q = L_d$) and then to include the control of i_d. In the first case, it is only required that i_q is controlled while the i_d demand is kept to zero in order to achieve the maximum torque-per-amp unless flux weakening operation is required.

Given the motor parameters such as the stator inductances and the winding resistance per phase, the general block diagram for the current control loop is shown in Figure 6.4.

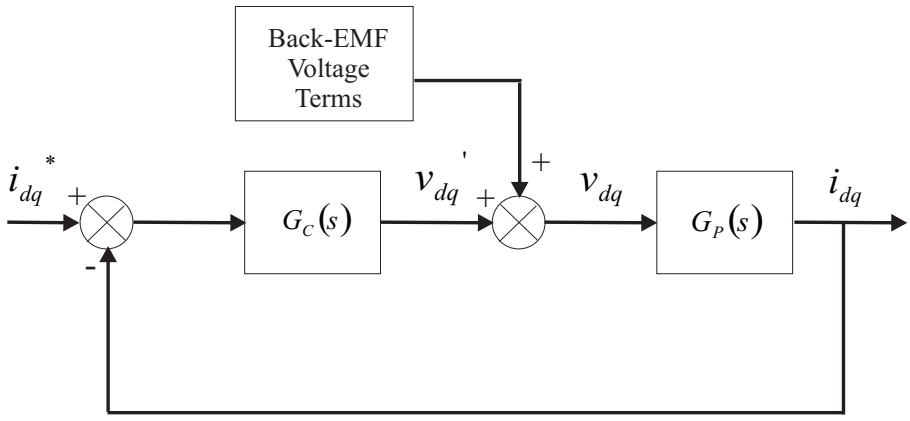

Figure 6.4: Block diagram of the current controller

where the plant electrical transfer function is given as follows:

$$G_P(s) = \frac{\frac{1}{L}}{s + \frac{R}{L}}$$

A PI controller was chosen and its transfer function has the general expression given as follows:

$$G_C(s) = K_P + \frac{K_I}{s}$$

where K_P and K_I are the proportional and integral constants, respectively.

First it is assumed that there is no rotor saliency, which implies that $L_q = L_d$. Also, having been given the specification of 2 or 3Hz for the bandwidth of the position control loop, the bandwidth of the current control loop will be chosen two orders of magnitude higher, for the reason mentioned earlier in Section 6.1.1. A range of natural frequency values between 200Hz-300Hz and damping ratio values between 0.8 and 0.9 were tested to design the best PI controller for the current control loop. These specifications correspond to a specific behaviour of the system to a step response. It is clear that the equivalent closed loop transfer function is one of a second order system whose general expression has been given earlier in Section 6.1.1. By equating the denominator of the closed loop transfer functions and imposing the specifications chosen for ω_n and ζ, it is possible to determine the control parameters K_P and K_I.

Therefore the current controller transfer function resulted in the following expression:

$$G_C(s) = 2.17 + \frac{2.3 * 10^3}{s}$$

For the equivalent current controller defined in the z-domain, the sampling frequency f_s should be chosen so that $f_s >> f_n$, where f_n is the natural frequency and the highest frequency in control structure. A high enough sampling frequency will guarantee a more accurate representation of the continuous system. Therefore a sampling frequency of 12.5kHz was considered for the current control loop.

The search for the optimum PI current controller revealed an inconsistency between the designed stator inductance L_q and the real one. In particular Figure 6.5 shows a comparison of the experimental i_q and v_q behaviours having assumed the same PI controller characteristics but different values of L_q. The overshoot in i_q disappears when doubling the value of the designed parameter L_q.

When rotor saliency is considered ($L_q \neq L_d$) both i_q and i_d references are changed in order to have the best performance in terms of machine torque generation. A first not quite rigorous attempt to control the dq current components was to use details from the design of the machine that could help to extrapolate information on the relation between i_q and i_d. This has been possible by using the map of the maximum torque expressed as a function of i_q and i_d obtained from a design simulation run on the machine and is shown in Figure 6.6. The aim was to demand a positive i_q while controlling i_d to be negative in correspondence of the maximum torque per amp condition (in this way, all injected current would produce torque). A linear interpolation was performed on the data available to calculate the relationship between the dq current components. The overall current control of the salient PMSM was tested on the drive experimentally and results are shown in Figure 6.7 and shows the d-axis and q-axis currents during a speed reversal of the motor from -4000 to 4000rpm.

A more rigorous approach would require further tests on the machine itself to experimentally find the curves of i_q and i_d for the maximum torque per amp condition.

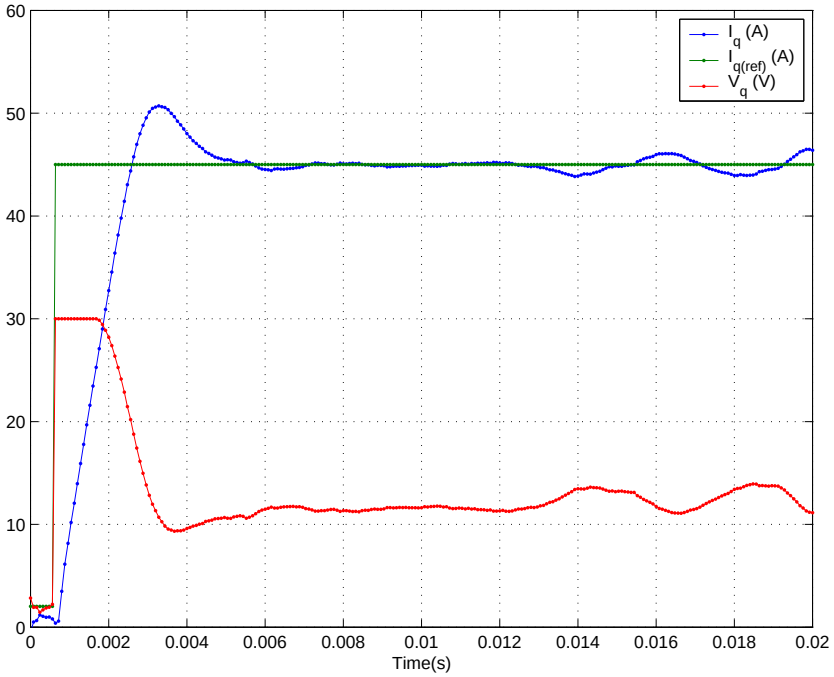

(a) Response where L_q is equal to the simulated value

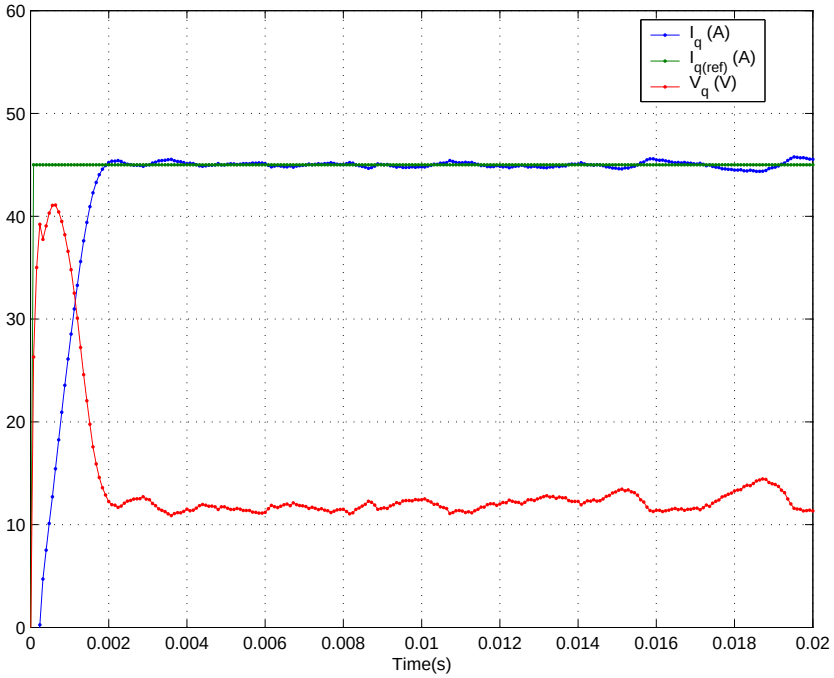

(b) Response when L_q is doubled

Figure 6.5: Current controller response for different values of L_q

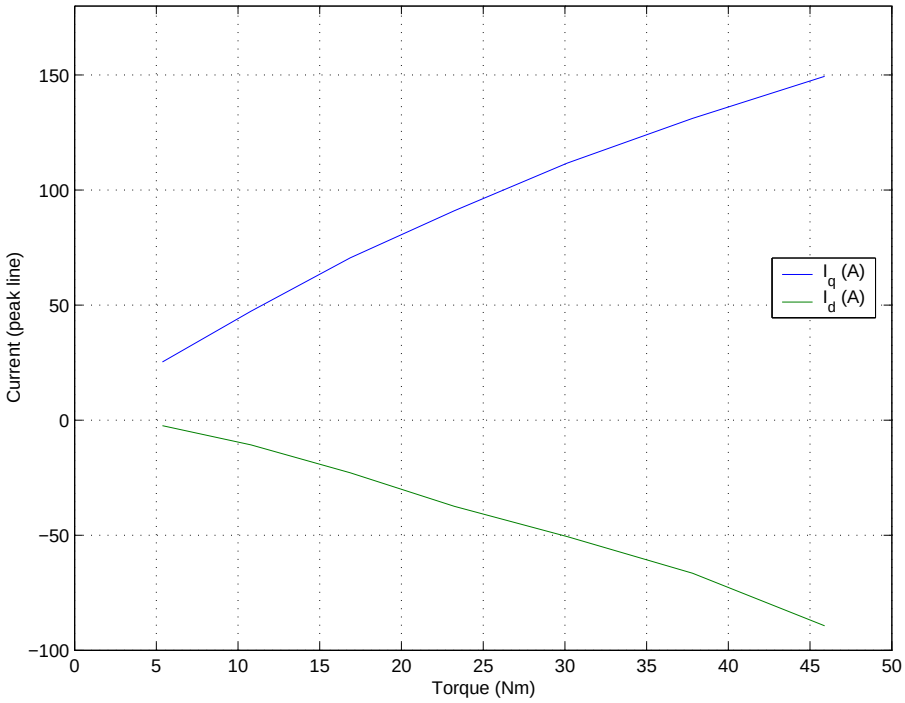

Figure 6.6: Graph to show relationship between Id,Iq and torque of the machine at 4500rpm

Look-up tables could then be built as indicated by $f_{d,q}(T)$ in Figure 6.3, which, for a given value of torque, generate the required demand values of i_q and i_d for the maximum torque per amp condition. Due to restrictions imposed by the time available to complete the project and deliver a reliable and working matrix converter drive for an aircraft actuator, the current control of the actual machine with its rotor saliency properties was not further investigated. It was decided therefore for the final implementation, to treat the machine as a non-salient PMSM and to postpone, for future work, the possibility of exploring the best way to increase the maximum machine torque.

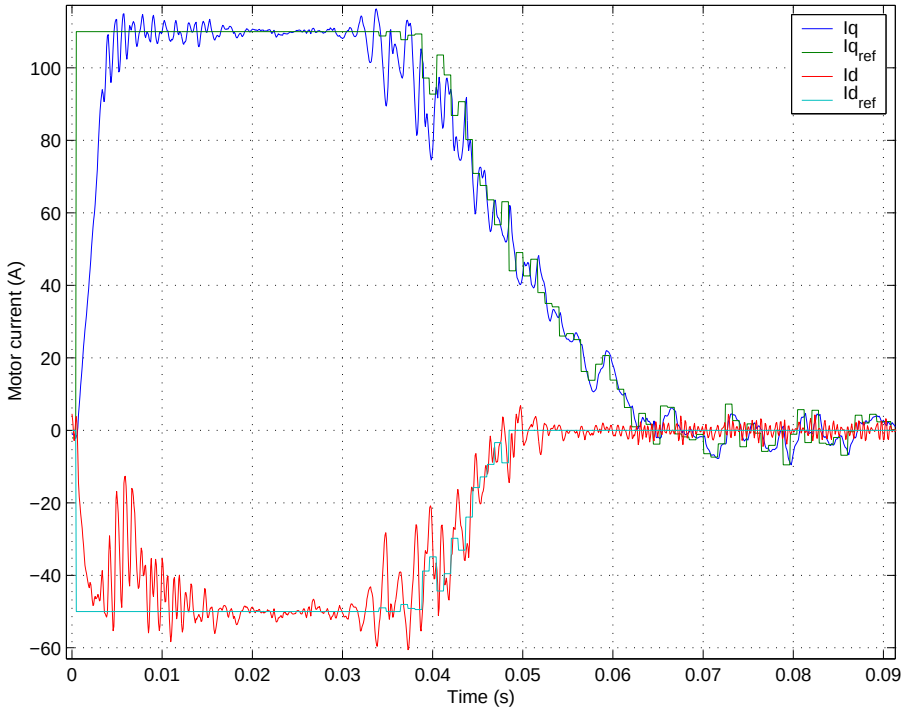

Figure 6.7: Control of i_d and i_d during a motor speed reversal from -4000rpm to 4000rpm

6.1.3 EDAAS Matrix Converter Drive System Speed Control Design

Assuming no mechanical load is attached to the machine, Newton's equation of rotational motion is given in (6.3)

$$T = J\,\frac{d\omega_{mech}}{dt} + B\,\omega_{mech} \tag{6.3}$$

where T is the torque developed by the interaction of the magnetic fields generated by the rotor permanent magnet and stator winding currents, ω_{mech} is the rotor mechanical angular frequency, J is the rotor inertia and B is the viscous damping friction on the motor shaft. The design of the speed controller was performed once the values of the motor parameters such as J and B were calculated from experimental results.

The rotor inertia J was determined by analysing the motor speed behaviour during a speed reversal. The value of i_q was used to calculate the torque while the motor was accelerating to the demanded speed. During the speed transient, near zero speed, the effect of B on the motor torque is minimised and the only real opposing torque is due to the inertia of the machine. The equation (6.3) can therefore be simplified by ignoring the friction on the motor shaft and the value of J can be easily found. From the curve of i_q for maximum torque per amp condition of Figure 6.6, it is possible to find the correspondent value of torque, and if relatively low (20A) values of i_q are used, i_d has little contribution to generated torque, while from observation of the speed transient $\frac{\Delta\omega}{\Delta t}$ can be calculated .

The viscous damping friction B was determined by examining the drive at steady state, when the demanded speed was reached. In this case the rotor inertia has been overcome and the motor torque is dependant on B. Again it is possible to consider a simplification of the equation (6.3) and to evaluate B knowing the values of ω_{mech} and T. After analysing the behaviour of the current i_q and determining its average value at steady state, a value of the torque constant k_T can be determined from the curve of torque constant k_T versus line current shown in Figure 6.8. The value of i_q found at steady state was quite low therefore the torque generated by the machine

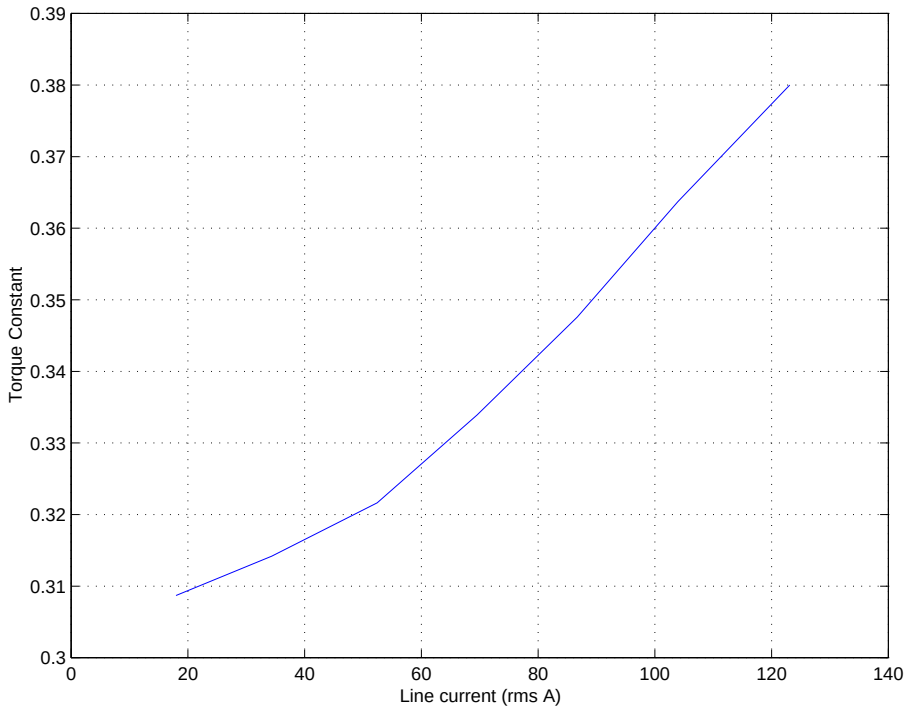

Figure 6.8: Graph to show relationship between rms line current and torque constant of the machine

in this condition can be assumed to be influenced only by the q component of the current. From the expression of T in terms of torque constant, $T = k_T i_q$, the value of T at steady state is found. Figure 6.9 shows the general block diagram for the speed control loop.

Having found the motor parameters J and B, the plant transfer function for the speed control loop of Figure 6.9 is given as follows:

$$G_P(s) = \frac{\frac{1}{J}}{s + \frac{B}{J}}$$

A PI controller was also chosen for the speed control loop, which is characterised by the same general transfer function described in the previous section, as a function of the control parameters K_P and K_I. For the design of the controller, the natural frequency was chosen an order of magnitude higher then the one of the position

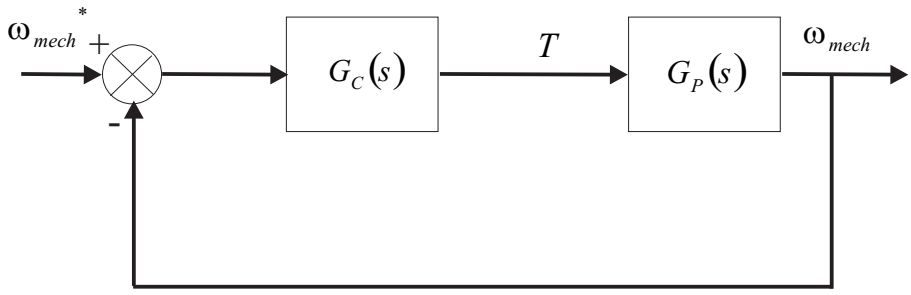

Figure 6.9: Block diagram of the speed controller

control loop, which meant a value around 20Hz, while for the damping factor a value of 0.8 was chosen. Following the same approach adopted for the design of the current controller, the specifications chosen are imposed on the second order system step response. The speed controller parameters are therefore found and the controller transfer function given is the following

$$G_C(s) = 0.4857 + \frac{38.58}{s}$$

Moving to the z-domain, a sampling frequency needs to be chosen. In this case the sampling frequency is the result of a compromise between the accuracy of the system representation and the resolution of the resolver speed measurement. Again empirically a sampling frequency of 1.25kHz was chosen and which lead to a sampling period of $800\mu s$.

The speed control, implemented and tested, was achieved with a small (but acceptable) overshoot as can be seen from the results shown in Figure 6.10 of a speed reversal between -4000rpm and +4000rpm whit a limit on the i_q current of 100A.

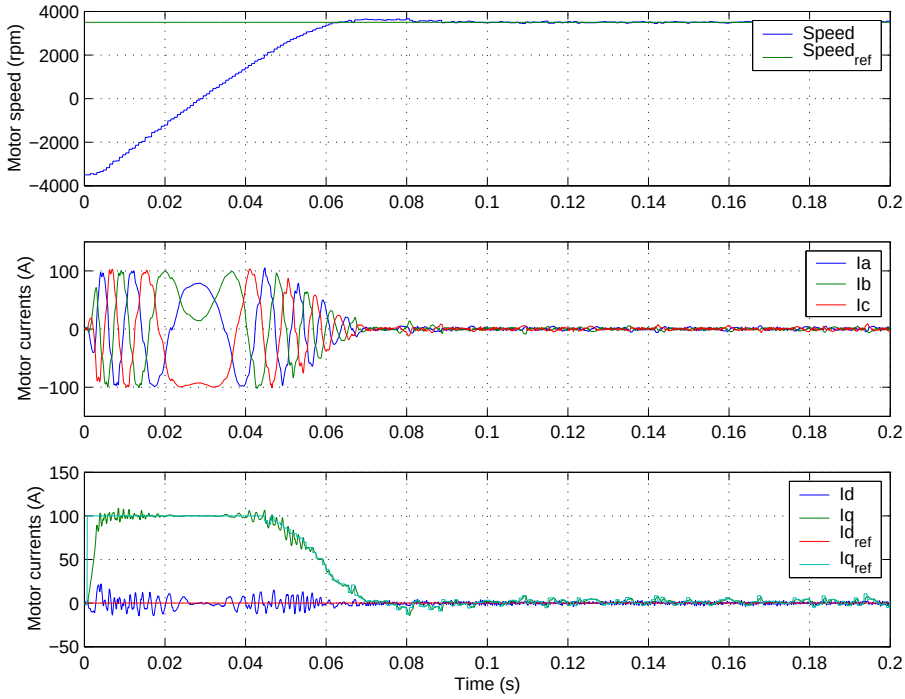

Figure 6.10: Speed reversal between -4000rpm and +4000rpm, with a limit on the motor phase current magnitude of 100A

6.2 EMA Drive System

The individual parts of the EDAAS matrix converter drive system described in the previous section were dismantled (the motor, the power converter and the temporary heat sink) to proceed to the assembly and testing of the Electro-Mechanical drive. Figure 6.11 shows the Electro-Mechanical Actuator drive system in our laboratory.

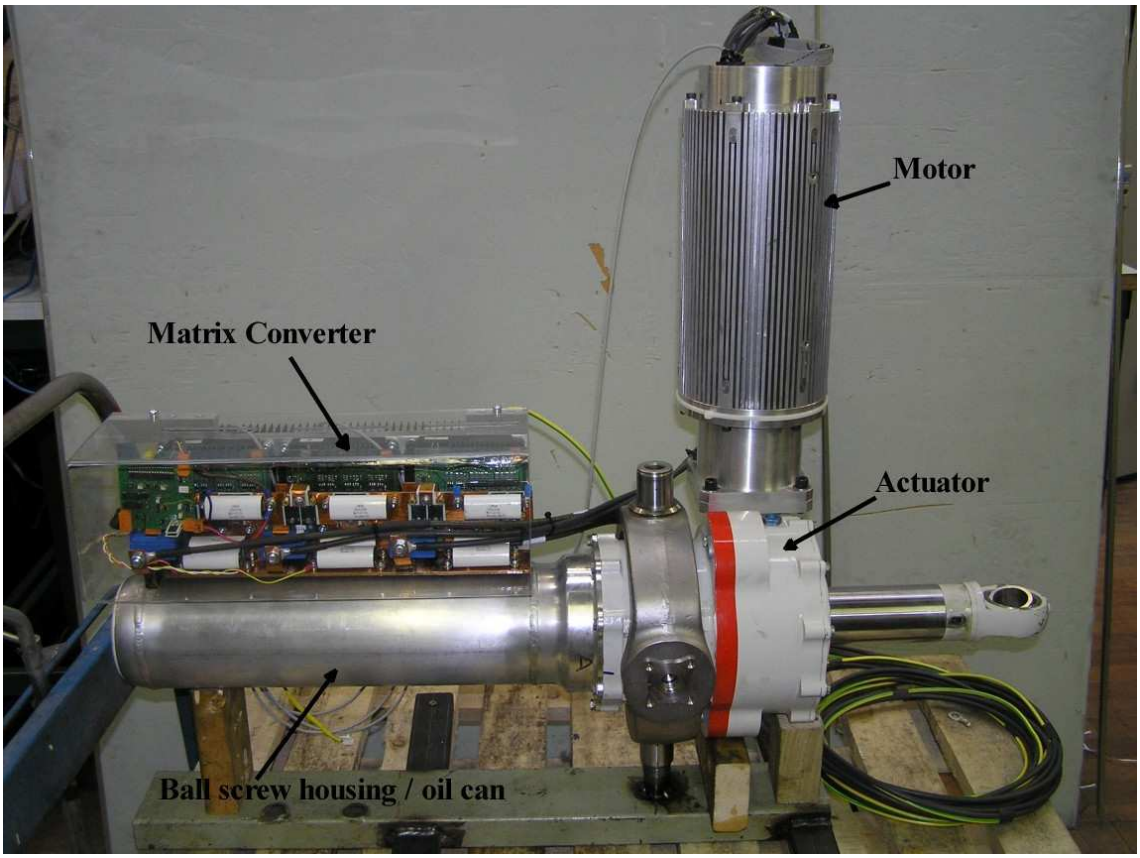

Figure 6.11: Photograph of the matrix converter based actuator at Nottingham

The compact design of the matrix converter with its protection circuit fits well within the space available over the oil can of the actuator. The matrix converter is mounted onto the heat sink which was designed by our colleagues in the School of Mechanical Engineering, who carried out the thermal analysis of the drive system under all operating conditions. The original actuator's oil can was replaced with another one

which incorporates the heat sink for the power electronics. It was manufactured by the mechanical engineering workshop from one solid piece of aluminium, milling out the fins for the heat sink. A thermal image of the heat sink under test is shown in Figure 5.3. Cable connections were provided from the output of the converter to the motor standing vertically in the picture which is attached to the actuator through the worm-wheel/ball-screw. The design of the PMS machine was carried out by other colleagues from the PEMC group involved in this project and manufactured by our workshop.

Once the assembly of the EMA drive system was completed, before connecting the power converter to the motor, an RL load attached to the output of the power converter was used to repeat the basic functional tests mentioned previously, such as the fixed duty cycle PWM generation test. This was necessary in order to check that all of the connections in the matrix converter were correct and that none of the circuitry was damaged during the re-assembly process. After re-establishing the connection between the output of the matrix converter and the machine which is now loaded with the actuator. The total inertia and viscous damping friction on the motor shaft needed to be re-calculated in order to achieve a high-performance motion control. New values of J and B were found using the techniques outlined in Section 6.1.3 and the speed control loop redesigned.

Once the actuator-drive system had been assembled, and the speed control loop re-tuned, the outer-most control loop of the three control loops, the position control loop, could be developed.

6.2.1 EMA Drive System Position Control

The actuator's gearbox uses a worm-wheel with the output gear directly driving the nut of the ballscrew which has a maximum extension of 217.5mm and is shown in Figure 6.12. The actuator translation to rotor angle ratio is a constant value of $0.14865\frac{mm}{rad}$ and it will be considered when defining the plant transfer function of the

position control loop.

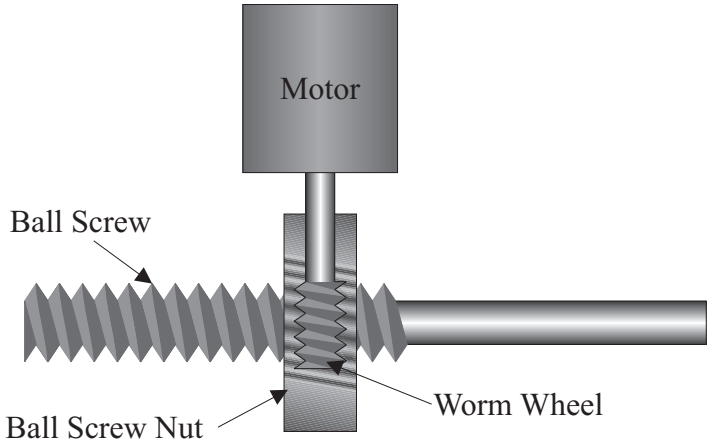

Figure 6.12: Diagram of the gear box structure of the actuator, showing the ballscrew, nut and wormwheel

The actuator originally considered for this project was characterised by a maximum ballscrew extension speed of $160\frac{mm}{rad}$ which in terms of motor speed employing the translation to rotor angle ratio is equivalent to a motor speed of approximately $10000rpm$, the machine maximum desired speed. The actuator that was actually employed was a different one from that which was originally specified and its maximum input speed was rated at $5000rpm$.

The general block diagram for the position control of the EDAAS EMA drive system is shown in Figure 6.13 To achieve the position control of the EMA drive system the demanded position Pos^*, which can be either an analog input demand or a demand from the Host-PC, is used to generate the desired motor speed which is processed as described in section 6.1 for the block diagram in Figure 6.3.

In order to gather on line information on the linear extension of the actuator, and to perform the position control loop, a feedback signal coming from the LVDT sensor is required. Unfortunately the LVDT sensor was mounted on the test rig, located at the Smiths Aerospace laboratory, which meant that the LVDT interface circuitry described in Section 5.2.2 could not be tested in our lab and that the information

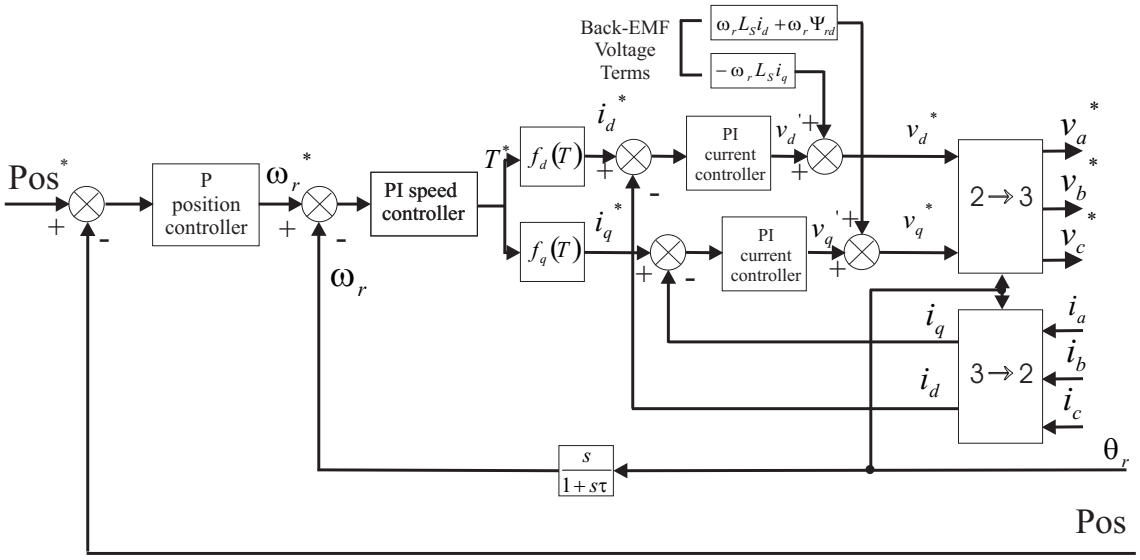

Figure 6.13: Structure of the position, speed and current control of the drive system

on the linear extension of the actuator needed to be obtained differently. Since the linear extension of the ram is directly proportional to the absolute rotor angle, this information could be used to determine the ram position. Since the DSP could not know the angle of the motor at start up in terms of linear ram position, the initial rotor angle had first to be determined.

It has been mentioned earlier that the maximum extension of the actuator ballscrew is 217.5mm and the 0mm position (zero position) is assumed to be half way through the total extension. A positive demand from the position control will make the ballscrew extend further and a negative position demand will make the ballscrew withdraw. By demanding a very low speed in the order of $100rpm$ in the negative direction and limiting the current i_q to a low value of $10A$, the ballscrew is allowed to slowly withdraw completely until the endstop is reached. In this way it is possible to know in mm the precise initial position of the balscrew (since the position of the end stop is known) and at the same time, from the actuator translation to rotor angle ratio, the initial value of the rotor angle. The rotor angle is determined only once to initialise the drive and a position control is achievable with a high accuracy while the LVDT feedback is temporary not available. The position loop block diagram is shown in

Figure 6.14.

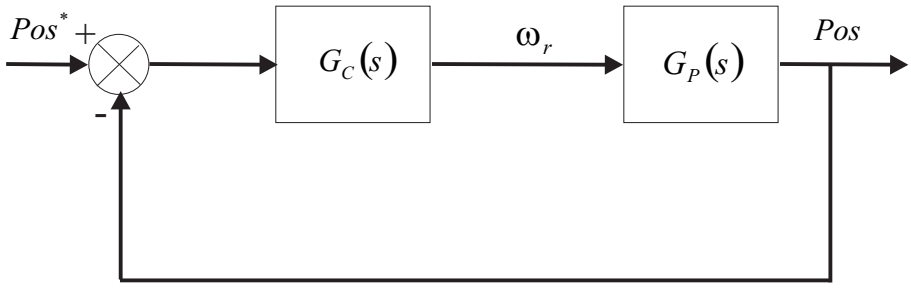

Figure 6.14: Block diagram of the position controller

The position control loop plant transfer function $G_P(s)$ in Figure 6.14 links the linear extension of the actuator at the output with the rotational speed of the motor on the input and it is given, while also taking into account the actuator translation to rotor angle ratio, as follows:

$$G_P(s) = \frac{0.14865\frac{mm}{rad}}{s}$$

The design of the position controller was done by considering only a proportional gain K_p and the specification given of a bandwidth of 3Hz. In this case the closed loop transfer function is the one of a first order system whose general expression has been given in section 6.1.1. Imposing the specification of a natural frequency of 3Hz on the system time constant, which will correspond to a specific system speed response to a step input, the controller proportional constant will result in $K_P = 127$. With regards to the choice of the sampling frequency for the position control loop, again the empiric rule $f_s >> f_n$, should be followed for reason of accuracy of the representation of the continuous system in the discrete domain.

The position control loop was implemented and tested and results are shown in Figure 6.15. A step in the position demand from -20mm to +20mm is required. The machine accelerates to the maximum speed of 5000rpm while getting to the demanded position and it slows down to zero as it approaches the final position. At the same time a maximum i_q current of 135A is employed to develop a torque capable of accelerating the machine to the above mentioned maximum speed. Once the maximum

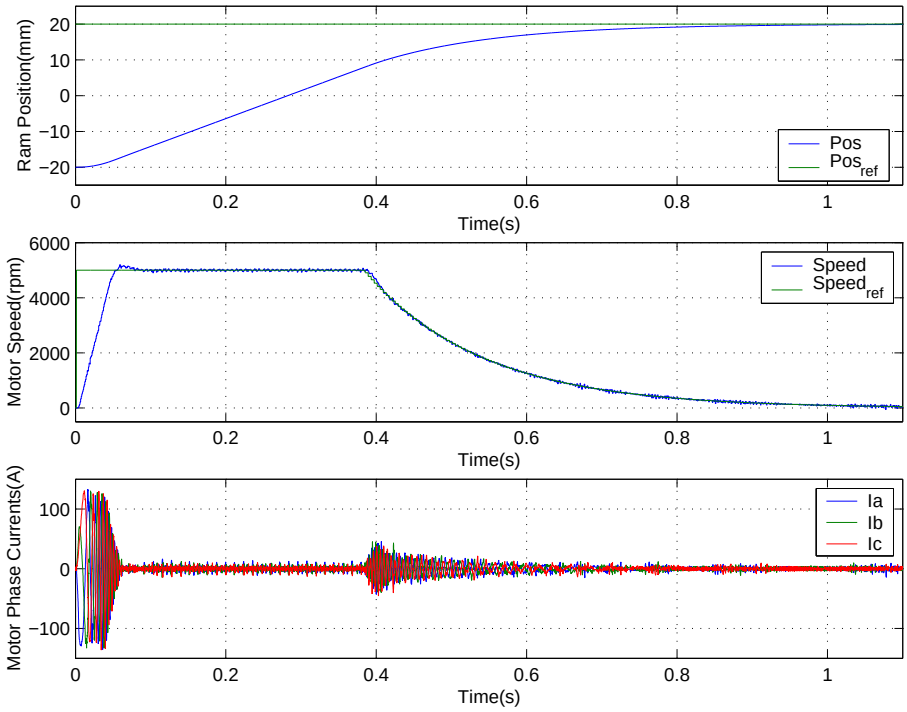

Figure 6.15: Step in the position demand from -20mm to +20mm with a maximum i_q of 135A and maximum speed of 5000rpm

speed has been achieved the torque producing current i_q reduces to a minimum level which is enough to overcome the viscous damping friction of the system.

6.3 EMA Drive System at Smiths Aerospace Research Laboratory in Wolverhampton

After having completed the initial stage of tests on the EMA drive system carried out in our laboratory, with no translational load applied to the actuator, the assembled system was ready to be moved to the Smiths Aerospace research laboratory at Wolverhampton. Here the EMA drive system was mounted on to the test rig, manufactured to the specifications and the research purposes of the EDAAS project.

The test rig includes a hydraulic ram which can be programmed to provide the appropriate loading action on the actuator according to standard flight conditions or specific test conditions. Its schematic is shown in Figure 6.16 which gives a top view and a 3D-side view of the test rig. As highlighted in the schematic, the dark grey area represents the EMA drive system which has been described so far.

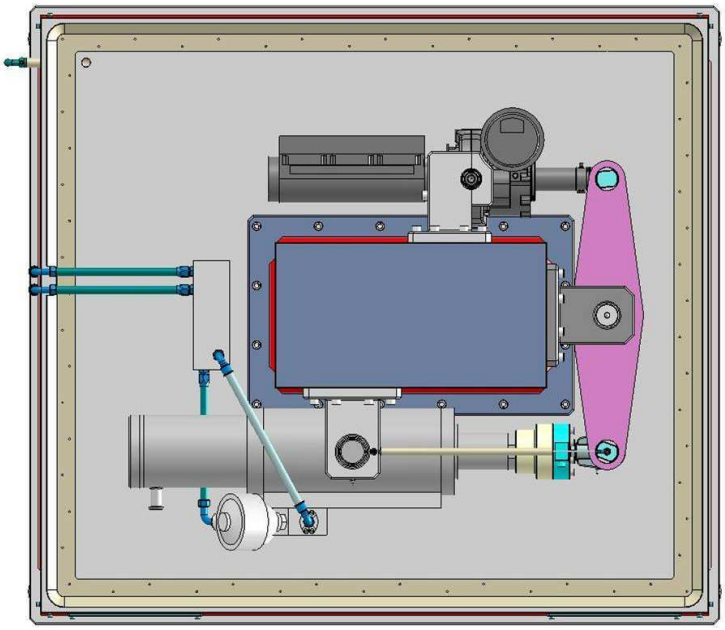

(a) Top View

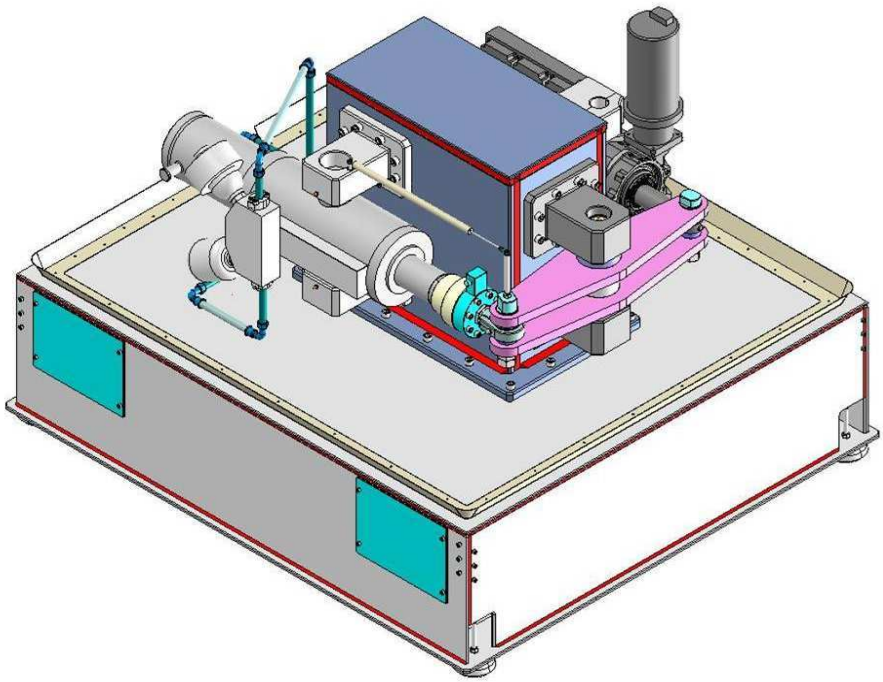

(b) 3D View

Figure 6.16: Line drawings of the test rig

Complications encountered with the test rig set up and the LVDT interface circuitry which needed to be modified, together with the time restrictions to complete the project meant that it was not possible to use the feedback from the LVDT. The calculation of the initial rotor angle was required to perform the position control as described in Section 6.2.1.

The EMA drive system position control was tested initially without loading the actuator and by gradually changing the maximum speed and the limit on the available i_q current. Even though it has been said that no load was applied to the actuator, a force, generated by the loading rig, opposing the movement of the actuator, was present. This force is proportional to the speed of the movement and it emulates the damping action of an inoperative actuator attached to the same rudder surface.

Initial tests were carried out to perform the position control of the actuator on the loading rig with the added effect of the damping force. The actuator was successively loaded with a constant force, increasing progressively up to 45kN, in addition to the damping force. Figures 6.17 to 6.22 show results from the position control tests. Figure 6.17 shows a step in position demand with the actuator loaded with 10kN against the direction of motion. The constant force of 10kN is provided by the test rig. The motor is accelerated with a maximum line current of 30A. Once up to speed, the current level drops slightly. This is the current required to move the actuator against the applied force. As the actuator reaches the desired position, the speed is reduced to zero and the current level at zero speed holds the actuator position against the applied 10kN load.

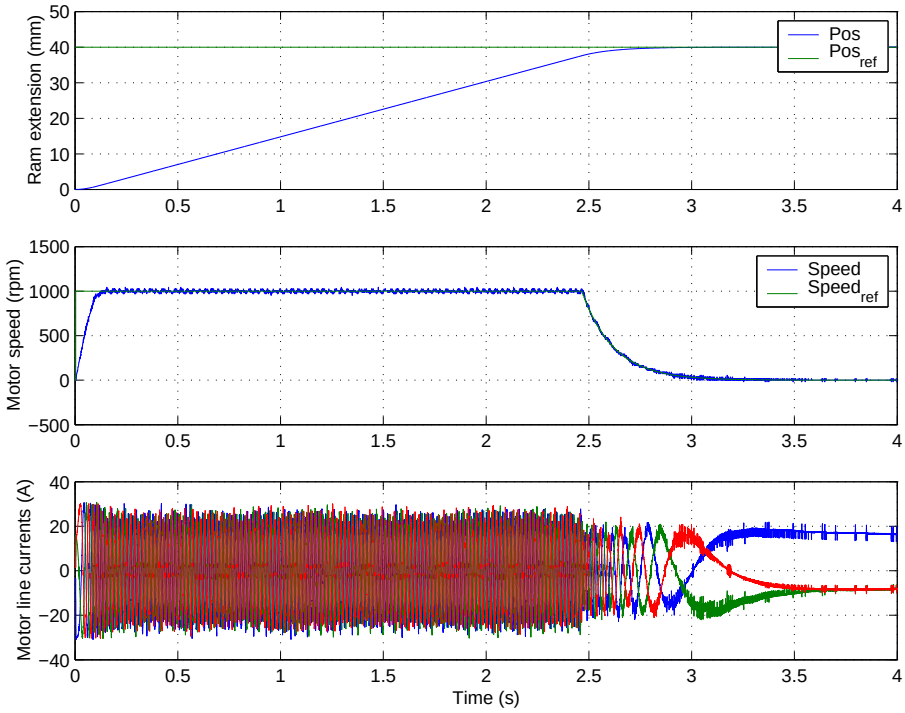

Figure 6.17: 40mm step position demand with 10kN lateral load applied, 30A current limit and 1000rpm speed limit

Differently to the previous test case, for the results shown in Figure 6.18, a square wave in the position demand is required which causes the actuator to move in both directions. This time a load of 30kN is applied to the actuator such that it will assist the movement of the actuator in one direction and it will oppose it in the other direction. This is clarified by the behaviour of the motor phase currents during the transients. When a positive position is demanded, the actuator's movement is made easier by the favourable action of the load. This is justified by the fact that, after the acceleration to the maximum speed of 2500rpm is achieved, a current of 80A is no longer required instead the current magnitude drops to the minimum value which is necessary to overcome the viscous damping friction of the system. When the negative position is demanded the load opposes the movement of the actuator therefore, after the acceleration to the maximum negative speed, the current magnitude decreases from the maximum value of 80A to 40A. In this way, a torque is developed, keeping the speed constant and allowing the movement of the actuator against the resistive action of the load.

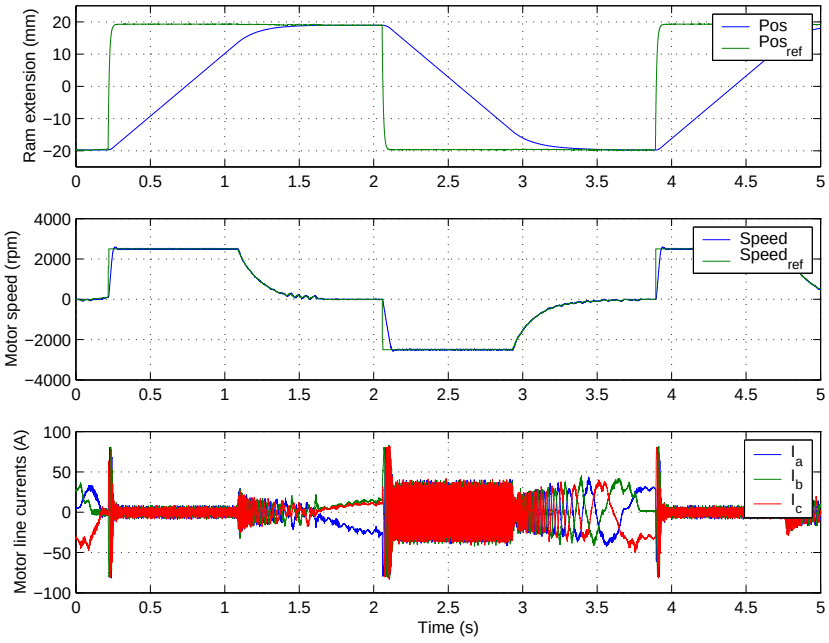

Figure 6.18: Square wave position demand with 30kN load applied, 80A current limit and 2500rpm speed limit

Figure 6.19 shows the behaviour of the power delivered to the motor during the speed transient of the test shown in the previous figure, just after the 2 second point, together with one phase of the input voltage and current supply. The maximum power

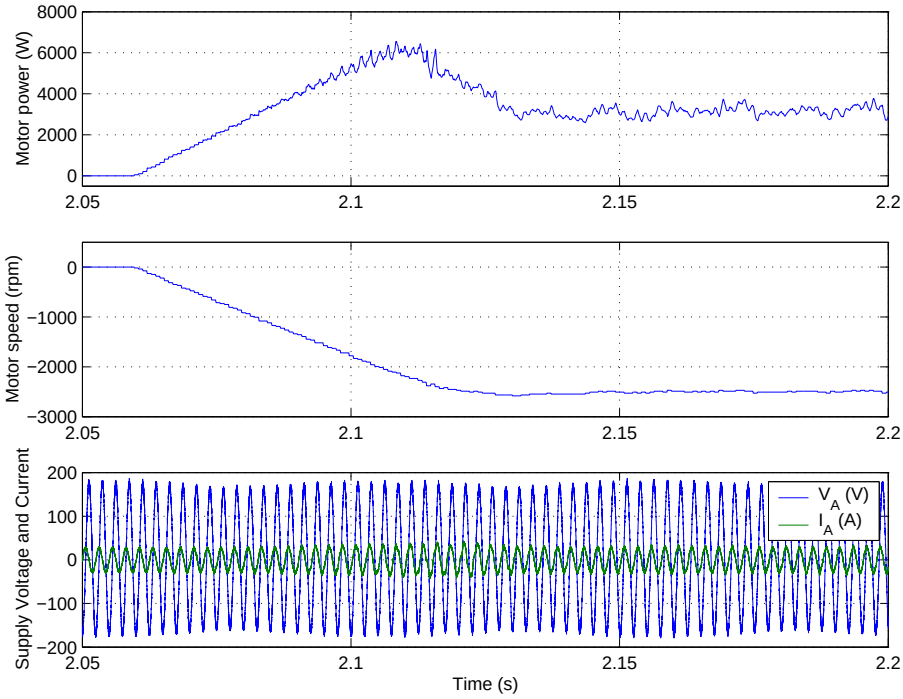

Figure 6.19: Power delivered to the motor during the speed transient, voltage and current supply

is delivered to the motor during the acceleration period at the maximum speed while it reduces to a lower but constant average value when a torque at constant speed is required to oppose the resistive action of the load as described earlier.

One phase of the input voltage and current supply of Figure 6.19 is shown in more detail in Figure 6.20. The sinusoidal input current can be seen as a validation of the results from the simulation of the EDAAS drive system done in SABER and described in Section 4.3

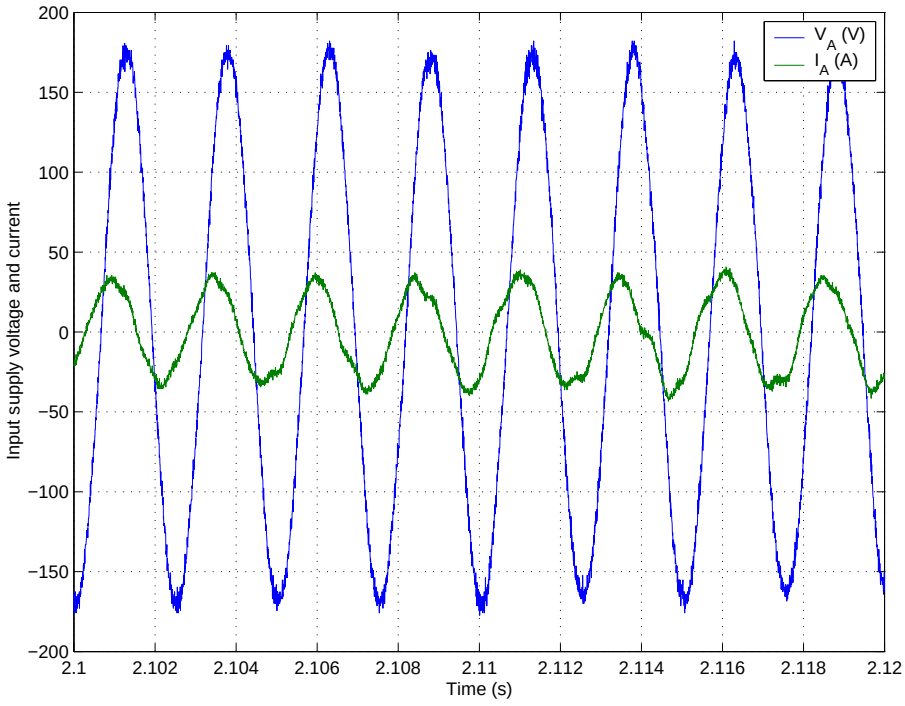

Figure 6.20: One phase of the input voltage and current supply

Figure 6.21 shows the response of the system to another square wave in the position demand (between +/- 20mm) but a load of 45kN is now applied to the actuator. The limits on the torque producing current, i_q, and the motor speed are set as before to 80A and 2500rpm respectively. Similarly to the 30kN test case, it is possible to see

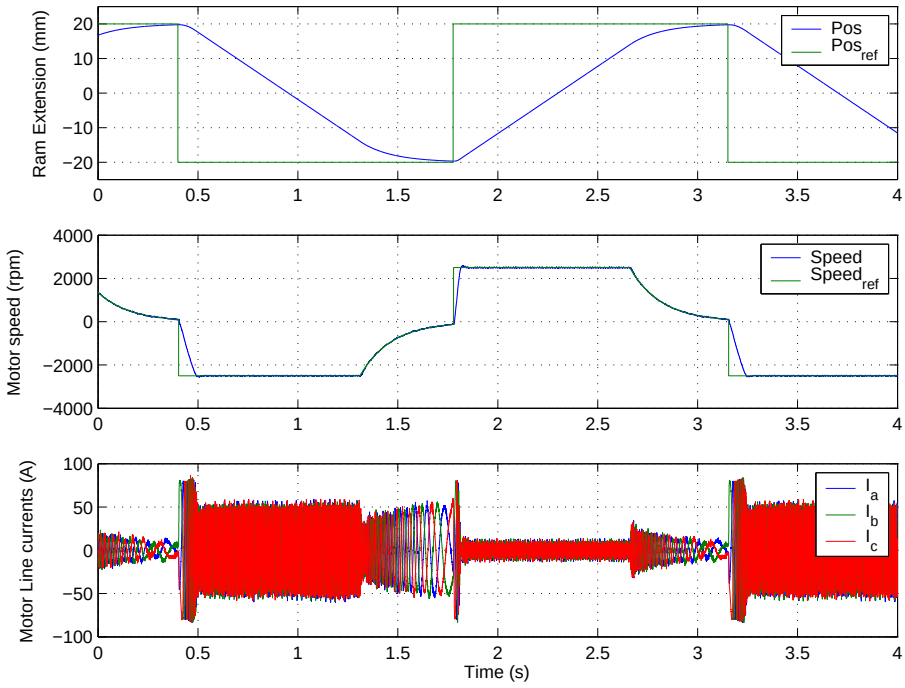

Figure 6.21: Square wave position demand with 45kN load applied, 80A current limit and 2500rpm speed limit: position response, motor speed and motor phase currents

when the actuator is assisted by the favourable action of the applied force of 45kN and when the actuator is opposed in its movement by the same force. While approaching the demanded negative position, during the first speed transient, the magnitude of the motor phase currents drop from the maximum value of 80A, which allows the machine to accelerate to 2500rpm, to 50A at constant speed. The higher value in the current magnitude at constant speed with respect to the previous test case is justified by the higher value of the force applied to the actuator which requires consequently a higher torque to guarantee the movement of the actuator against the resistive action of the load. It is interesting to analyse the behaviour of the torque producing current, i_q, during the second speed transient, that is when a positive position is demanded. This

is shown in Figure 6.22, which includes the behaviour of i_q. During the second speed

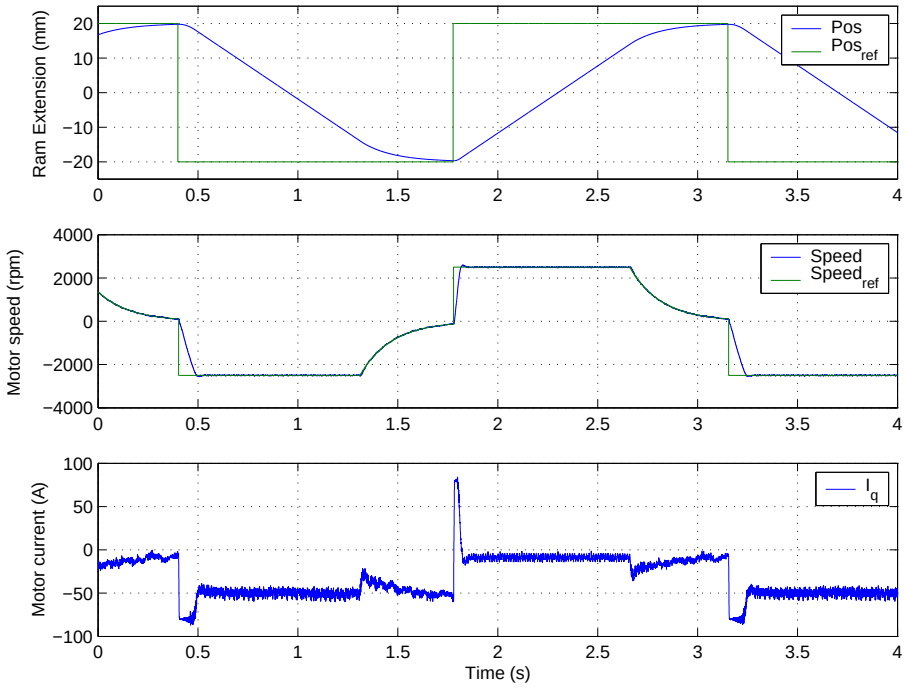

Figure 6.22: Square wave position demand with 45kN load applied: position response, motor speed and torque producing current i_q

transient, the actuator is assisted by the action of the force applied to it therefore after the peak in the i_q current of 80A to accelerate the machine to its maximum speed, i_q drops to a constant average negative value at a constant positive speed. This means that a negative torque is required to keep the machine spinning at the same speed of 2500rpm which suggests that the machine is trying to slow down the positive action of the applied load, causing regeneration.

The EMA drive system wasn't further loaded since, due to the tests conducted by applying progressively higher loads, the test rig needed to be re-assessed because signs of failure of the bottom mounting bracket bearing, were suspected.

6.4 Summary

In this chapter details of the final assembly and testing of the EDAAS matrix converter drive system and EMA drive system have been discussed. As soon as the implementation of the matrix converter was completed, its functionality and the communication between the Host PC, the DSP/FPGA controller, the Interface Card and finally the Gate drive boards were tested. This has been done by progressively testing the matrix converter performance when connecting it to, first an RL load, then using it to drive a 1.5kW induction machine and a 3kW permanent magnet synchronous machine which was employed in the TIMES project. Results from the initial tests on the matrix converter have been presented.

The next task performed consisted of testing the matrix converter driving the permanent magnet synchronous machine manufactured for the EDAAS project, achieving gradually and successfully, the implementation of the machine's cascaded speed and current control loops. The EDAAS machine was considered with and without its rotor salient characteristics which led to two different approaches in the current control design. The current control design of the salient EDAAS PMSM and therefore the possibility to increase the machine delivered torque, required a deeper knowledge of the characteristics of the machine itself and this could have been achieved with more testing. Due to restrictions imposed by the time available to complete the project, it was decided to not further investigate a way of optimizing the machine torque generation and to treat the machine as a non-salient PMSM.

Once the assembly of the EMA drive system was completed by mounting the matrix converter onto the actuator's oil can which integrates the heat sink and connecting the machine to worm-wheel/ballscrew of the actuator, the position control was finally implemented and tested. Results from initial step change in the position demand of the actuator with a maximum limit on the torque producing current, i_q, and on the motor speed of 135A and 5000rpm respectively, have been presented.

The following and final stage of the project was to deliver and commission the EMA

drive system. Once the EMA drive system was transferred to the research laboratory of Smiths Aerospace in Wolverhampton, it was mounted on the custom manufactured loading test rig to carry out all of the final stage tests. Figure 6.23 shows the EMA drive system mounted on the loading test rig. The test rig was used to provide

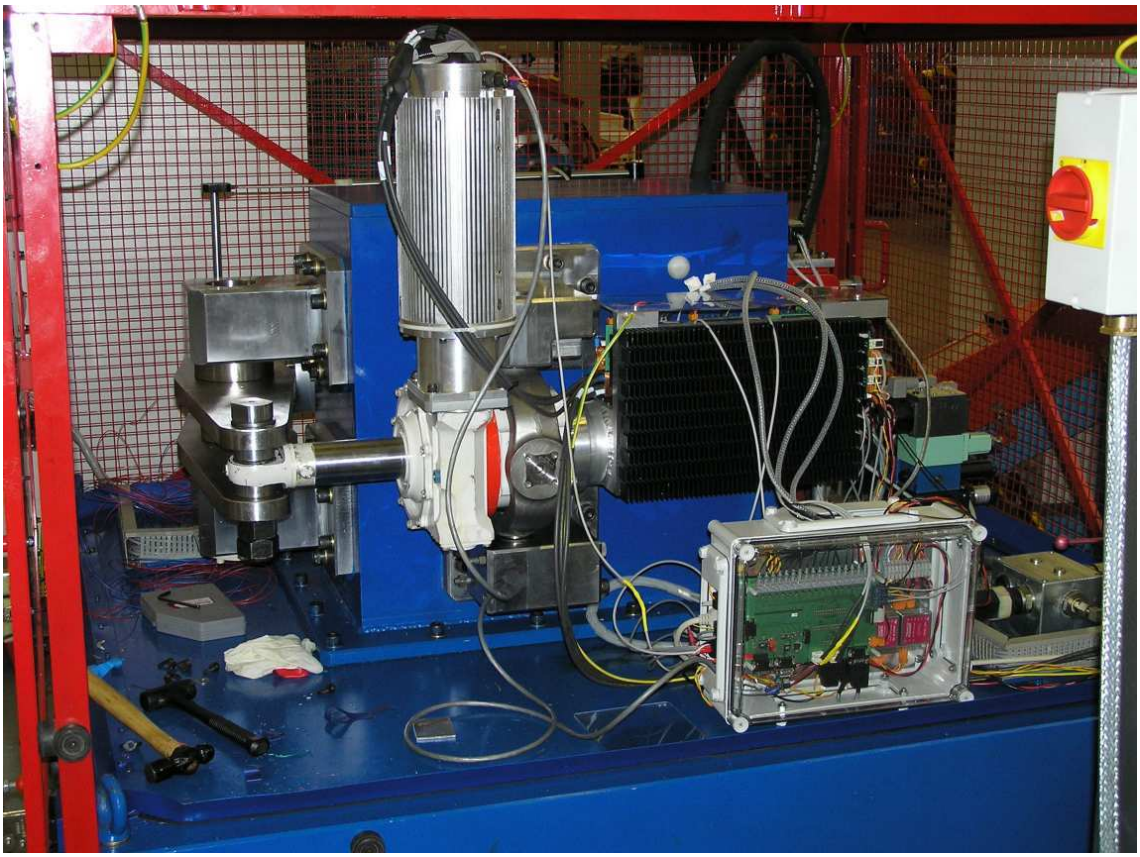

Figure 6.23: Final assembly of the EMA drive system mounted on the test rig at SMITHS research laboratory

the desired loading action on the actuator, gradually higher loads were employed in the range of between 10kN and 45kN. It was not advisable to further increase the load applied on the actuator because of possible failures of the supporting actuator structure on the test rig. Results of the final tests show the system position response to square wave in the position demand, with a maximum limit on the torque producing current, i_q, and on the motor speed of 80A and 2500rpm respectively, at different applied load conditions.

Chapter 7

Conclusions

The work presented in this thesis has been an exciting opportunity to give a small contribution to research on the More Electric Aircraft (MEA) concept. This concept aims to gradually remove the hydraulic power source and to reduce the hydraulic distribution infrastructure, replacing it with an electrical power source with its flexible distribution architecture. The MEA concept has received the interest of Governments and different sectors of Industry, not only the Aerospace Industry, and has involved research, to an increasing degree, by the academic world and Technology Centres. The increasing interest in the MEA research is driven by the awareness of the progress that has been achieved into new technologies since the MEA concept was first introduced in the 1970s. The main motivation is the potential progress that can be achieved if more research is invested, for example in the power electronics and electric machinery which are required to operate in very demanding environments.

The spirit of the MEA concept is demonstrated in the work done, and successfully implemented, on the Electric-Hydrostatic Actuator (EHA) and in the work done on the still to be completed and accepted, Electro-Mechanical Actuator (EMA), both of which are intended to replace the conventional hydraulically powered actuators for primary and secondary flight surfaces with electrically powered ones. The EHA has been officially introduced and successfully tested on the new AIRBUS A380 and it

represents an important step forward in the employment of more electrical systems in the place of heavy hydraulic piping, eliminating potential leakage sources and reducing overall weight and costs. The EHA, though, still needs a localised hydraulic system to implement the final control of the flight surface, which would not be required in the EMAs. The capability of the EMA to employ an electric motor to directly drive, through a gear set and ballscrew, the flight surface introduces a potentially greater advantage than in the EHA because it reduces even further complexity, weight and maintenance while increasing reliability.

The down sides of EMAs are still to be fully explored such as the case of the "jamming probability" of an EMA or its wear life. So what makes EMA worth investigating? The answer is in the potential advantages which EMAs could deliver and introduce into the overall aircraft architecture. The Aerospace Industry, with its conservative approach to new technologies, will need much more than promises in order to benefit from the advantages of the EMA such as cost and maintenance reduction and increasing reliability. More proof of the beneficial effects of employing EMAs instead of EHA or hydraulic actuators will need to be produced and this will be possible only through further study and research.

The way to the implementation of new technology in a well consolidated, reliable, conventional aircraft architecture is certainly long and is not easy but at the same time it did not stop the EHA being finally integrated into the new A380 architecture. This does not mean that it will be necessary to wait for another thirty years before EMAs will be successfully employed on a civil aircraft, as long as the interest for this new technology does not remain confined to the Aerospace Industry but meets the support of other sectors of Industry which will have to contribute in an equal way with new technologies and are directly responsible for the optimisation of the EMA development.

One interesting aspect of the development of EMAs is the power electronics employed to drive the motor which operates through the mentioned gear-set/ballscrew on the control of the flight surface. The novelty introduced by the work of this thesis is

to offer an alternative topology of power converter, the matrix converter, to drive the motor in an EMA, instead of the conventional Voltage Source Inverter (VSI) currently in use on EHAs. In the conventional VSI, the multi-pulse (12 or 18) rectification stage, the DC link and associated input filters add weight and complexity especially if it is considered that, for safety reasons, no electrolytic capacitors are allowed on the aircraft. Electrolytic capacitors are temperature sensitive and therefore unreliable when the typical ambient temperature range for this application varies between $-55°C$ and $+70°C$. To create the equivalent capacitance sized for the DC link, using film capacitors, they would require a considerable amount of space compared to electrolytic capacitors.

As it has been shown, matrix converters are able to be driven from frequency wild power systems, thus avoiding a DC conversion stage and the bulky, fixed frequency conversion stage used to provide electrical power in conventional aircraft. Besides this, the absence of a DC link in a matrix converter would allow an increase in the power density of the converter. It is possible to achieve bi-directional power flow with a matrix converter and by controlling the switching devices appropriately, both output voltage and input current can be sinusoidal. This is only true if there are no power fluctuations in the load which would be fed to the input supply with a consequent distortion of the line currents. This is an important issue which has been taken into consideration when looking at the characteristics of the application to be implemented.

In order to optimise the design of the drive which was going to operate on the rudder actuator, a detailed analysis using the SABER simulator was used to select the best topology of matrix converter drive system that could satisfy the aircraft power supply specifications. Indeed the result of this analysis showed that the choice of the machine is mainly dependent on the topology of converter selected for the considered application. Therefore the sinusoidal machines were preferred to the non-sinusoidal ones.

Among the sinusoidal machines, the induction machine's efficiency decreases at low

speed due to an increase in the rotor losses. Considering that the worse operating condition of a rudder actuator requires the drive to deliver half of the rated torque at very low speed, the induction machine would not be the preferred machine for this application. Therefore, it was finally decided to design and implement a matrix converter sinusoidal permanent magnet AC machine drive system.

The design and implementation of the matrix converter was not only an opportunity aimed at achieving an optimised practical realisation which could respond to the strict requirements of the particular application. Indeed, it has also been an occasion to develop a new and efficient strategy for implementing the matrix converter circuit protection, which even if inspired by it, is not dependent on the specific application. The importance of a prompt and efficient circuit protection in the matrix converter is again linked to the absence of a DC link, leaving the matrix converter without an energy storage facility when the load energy needs to be removed in an emergency situation.

The assembled matrix converter has been tested for its functionality and to verify that the communication between the Host PC, the DSP/FPGA controller, the Interface Card and finally the Gate drive boards were working correctly. Results from the initial tests on the matrix converter have been presented.

The matrix converter was connected to the permanent magnet synchronous machine designed and manufactured for this project in order to progressively achieve and implement its cascaded current and speed control. The consequent testing of the control structures involved not a small effort because of the non-linear characteristics of the machine driven, where knowledge of the characteristics required further testing on the machine itself which was not possible. Once achieved the speed control of the machine, which is explicative in the related results, the position control of the assembled EMA drive system was required and achieved first at the input supply frequency of 50Hz.

The final stage of the project was to deliver and commission the EMA drive system to

SMITHS AEROSPACE in Wolverhampton. The position control test was performed on the EMA drive system, mounted on the loading test rig, whilst applying gradually higher loads on the actuator. The results of the actuator position response, under loading conditions of 10kN, 35kN and 45kN, and at the input supply frequency of 400Hz, have been presented. They show the good performance of the matrix converter at different loading conditions and different input supply frequencies, besides the capability of bidirectional power flow of the converter.

The experience gained and passed from the TIMES project made it possible to successfully complete the EDAAS project in spite of the time constraints. The achieved electrically driven advanced actuation system was a challenge in terms of optimising the matrix converter with a compact and efficient layout, of implementing the control of the machine which could give the best performance in the time available to complete the project and of commissioning the EMA drive system on a loading test rig which again required time to commission. The work done also included simulation to provide an analysis of different matrix converter drive systems in order to select the appropriate one for the given application. The final goal has been achieved but more could possibly be done to realise the inherent potentialities of the EDAAS EMA drive system and a few ideas are suggested in the following section.

7.1 Further Work

The following are some of the areas in which it would be advisable to do further research in order to reach a more optimised implementation of the EDAAS EMA drive system.

Input Filter Design: This needs more analysis of the drive system at different input supply frequencies with different amounts of supply distortion in order to characterise the values of L, C and R which generate the attenuation of specified harmonics, whilst still trying to optimise the filter size. Different filter topologies could also be investigated with the aim of improving power quality whilst also improving the size

and weight.

The effect of the filter on the capacitive input power factor observed in simulation and experimentally, especially at high input frequency, needs to be addressed. It has been mentioned that one of the advantage of using a matrix converter over other topologies of converters is, depending on the modulation method used, the possibility of controlling the input displacement factor, irrespective of the type of load. This means that it may be possible to compensate for the poor power factor due to the input filter using the matrix converter modulation. However, this would not be possible under no load conditions.

Machine Torque Generation: Further tests on the salient PMSM need to be carried out in order to implement the appropriate current control strategy which would help to achieve the highest torque generation possible.

Electro Magnetic Compatibility (EMC) Problems: The commissioning and testing of the EMA drive system on the loading test rig, revealed the important issue of electro magnetic interference. It could not be determined whether the problem was due to the EMA system or in the susceptibility of the loading rig, although the wiring layout of the loading rig did not help.

References

[1] Jones R.I, "The More Electric Aircraft: The past and the future?," *Colloquium, Electrical Machines and Systems for the More Electric Aircraft, IEE Power Division*, vol. 99/180, pp. 1/1 – 1/4, 1999.

[2] Cronin M.J.J, "The All-Electric Aircraft," *IEE Review*, vol. 36(8), pp. 309 – 311, 1990.

[3] van den Bossche D, "More electric control surface actuation; a standard for the next generation of transport aircraft," *EPE Conference Record*, 2003.

[4] Faleiro L.F, "Trends towards a More Electrical Aircraft," *More Electric Aircraft Conference Record*, 2004. UK Royal Aeronautical Society.

[5] Weale D and Whitley C, "Power takes flight," *IEE Power Engineer, issue 3*, vol. 18, pp. 33 – 36, 2004.

[6] Dodds G, "The More Electric Aircraft," *Electrical Drive Systems for the More Electric Aicraft, UK Magnetic Society*, April 2005. One-Day Seminar.

[7] Wheeler P, Aten M, Whitley C, Towers G, Clare J, and Bradley K, "Reliability prediction of matrix converter and rectifier-inverter topologies for aerospace applications," *IEEE Transactions on Aerospace and Electronic Systems 1*, 2006.

[8] Weimer J.A, "The role of electric machines and drives in the more electric aircraft," *IEMDC Conference Record*, 2003.

[9] Howse M, "All Electric Aircraft," *IEE Power Engineer*, pp. 35 – 37, 2003.

[10] Gyugyi L and Pelly B, "Static Power Frequency Changers: Theory, Performance and Applications," *New York:John Wiley and Sons*, 1976.

[11] Wood P, "General Theory of Switching Power Converters," *IEEE PESC Conference Record*, pp. 3 – 10, 1979.

[12] Venturini M, "A New Sine Wave In Sine Wave Out, Conversion Technique Which Eliminates Reactive Elements," *Proceedings Powercon 7*, vol. E3, pp. 1 – 15, 1980.

[13] Alesina A and Venturini M, "Analysis and Design of Optimum-Amplitude Nine-Switch Direct AC-AC Converters," *IEEE Transactions on Power Electronics*, vol. 4, pp. 101 – 112, Jan. 1989.

[14] Oyama J, Higuchi T, Yamada E, Koga T, and Lipo T, "New Control Strategy For Matrix Converter," *IEEE PESC Conference Record*, pp. 360 – 367, 1989.

[15] Roy G, Duguay L, Manias S, and April G.E, "Asynchronous Operation of Cycloconverter with Improved Voltage Gain by Employing a Scalar Control Algorithm," *IEEE IAS Conference Record*, pp. 889 – 898, 1987.

[16] Roy G and April G. E, "Cycloconverter Operation Under a New Scalar Control Algorithm," *IEEE PESC Conference Record*, pp. 368 – 375, 1989.

[17] Huber L and Borojevic D, "Space Vector Modulator for Forced Commutated Cycloconverters," *IEEE IAS Conference Record*, vol. 1, pp. 871 – 876, 1989.

[18] Casadei D, Serra G, Tani A, and Zarri L, "A New General Approach Based on Space-Vector Representation of the Switch State," *IEEE Transactions on Industrial Electronics*, vol. 49, no. 2, pp. 370 – 381, 2002.

[19] Huber L, Borojevic D, and Burany N, "Analysis design and implementation of the space-vector modulator for forced-commutated cycloconvertors," *IEE Proceedings-B*, vol. 139, pp. 103 – 113, Mar. 1992.

[20] Ziogas P.D, Khan S.I, and Rashid M.H, "Some Improved Forced Commutated Cycloconverter Structures," *IEEE Transactions on Industry Applications*, vol. 1A-21, pp. 1242 – 1253, Sept. 1985.

[21] Ziogas P.D, Khan S.I, and Rashid M.H, "Analysis and Design of Forced Commutated Cycloconverter Structures with Improved Transfer Characteristics," *IEEE Transactions on Industrial Electronics*, vol. 1E-33, pp. 271 – 280, Aug. 1986.

[22] Friedrichs P and Rupp R, "Silicon Carbide Power Devices - Current Developments and Potential Applications," *EPE Conference Record*, 2005.

[23] Munzer M, Loddenkotter M, Simon O, and Bruckman M, "EconoMac the first all-in-one IGBT module for Matrix Converters," *Drives and Controls and Power Electronics Conference*, 2001.

[24] Dynex Semiconductor, "IGBT Bi-Directional Switch Module DIM200MBS12-A000," *Device Data Sheet, www.dynexsemi.com.*

[25] Sunter S and Clare J.C, "A true four quadrant matrix converter induction motor drive with servo performance," *IEEE PESC Conference Record*, pp. 146 – 151, 1996.

[26] Neft C.L and Schauder C.D, "Theory and Design of a 30-Hp Matrix Converter," *IEEE IAS Conference Record*, pp. 934 – 939, 1988.

[27] Beasant R.R, Beattie W.C, and Refsum A, "An Approach to the Realization of a High-Power Venturini Converter," *IEEE PESC Conference Record*, pp. 291 – 297, 1990.

[28] Apap M, Clare J.C, Wheeler P.W, and Bradley K, "Analysis and Comparasion of AC-AC Matrix Converter Control Strategies," *IEEE PESC Conference Record*, 2003.

[29] Empringham L, Wheeler P.W, and Clare J.C, "A Matrix Converter Induction Motor Drive using Intelligent Gate Drive Level Current Commutation Technique," *IEEE IAS Annual Meeting*, pp. 1936 – 1941, 2000.

[30] Kwon B.H, Min B.H, and Kim J.H, "Novel Commutation Technique of AC-AC converters," *IEE Proceedings Part B*, vol. 145, pp. 295 – 300, July 1998.

[31] Ziegler M and Hofmann W, "Semi Natural Two Steps Commutation Strategy for Matrix Converters," *IEEE PESC Conference Record*, pp. 727 – 731, 1998.

[32] Ziegler M and Hofmann W, "Performance of a Two Steps Commutated Matrix Converter for AC Variable Speed Drives," *IEEE Power Electronics Specialists Conference*, 1999.

[33] Ziegler M and Hofmann W, "A New Two Steps Commutation Policy for Low Cost Matrix Converter," *PCIM Conference Record*, 2000.

[34] Ziegler M and Hofmann W, "Rectifier based robust control of bidirectional switches in AC-AC matrix converters," *EPE-PEMC Conference Record*, 2002.

[35] Choi Jong-Woo and Sul Seng-Ki, "A new Compensation Strategy Reducing Voltage/Current Distortion in PWM VSI Systems Operating with Low Voltages," *IEEE IAS Annual Meeting*, vol. 31, pp. 1001 – 1008, 1995.

[36] Boulant H, Mazet L, Huselstein J.J, and Glaize C, "Four Quadrant Switches Direct Matrix Converter Switching Management by Time Gap Regulation," *PEMC Conference Record*, vol. 2, pp. 54 – 58, 1998.

[37] Mahlein J, Igney J, Braun M, and Simon O, "Robust Matrix Converter Commutation without explicit Sign Measurement," *EPE Conference Record*, 2001.

[38] Pan C.T, Chen T.C, and Shieh J.J, "A Zero Switching Loss Matrix Converter," *IEEE PESC Conference Record*, pp. 545 – 550, 1993.

[39] Hey H.L, Pinheiro H, and Pinheiro J.R, "A New Soft-Switching AC-AC Matrix Converter with a Single Actived Commutation Auxiliary Circuit," *IEEE PESC Conference Record*, pp. 965 – 970, 1995.

[40] Marcks M, "A New Double Resonant Zero Current Switching Matrix Converter," *EPE Conference Record*, vol. 2, pp. 100 – 105, 1992.

[41] Cho J.G and Cho G.H, "Soft Switched Matrix Converter for High Frequency Direct AC-to-AC Power Conversion," *EPE Conference Record*, vol. 4, pp. 196 – 201, 1991.

[42] Department of Defense Washington DC (USA), "Military Handbook Reliability Prediction of Electronic Equipment, MIL-HDBK-217F," 2 December 1991, Notice 2, 28 February 1995.

[43] Choi S, Enjeti P N, and Pitel I J, "Polyphase transformer arrangements with reduced kVA capacities for harmonic current reduction in rectifier-type utility interface," *IEEE Transactions on Power Electronics*, vol. 11, pp. 680 – 690, Sept. 1996.

[44] Paice D D, "Optimized 18-pulse type AC/DC, or DC/AC, converter system," *US Patent 5,124,904*, 1992.

[45] Chivite-Zabalza F J, Forsyth A J, and Trainer D R, "Analysis and practical evaluation of an 18-pulse rectifier for aerospace applications," *2nd IEE Int. conference on Power Electronics Machines and Drives (PEMD), Edinburgh (UK)*, pp. 338 – 349, Apr. 2004.

[46] Cheng K W E, "Comparative study of AC/DC converters for more Electric Aircraft," *7th International Conference on Power Electronics and Variable Speed Drives*, pp. 209 – 304, Sept. 1998. IEE conf. no. 456.

[47] Marshall J, "Reliability enhancement methodology and modeling for electronic equipment - The REMM Project," *IEE Power Division colloquium Electrical Machines and Systems for the More Electric Aircraft, London*, pp. 12/1 – 12/8, Nov. 1999.

[48] Robson P, Bradley K, Wheeler P, Clare J, de Lillo L, Gerada C, Pickering S, Lampard D, Goh C.K, Towers G, and Whitley C, "The impact of Matrix Converter Technology on Motor Design for an Integrated Flight Control Surface Actuation System," *IEEE IEMDC Conference Record*, vol. 1-3, 2003.

[49] Fitzgerald A.E, Kingsley C.Jr, and Umans S.D, "Electric Machinery," *Sixth Edition*, 2003.

[50] Torrey D.A, "An experimentally verified variable-reluctance machine model implemented in the Saber circuit simulator," *International Conference on the Computational Aspects of Electromechanical Energy Converters and Drives*, 1993.

[51] Churn P.M, Maxwell C.J, Sciofield N, Howe D, and Powell D.J, "Electrohydraulic actuation of primary flight control surfaces," *IEE Colloquium*, 1998. n 260.

[52] Mason G, Evernden K, Bennett J, Jack A, Mecrow B, and Atkinson D, "Distributed Electrical Actuation of Aircraft Flaps and Slats," *Electrical Drive Systems for the More Eletric Aircraft, One-day Seminar, UK Magnetis Society*, 2005.

[53] Dixon R, Gifford N, Sewell C, and Spalton M.C, "REACTS: Reliable Electrical Actuation Systems," *Electrical Machines and Systems for the More Electric Aircraft, Colloquium, IEE Power Division*, 1999.

[54] Bose B.K, "Power Electronics and Variable Frequency Drives Technology and Applications," *IEEE Press, Chapter 6*, 1997.

[55] Robson P, Bradley K, Wheeler P, Clare J, de Lillo L, Gerada C, Pickering S, Lampard D, Goh C.K, Towers G, and Whitley C, "The impact of the matrix converter on motor choice for an integrated flight control surface actuation drive system," *EPE Conference Record*, 2003.

[56] Wheeler P.W, Empringham L, Apap M, de Lillo L, Clare J.C, Bradley K, Whitley C, and Towers G, "A matrix converter motor drive for an aircraft actuation system," *EPE Conference Record*, 2003.

[57] EUPEC Semiconductor, "Switching Behaviour and Optimal Driving of IGBT^3 Modules," *Application Note, AN2003-03*, 2003.

[58] Phelps T.K and Tate W.S, "Optimizing passive input filter design," *Proceedings of POWERCON 6*, pp. G1.1 – G1.10, 1979.

[59] Nielsen P, Blaabjerg F, and Pederson J.K, "Novel Solutions for Protection of Matrix Converter to Three Phase Induction Machine," *IEEE IAS Conference Record*, pp. 1447 – 1454, Oct. 1997.

[60] Klumpner K, "An Indirect Matrix Converter with a Cost Effective Protection and Control," *Proceedings of EPE Conference*, 2005. CD-Rom Paper no. 0594.

Appendix A

Papers Published

de Lillo L, Wheeler P W, Apap M, Empringham L, Clare J C, Bradley K J, Whitley C, Towers G , "An Accurate Saber Simulation of Matrix Converter Drive Systems for More Electric Aircraft Applications", *European Power Electronics - PEMC Conference, Riga*, September 2004.

de Lillo L, Wheeler P W, Clare J C, Bradley K J, Whitley C, Towers G, "A 20 kW Matrix Converter Drive System for an Electro-Mechanical Aircraft (EMA) Actuator", *European Power Electronics Conference, Dresden*, September 2005.

Wheeler P W, Empringham L, de Lillo L, Bradley K J, Pickering S, Clare J C, Whitley C, Kearns P, and Towers G, "A High Power Rudder EMA with an Integrated Machine and Matrix Converter Design", *International Council of the Aeronautical Sciences (ICAS)*, 2006.

Wheeler P W, Aten M, Whitley C, Towers G, Clare J C, Bradley K, de Lillo L, "Reliability Prediction of Matrix Converter and Rectifier-Inverter Topologies for Aerospace Applications", *IEEE Transactions on Aerospace and Electronic Systems 1*, 2006.

Wheeler P W, Empringham L, de Lillo L, Bradley K J, Pickering S, Clare J C, Whitley C, Kearns P, Towers G, "An Integrated Machine and Matrix Converter based High

Power Rudder EMA", *IEE PEMD, Dublin*, 2006.

Wheeler P W, Apap M, Empringham L, Clare J C, de Lillo L, Bradley K J , Whitley, Towers G, "An Electro Hydrostatic Aircraft Actuator using a Matrix Converter Permanent Magnet Motor Drive", *IEE PEVD Conference*, April 2004.

Wheeler P W, Clare J C, Apap M, Empringham L, de Lillo L, Bradley K J, Whitley C, Towers G, "Power supply loss ride-through and device voltage drop compensation in a matrix converter permanent magnet motor drive for an aircraft actuator", *IEEE 35TH ANNUAL POWER ELECTRONICS SPECIALISTS CONFERENCE*, VOLS 1-6, 2004.

Robson P A, Bradley K J, Wheeler P W, Clare J C, de Lillo L, Gerada C, Pickering S J, Lampard D, Goh C K, Towers G, Whitley C, "The impact of matrix converter technology on motor design for an integrated flight control surface actuation system", *IEEE INTERNATIONAL ELECTRIC MACHINES AND DRIVES CONFERENCE*, VOLS 1-3, 2003.

Robson P A, Bradley K J, Wheeler P W, Clare J C, de Lillo L, Gerada C, Pickering S J, Lampard D, Goh C K, Towers G, Whitley C, "The impact of matrix converter on motor choice for an integrated flight control surface actuation drive system", *European Power Electronics CONFERENCE, Toulouse*, 2003.

Wheeler P W, Clare J C, Apap M, Empringham L, Bradley K J, Whitley C, Towers G, de Lillo L, "Matrix converter based permanent magnet motor drive for an electro-hydrostatic aircraft actuator", *IECON'03: THE 29TH ANNUAL CONFERENCE OF THE IEEE INDUSTRIAL ELECTRONICS SOCIETY*, VOLS 1 - 3, PROCEEDINGS

Appendix B

MAST Models

This Appendix contains the MAST models written for this project, used in the simulations described in Chapter 4.

B.1 Venturini Algorithm: 50% Method

```
template signalsgen_vent50 VA VB VC Varef ck p m =Tseq,td#,Vim
electrical VA,VB,Varef,VC
state logic_4 ck,p,m

number Tseq=1m ,
       td=1u
       #Vim=57600
{

number const=2/3
val t tAa,tBa,tCa
val v Vpsq,phase1,phase2,phase3,refa,Vimsq
```

```
phase1=v(VA)
phase2=v(VB)
phase3=v(VC)
refa=v(Varef)

#Vimsq=1
Vimsq=phase1**2+phase2**2+phase3**2+0.00000000001

Vpsq=const*(Vimsq)

tAa=0
tBa=0
tCa=0

tAa=(Tseq/3)*(1+(2*phase1*refa)/Vpsq)
tBa=(Tseq/3)*(1+(2*phase2*refa)/Vpsq)
tCa=(Tseq/3)*(1+(2*phase3*refa)/Vpsq)


when (dc_init) {
schedule_event(time,p,l4_0)
schedule_event(time,m,l4_0)
}
when(event_on(ck)){

if(ck==l4_1){

              schedule_event(time,m,l4_0)
              schedule_event(time+td,p,l4_0)

              #if(tAa>0) {
```

```
                    schedule_event(time+tAa,m,l4_1)#}
            #if(tBa>0) {
                    schedule_event(time+tAa+tBa,p,l4_1)#}
            }
                 }
}
```

B.2 Space Vector Modulation

```
template vsm1 VA VB VC Vaout Vbout Vcout ck p m outat2 outat1 =Tseq#,td,q,Vim
electrical VA,VB,VC,Vaout,Vbout,Vcout
state logic_4 ck,p,m
ref nu outat2,outat1

number Tseq=0.00008
      # td=......
{

state logic_4 v11[6,13]=[l4_1,l4_0,l4_0,l4_0,l4_0,l4_0,l4_0,l4_0,l4_0,l4_0,l4_0,l4_0,l4_1,
                         l4_0,l4_0,l4_0,l4_0,l4_0,l4_0,l4_1,l4_0,l4_0,l4_0,l4_0,l4_0,l4_0,
                         l4_1,l4_1,l4_0,l4_0,l4_0,l4_0,l4_0,l4_0,l4_0,l4_0,l4_0,l4_1,l4_1,
                         l4_0,l4_0,l4_0,l4_0,l4_0,l4_1,l4_1,l4_1,l4_0,l4_0,l4_0,l4_0,l4_0,
                         l4_1,l4_1,l4_1,l4_0,l4_0,l4_0,l4_0,l4_0,l4_0,l4_0,l4_0,l4_1,l4_1,l4_1,
                         l4_0,l4_0,l4_0,l4_0,l4_1,l4_1,l4_1,l4_1,l4_1,l4_0,l4_0,l4_0,l4_0],

              v12[6,13]=[l4_1,l4_1,l4_0,l4_0,l4_0,l4_0,l4_0,l4_0,l4_0,l4_0,l4_0,l4_0,l4_1,l4_1,
                         l4_0,l4_0,l4_0,l4_0,l4_0,l4_1,l4_1,l4_1,l4_0,l4_0,l4_0,l4_0,l4_0,
                         l4_1,l4_0,l4_0,l4_0,l4_0,l4_0,l4_0,l4_0,l4_0,l4_0,l4_0,l4_0,l4_1,
                         l4_0,l4_0,l4_0,l4_0,l4_0,l4_0,l4_1,l4_0,l4_0,l4_0,l4_0,l4_0,l4_0,
                         l4_1,l4_1,l4_1,l4_0,l4_0,l4_0,l4_0,l4_0,l4_0,l4_0,l4_0,l4_1,l4_1,l4_1,
                         l4_0,l4_0,l4_0,l4_0,l4_1,l4_1,l4_1,l4_1,l4_1,l4_0,l4_0,l4_0,l4_0],

              v13[6,13]=[l4_1,l4_1,l4_1,l4_0,l4_0,l4_0,l4_0,l4_0,l4_0,l4_0,l4_0,l4_1,l4_1,l4_1,
```

```
                        l4_0,l4_0,l4_0,l4_0,l4_1,l4_1,l4_1,l4_1,l4_1,l4_0,l4_0,l4_0,l4_0,
                        l4_1,l4_0,l4_0,l4_0,l4_0,l4_0,l4_0,l4_0,l4_0,l4_0,l4_0,l4_0,l4_1,
                        l4_0,l4_0,l4_0,l4_0,l4_0,l4_0,l4_1,l4_0,l4_0,l4_0,l4_0,l4_0,l4_0,
                        l4_1,l4_1,l4_0,l4_0,l4_0,l4_0,l4_0,l4_0,l4_0,l4_0,l4_0,l4_1,l4_1,
                        l4_0,l4_0,l4_0,l4_0,l4_0,l4_1,l4_1,l4_1,l4_0,l4_0,l4_0,l4_0,l4_0],

              v14[6,13]=[l4_1,l4_1,l4_1,l4_0,l4_0,l4_0,l4_0,l4_0,l4_0,l4_0,l4_1,l4_1,l4_1,
                        l4_0,l4_0,l4_0,l4_0,l4_1,l4_1,l4_1,l4_1,l4_1,l4_0,l4_0,l4_0,l4_0,
                        l4_1,l4_1,l4_0,l4_0,l4_0,l4_0,l4_0,l4_0,l4_0,l4_0,l4_0,l4_1,l4_1,
                        l4_0,l4_0,l4_0,l4_0,l4_0,l4_1,l4_1,l4_1,l4_0,l4_0,l4_0,l4_0,l4_0,
                        l4_1,l4_0,l4_0,l4_0,l4_0,l4_0,l4_0,l4_0,l4_0,l4_0,l4_0,l4_0,l4_1,
                        l4_0,l4_0,l4_0,l4_0,l4_0,l4_0,l4_1,l4_0,l4_0,l4_0,l4_0,l4_0,l4_0],

              v15[6,13]=[l4_1,l4_1,l4_0,l4_0,l4_0,l4_0,l4_0,l4_0,l4_0,l4_0,l4_0,l4_1,l4_1,
                        l4_0,l4_0,l4_0,l4_0,l4_0,l4_1,l4_1,l4_1,l4_0,l4_0,l4_0,l4_0,l4_0,
                        l4_1,l4_1,l4_1,l4_0,l4_0,l4_0,l4_0,l4_0,l4_0,l4_0,l4_0,l4_1,l4_1,
                        l4_0,l4_0,l4_0,l4_0,l4_1,l4_1,l4_1,l4_1,l4_1,l4_0,l4_0,l4_0,l4_0,
                        l4_1,l4_0,l4_0,l4_0,l4_0,l4_0,l4_0,l4_0,l4_0,l4_0,l4_0,l4_0,l4_1,
                        l4_0,l4_0,l4_0,l4_0,l4_0,l4_0,l4_1,l4_0,l4_0,l4_0,l4_0,l4_0,l4_0],

              v16[6,13]=[l4_1,l4_0,l4_0,l4_0,l4_0,l4_0,l4_0,l4_0,l4_0,l4_0,l4_0,l4_0,l4_1,
                        l4_0,l4_0,l4_0,l4_0,l4_0,l4_0,l4_1,l4_0,l4_0,l4_0,l4_0,l4_0,l4_0,
                        l4_1,l4_1,l4_1,l4_0,l4_0,l4_0,l4_0,l4_0,l4_0,l4_0,l4_1,l4_1,l4_1,
                        l4_0,l4_0,l4_0,l4_0,l4_1,l4_1,l4_1,l4_1,l4_1,l4_0,l4_0,l4_0,l4_0,
                        l4_1,l4_1,l4_0,l4_0,l4_0,l4_0,l4_0,l4_0,l4_0,l4_0,l4_0,l4_1,l4_1,
                        l4_0,l4_0,l4_0,l4_0,l4_0,l4_1,l4_1,l4_1,l4_0,l4_0,l4_0,l4_0,l4_0],

              v21[6,13]=  ....
                .
                .          :this section omitted for clarity
                .
              v66[6,13]=  ....



number const=2/3,
       const1=2/sqrt(3),
       pi=3.14
```

```
val t tI,tII,tIII,tIV,t0,t03_2,t03,t2ev,t3ev,t4ev,t5ev,t6ev,t7ev,t8ev,t9ev,t10ev,t11ev,
    t12ev,t2od,t3od,t4od,t5od,t6od,t7od,t8od,t9od,t10od,t11od,t12od


val v Vpsq,phase1,phase2,phase3,outa,outb,outc,Vimsq,Vomsq,Vim,Vom#,Vj
val nu q

phase1=v(VA)
phase2=v(VB)
phase3=v(VC)
outa=v(Vaout)
outb=v(Vbout)
outc=v(Vcout)

#Vimsq=1
Vimsq=phase1**2+phase2**2+phase3**2+0.00000000001
Vomsq=outa**2 + outb**2 +outc**2+0.00000000001

Vpsq=const*(Vimsq)
Vim =0.8165*sqrt(Vimsq)
Vom =0.8165*sqrt(Vomsq)

#const1=2/sqrt(3)

q =Vom/Vim
if(q>0.75) q=0.75

kv=(outat1+(pi/3))/(pi/3)
ki=(outat2+(pi/2))/(pi/3)

if(kv<1) kv=1
else if(kv>=1 & kv<2) kv=1
else if(kv>=2 & kv<3) kv=2
else if(kv>=3 & kv<4) kv=3
else if(kv>=4 & kv<5) kv=4
else if(kv>=5 & kv<6) kv=5
else if(kv>=6 & kv<7) kv=6
```

```
if(ki<1) ki=1
if(ki>=1 & ki<2) ki=1
else if(ki>=2 & ki<3) ki=2
else if(ki>=3 & ki<4) ki=3
else if(ki>=4 & ki<5) ki=4
else if(ki>=5 & ki<6) ki=5
else if(ki>=6 & ki<7) ki=6
else if(ki>=7) ki=1

a_o=outat1-(kv-0.5)*(pi/3)
b_i=outat2-(ki- 1 )*(pi/3)

#fat1=(-1)**(kv+ki)
#fat2=(-1)**(kv+ki+1)

cosa_omeno=cos(a_o-(pi/3))
cosa_opiu=cos(a_o+(pi/3))
cosb_imeno=cos(b_i-(pi/3))
cosb_ipiu=cos(b_i+(pi/3))



tI  =0
tII =0
tIII=0
tIV =0

tI  =(Tseq/2)*(const1*q*cosa_omeno*cosb_imeno)
tII =(Tseq/2)*(const1*q*cosa_omeno*cosb_ipiu)
tIII=(Tseq/2)*(const1*q*cosa_opiu*cosb_imeno)
tIV =(Tseq/2)*(const1*q*cosa_opiu*cosb_ipiu)

t0   =(Tseq/2)-(tI+tII+tIII+tIV)
t03  =t0/3
t03_2=2*t03
t2ev =t03+tIII
t3ev =t2ev+tI
t4ev =t3ev+t03
```

```
t5ev =t4ev+tII
t6ev =t5ev+tIV
t7ev =t6ev+t03_2
t8ev =t7ev+tIV
t9ev =t8ev+tII
t10ev=t9ev+t03
t11ev=t10ev+tI
t12ev=t11ev+tIII
#t13ev=t12ev+t03

t2od =t03+tI
t3od =t2od+tIII
t4od =t3od+t03
t5od =t4od+tIV
t6od =t5od+tII
t7od =t6od+t03_2
t8od =t7od+tII
t9od =t8od+tIV
t10od=t9od+t03
t11od=t10od+tIII
t12od=t11od+tI
#t13od=t12od+t03

when (dc_init) {
                schedule_event(time,p,l4_0)
                schedule_event(time,m,l4_0)

                }

when(event_on(ck)){


                if(ck==l4_1){
                           if(ki==1 & kv==1){
                                        schedule_event(time+Tseq,p,v11[1,1])
                                        schedule_event(time+Tseq,m,v11[2,1])
```

```
schedule_event(time+Tseq+t03,p,v11[1,2])
schedule_event(time+Tseq+t03,m,v11[2,2])


schedule_event(time+Tseq+t2ev,p,v11[1,3])
schedule_event(time+Tseq+t2ev,m,v11[2,3])

schedule_event(time+Tseq+t3ev,p,v11[1,4])
schedule_event(time+Tseq+t3ev,m,v11[2,4])

schedule_event(time+Tseq+t4ev,p,v11[1,5])
schedule_event(time+Tseq+t4ev,m,v11[2,5])


schedule_event(time+Tseq+t5ev,p,v11[1,6])
schedule_event(time+Tseq+t5ev,m,v11[2,6])


schedule_event(time+Tseq+t6ev,p,v11[1,7])
schedule_event(time+Tseq+t6ev,m,v11[2,7])


schedule_event(time+Tseq+t7ev,p,v11[1,8])
schedule_event(time+Tseq+t7ev,m,v11[2,8])

schedule_event(time+Tseq+t8ev,p,v11[1,9])
schedule_event(time+Tseq+t8ev,m,v11[2,9])

schedule_event(time+Tseq+t9ev,p,v11[1,10])
schedule_event(time+Tseq+t9ev,m,v11[2,10])


schedule_event(time+Tseq+t10ev,p,v11[1,11])
schedule_event(time+Tseq+t10ev,m,v11[2,11])


schedule_event(time+Tseq+t11ev,p,v11[1,12])
schedule_event(time+Tseq+t11ev,m,v11[2,12])
```

```
                                        schedule_event(time+Tseq+t12ev,p,v11[1,13])
                                        schedule_event(time+Tseq+t12ev,m,v11[2,13])


                                        }

                        if(ki==1 & kv==2){
                                        schedule_event(time+Tseq,p,v12[1,1])
                                        schedule_event(time+Tseq,m,v12[2,1])
                        .
                        .       :all if statements for ki = 1-6 and kv = 2-6
                        .       :remainder omitted for clarity

                        }
                }
        }
}
```

B.3 Four Step Current Commutation

```
template comblocgen af ar bf br cf cr p m i dis=t1,t2,t3,ten

state logic_4 af,ar,bf,br,cf,cr,p,m,i,dis
number t1= 1u,
       t2= 200n,
       t3= 500n,
       ten
#td=10u
{

when (dc_init) {
schedule_event(time,dis,l4_1)
}
when (event_on(p)) {
```

```
if (p==l4_1) {
  if (m==l4_1) {
    if (i==l4_1)    {                                  # se i>0  la var. i e'high

     # commutation from Vb - Vc

     schedule_event(time,dis,l4_0)
     schedule_event(time,br,l4_0)
     schedule_event(time+t1,cf,l4_1)                 #  sequence for i>0
     schedule_event(time+t2+t1,bf,l4_0)
     schedule_event(time+t3+t2+t1,cr,l4_1)
     schedule_event(time+ten,dis,l4_1)
    }
    else {
     schedule_event(time,dis,l4_0)
     schedule_event(time,bf,l4_0)                    #
     schedule_event(time+t1,cr,l4_1)                 #  sequence for i<0
     schedule_event(time+t2+t1,br,l4_0)                 #
     schedule_event(time+t3+t2+t1,cf,l4_1)                 #
     schedule_event(time+ten,dis,l4_1)
    }
  }
  else {
    if (i==l4_1)    {

     # commutation from Va - Vc

     schedule_event(time,dis,l4_0)
     schedule_event(time,ar,l4_0)                    #
     schedule_event(time+t1,cf,l4_1)                 #  sequence for i>0
     schedule_event(time+t2+t1,af,l4_0)                 #
     schedule_event(time+t3+t2+t1,cr,l4_1)                 #
     schedule_event(time+ten,dis,l4_1)
     }
    else {
     schedule_event(time,dis,l4_0)
     schedule_event(time,af,l4_0)                    #
     schedule_event(time+t1,cr,l4_1)                 #  sequence for i<0
```

```
      schedule_event(time+t2+t1,ar,l4_0)                #
      schedule_event(time+t3+t2+t1,cf,l4_1)                #
      schedule_event(time+ten,dis,l4_1)
      }
    }
}
 else {
     if (m==l4_1) {
       if (i==l4_1)    {
         # commutation from Vc - Vb

         schedule_event(time,dis,l4_0)
         schedule_event(time,cr,l4_0)                   #
         schedule_event(time+t1,bf,l4_1)                #  sequence for i>0
         schedule_event(time+t2+t1,cf,l4_0)                #
         schedule_event(time+t3+t2+t1,br,l4_1)                #
         schedule_event(time+ten,dis,l4_1)
       }
       else {
         schedule_event(time,dis,l4_0)
         schedule_event(time,cf,l4_0)                   #
         schedule_event(time+t1,br,l4_1)                #  sequence for i<0
         schedule_event(time+t2+t1,cr,l4_0)                #
         schedule_event(time+t3+t2+t1,bf,l4_1)                #
         schedule_event(time+ten,dis,l4_1)
       }
     }
     else {
         if (i==l4_1)    {

          # commutation from Vc - Va

          schedule_event(time,dis,l4_0)
          schedule_event(time,cr,l4_0)                   #
          schedule_event(time+t1,af,l4_1)                #  sequence for i>0
          schedule_event(time+t2+t1,cf,l4_0)                #
          schedule_event(time+t3+t2+t1,ar,l4_1)                #
          schedule_event(time+ten,dis,l4_1)
```

```
            }
           else {
            schedule_event(time,dis,l4_0)
            schedule_event(time,cf,l4_0)                    #
            schedule_event(time+t1,ar,l4_1)                 #  sequence for i<0
            schedule_event(time+t2+t1,cr,l4_0)                  #
            schedule_event(time+t3+t2+t1,af,l4_1)                  #
            schedule_event(time+ten,dis,l4_1)
            }
        }
      }
}
when (event_on(m)) {
    if (m==l4_1) {
      if (p==l4_0) {
        if (i==l4_1)    {

          # no commutation when m=1 and p=1

          # commutation from Va - Vb

          schedule_event(time,dis,l4_0)
          schedule_event(time,ar,l4_0)                  #
          schedule_event(time+t1,bf,l4_1)               #  sequence for i>0
          schedule_event(time+t2+t1,af,l4_0)                #
          schedule_event(time+t3+t2+t1,br,l4_1)                #
          schedule_event(time+ten,dis,l4_1)
         }
        else {
          schedule_event(time,dis,l4_0)
          schedule_event(time,af,l4_0)                  #
          schedule_event(time+t1,br,l4_1)               #  sequence for i<0
          schedule_event(time+t2+t1,ar,l4_0)                #
          schedule_event(time+t3+t2+t1,bf,l4_1)                #
          schedule_event(time+ten,dis,l4_1)
        }
      }
    }
```

```
    else {
        if (p==l4_0) {
          if (i==l4_1)    {

            # no commutation when m=0 and p=1

            # commutation from Vb - Va

            schedule_event(time,dis,l4_0)
            schedule_event(time,br,l4_0)                    #
            schedule_event(time+t1,af,l4_1)                 #  sequence for i>0
            schedule_event(time+t2+t1,bf,l4_0)                 #
            schedule_event(time+t3+t2+t1,ar,l4_1)                 #
            schedule_event(time+ten,dis,l4_1)
          }
          else {
            schedule_event(time,dis,l4_0)
            schedule_event(time,bf,l4_0)                    #
            schedule_event(time+t1,ar,l4_1)                 #  sequence for i<0
            schedule_event(time+t2+t1,br,l4_0)                 #
            schedule_event(time+t3+t2+t1,af,l4_1)                 #
            schedule_event(time+ten,dis,l4_1)
          }
        }
       }
   }
}
```